

Review

# Recent Developments and Advancements in Solar Air Heaters: A Detailed Review

Varun Pratap Singh <sup>1,\*</sup>, Siddharth Jain <sup>1</sup>, Ashish Karn <sup>1</sup>, Ashwani Kumar <sup>2</sup>, Gaurav Dwivedi <sup>3</sup>, Chandan Swaroop Meena <sup>4,5,\*</sup>, Nitesh Dutt <sup>6</sup> and Aritra Ghosh <sup>7,\*</sup>

<sup>1</sup> Department of Mechanical Engineering, School of Engineering, University of Petroleum and Energy Studies, Dehradun 248007, India

<sup>2</sup> Technical Education Department Uttar Pradesh, Kanpur 208024, India

<sup>3</sup> Energy Centre, Maulana Azad National Institute of Technology, Bhopal 462003, India

<sup>4</sup> CSIR-Central Building Research Institute, Roorkee 247667, India

<sup>5</sup> Academy of Scientific and Innovative Research (AcSIR), Ghaziabad 201002, India

<sup>6</sup> Department of Mechanical Engineering, College of Engineering Roorkee, Roorkee 247667, India

<sup>7</sup> Faculty of Environment, Science and Economy (ESE), Renewable Energy, Electric and Electronic Engineering, University of Exeter, Penryn, Cornwall TR10 9FE, UK

\* Correspondence: ray\_varun@yahoo.com (V.P.S.); chandanswaroop2008@gmail.com (C.S.M.); a.ghosh@exeter.ac.uk (A.G.)

**Abstract:** The scientific literature extensively mentions the use of a solar air heater (SAH) by utilizing solar energy for heating purposes. The poor heat-transfer rate of an SAH with a flat plate is caused by developing a laminar sub-layer near the heated base plate. The plate temperatures improve significantly, resulting in losses and a decrease in performance. The passive approach entails the placement of fins/turbulators/pouring material/ribs to the surface where the boundary layer forms to disrupt it. Artificially roughened SAH for gathering and efficiently using solar radiations for thermal purposes is extensively described in the literature. This paper includes a thorough literature overview of the history, basics, roughness evolution, forms of SAH, and recent breakthroughs in thermal performance improvement techniques for SAH compiled by several researchers. This paper uses a comparative evaluation of several roughness geometries and kinds of SAH to uncover thermohydraulic performance factors that may be considered in future research to pick the optimal configuration.

**Keywords:** solar energy; solar air heater; thermal performance; artificial roughness; single and double pass



**Citation:** Singh, V.P.; Jain, S.; Karn, A.; Kumar, A.; Dwivedi, G.; Meena, C.S.; Dutt, N.; Ghosh, A. Recent Developments and Advancements in Solar Air Heaters: A Detailed Review. *Sustainability* **2022**, *14*, 12149. <https://doi.org/10.3390/su141912149>

Academic Editor: Akbar Maleki

Received: 12 August 2022

Accepted: 11 September 2022

Published: 26 September 2022

**Publisher's Note:** MDPI stays neutral with regard to jurisdictional claims in published maps and institutional affiliations.



**Copyright:** © 2022 by the authors. Licensee MDPI, Basel, Switzerland. This article is an open access article distributed under the terms and conditions of the Creative Commons Attribution (CC BY) license (<https://creativecommons.org/licenses/by/4.0/>).

## 1. Introduction

Energy is a basic necessity for life's survival and has emerged as a critical element in the global economy's development. Energy is traditionally derived from fossil fuels, massive hydroelectric systems, and wood products, such as coal, oil, and gas. However, the recent oil crisis fueled speculation about long-term shifts in the global economic system towards alternative sources of energy and environmental issues. The coal supply is finite and will last just a few hundred years [1]. The present energy paradigm depends on conventional energy sources, despite the reality that they are limited and beyond control commercially for many emerging nations. The availability of conventional energy sources is finite and affects the environment by creating pollution [2]. Various factors demotivate the growth of conventional fuels for energy generation, such as the limited availability of nuclear energy and coal reserves and threats of pollution, which harm flora and fauna. Therefore, there is a need to meet the energy-consumption objective by using such energy resources that are available in plenty in nature and create less pollution [3].

The sun provides the most readily available source of energy available on earth as direct solar irradiance and indirect forms like wind, agriculture, hydro, and sea. Solar energy is, therefore, an auspicious alternative energy source that is environmentally friendly,

free, and widely available (Figure 1). It can meet all the world's current and future needs without disturbance [4].

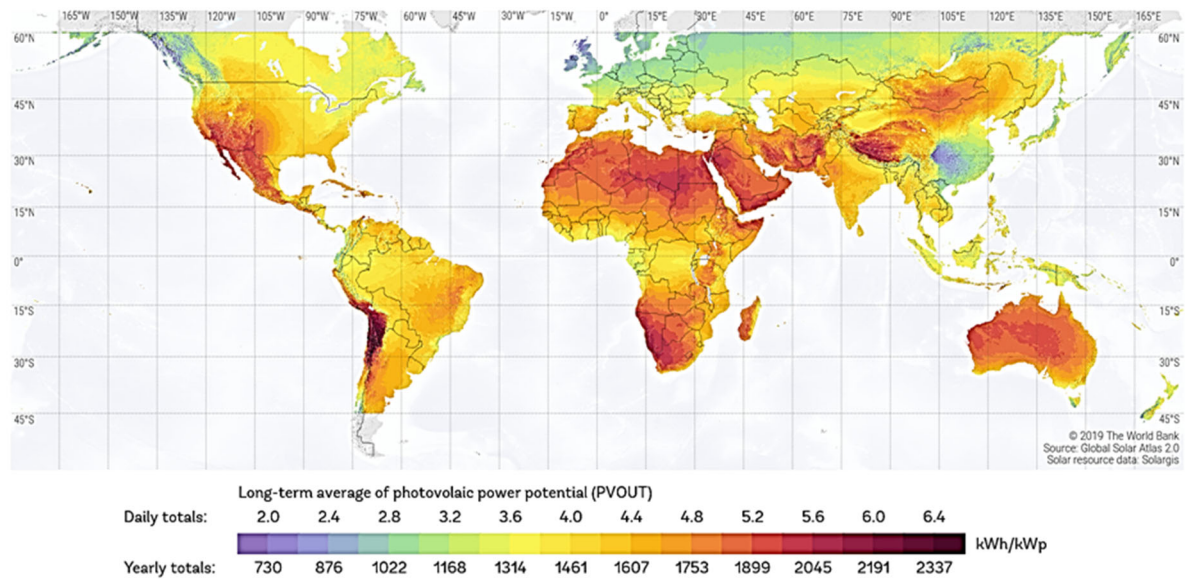


**Figure 1.** World map of global solar irradiation (Solar Resource Maps and GIS Data for 200+ Countries. Available online: <https://solargis.com/maps-and-gis-data/overview> (accessed on 5 July 2022).

Solar energy can be used directly across several thermal applications, such as heating water or air heating, drying, distilling, water pumping, cooking, agricultural greenhouses, heating and cooling of buildings, salt production, photochemical and photobiological conversions, and hydrogen-gas generation [5]. The high-temperature fluids can be used for purposes such as energy generation and heating [6]. Solar-energy harnessing can be done by different technologies, i.e., helio-thermal technology, helio-electrical technology, and helio-chemical technology [7] (Figure 2). Helio-thermal energy utilization involves using solar collectors to heat the fluid, which can be used for different purposes.

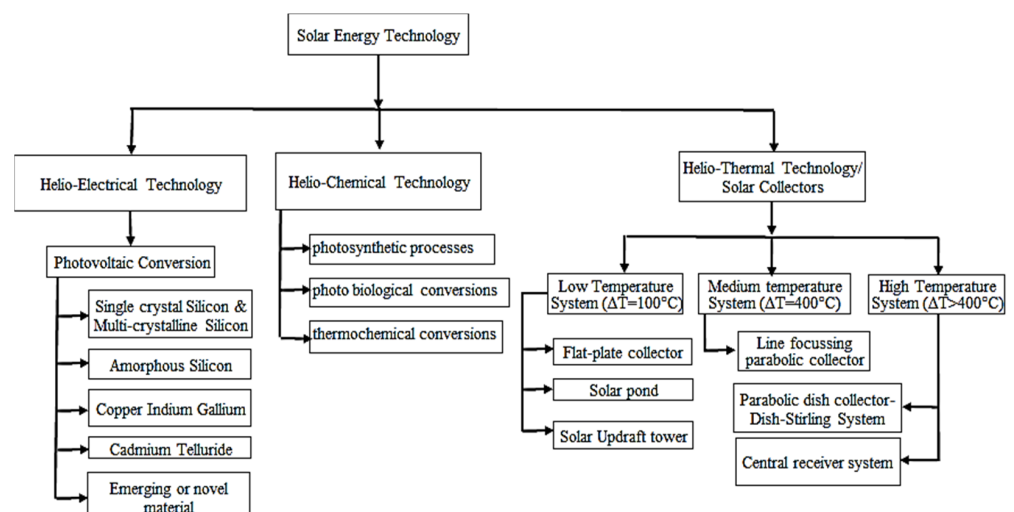


**Figure 2.** Classification of solar-energy technology.

### 1.1. Helio-Thermal Technology (Solar Collectors)

An Englishman, William Adams, conducted the first experiments on the generation of solar thermal power in India in the mid-19th century by focusing the sun's rays on creating steam [1]. Solar thermal conversion is a technological scheme that uses a dark surface placed in front of the sun, absorbs solar energy, and heats up, and then the heat

is transmitted to the circulation fluid. This can be stored in thermal storage and used for various purposes, as shown in Figure 3 [8].

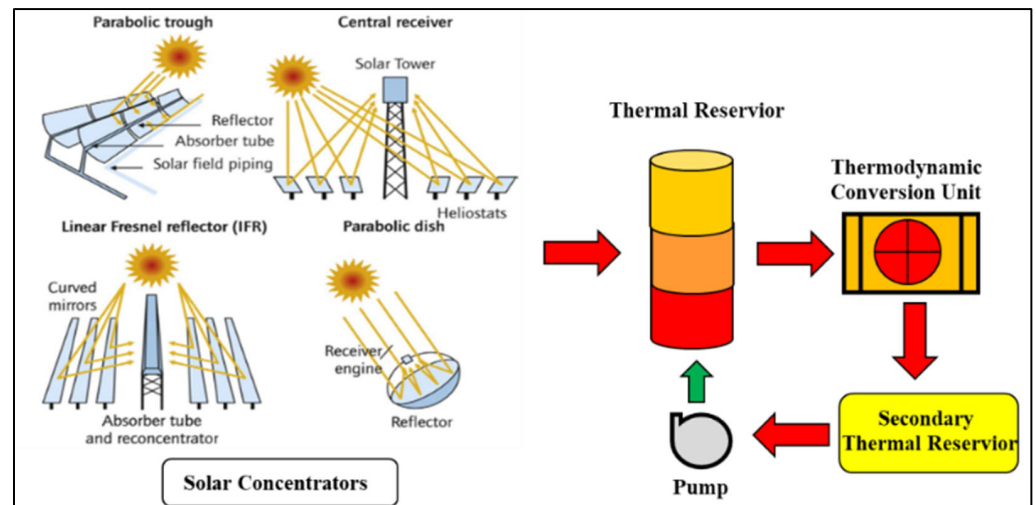


**Figure 3.** Different solar concentrator- linear Fresnel reflector, parabolic dish and through concentrator, reprinted with permission from [8], 2022, Elsevier.

### 1.2. Solar-Collecting System

A solar-collecting system (SCS) is a device that collects solar insolation to generate heat, which is subsequently transferred to a fluid. The two main types of SCS are non-concentrating or fixed collectors and focusing collectors [9]. The size of a non-concentrating collector (flat plate) for capturing and absorbing solar energy is the same. In contrast, a focusing collector (concave reflecting surfaces) has a smaller receiving area to intercept and focus solar-beam radiation, thus capturing the radiation flux [10]. Concentrating collectors can be classified into different types, which include “parabolic trough collector, mirror strip reflector, Fresnel lens collector, flat plate collector with adjustable mirrors, and compound parabolic concentrator” [5]. Broad classification of solar concentrators is conducted based on working fluid temperature, as mentioned below [11]:

- (a) High-temperature system ( $\Delta T > 400\text{ }^{\circ}\text{C}$ )
  - Parabolic dish-collector
  - Dish-sterling system
  - Central receiver system
- (b) Medium-temperature system ( $\Delta T = 400\text{ }^{\circ}\text{C}$ )
  - Line-focusing parabolic collector
- (c) Low-temperature system ( $\Delta T = 100\text{ }^{\circ}\text{C}$ )
  - Flat-plate collector
  - Solar pond
  - Solar-updraft tower

### 1.3. Low-Temperature System ( $\Delta T = 100\text{ }^{\circ}\text{C}$ )

Solar systems with a maximum working temperature range of  $100\text{ }^{\circ}\text{C}$  are classified in this category as flat-plate collectors, solar ponds, and solar-updraft tower-like mechanisms used for collecting solar energy. Density difference and the Rankine cycle are the basic working principles for such systems [9]. Easy design and installation, direct and diffused radiation, relatively rough operation, low maintenance and working cost, and simple operation are a few of the mentioned advantages of the low-temperature thermal concentrator. The overall efficiency of such systems is relatively low compared to medium- and high-temperature systems due to their low operating-temperature range. It may be developed for applications that demand energy at temperatures roughly  $100\text{ }^{\circ}\text{C}$  above ambient [1].

#### 1.4. Flat-Plate Solar-Collecting System

The flat-plate SCS comprises a black-painted flat surface termed an absorber plate, with significant absorption for the incoming irradiation, transparent glass covers, and fluid (air or water) passage, as shown in Figure 4 [12]. The collecting unit is a typical metallic plate that faces the sunlight to absorb insolation, convert it into heat, and transfer it to the working fluid flowing through the SCS [13]. The top of the SCS has a glass cover that allows the incoming insolation to be transmitted and prevents infrared radiation and radiation losses. Using beam and diffuse radiation at a fixed position does not require tracking the sun's path [14].

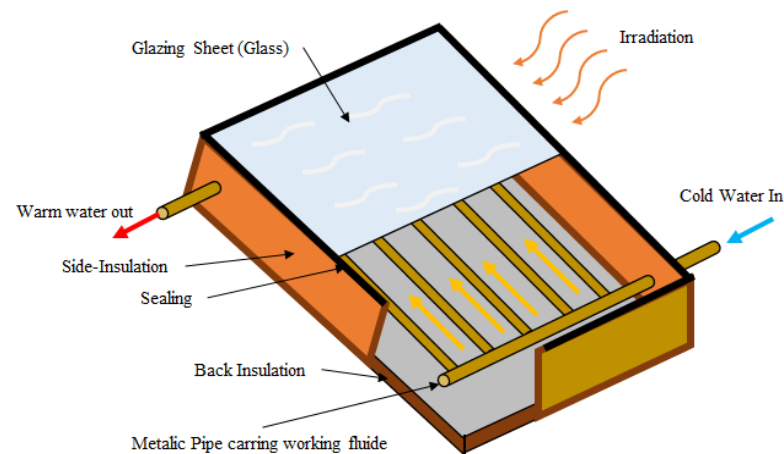


Figure 4. Basic diagram of a flat-plate SCS.

Air collectors require less piping and has no danger of freezing. Its design is relatively simple, and the cost of such a collector is substantially lower than that of the liquid heating system since there is no need for copper tubing. Because of the low air density, the large air volume in the SCS is lower compared to the volume of liquid required in solar water collectors to collect the same amount of energy [1].

The convective heat-transfer coefficient ( $h$ ) among incoming air and the base plate is the major factor limiting the effectiveness of the SCS. There are several methods for enhancing the heat-transfer coefficient. Several researchers have suggested many designs and flow adjustments to boost the  $h$  value for the heated plate and airflow. These involve using corrugated absorber plates, fins, artificial roughness on the surface of the air heating, and packed bed ducts. SCS are the most economical and can be used in almost any sunny place with minor consideration [10], as shown in Figure 5.

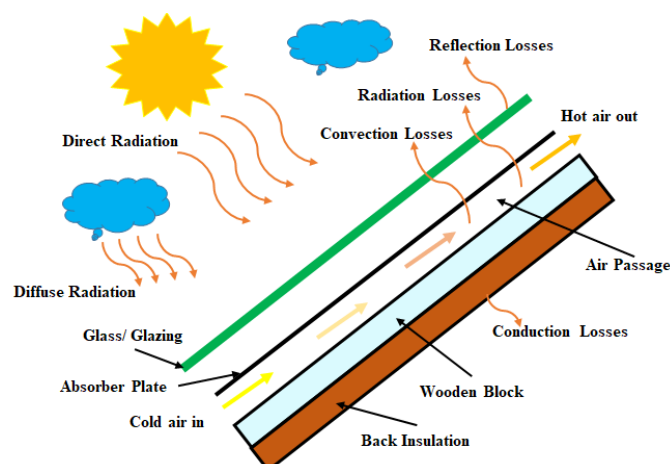


Figure 5. Conventional solar air heater.

### 1.5. Solar Air Heating

A solar air heater (SAH) is a device employed to heat the air as an energy-transfer media that possesses several advantages over liquid. Various problems are associated with liquid solar heaters, i.e., problems of corrosion, leakage of fluid, and power to transfer fluid [15]. All of these problems are eliminated by using air instead of liquid in solar heating devices. The SAH collects chilled air from the bottom of the space and distributes it through the SCS, as shown in Figure 6. Because these simple methods and direct transfers do not store heat, they are ineffective at night or in gloomy conditions [16].

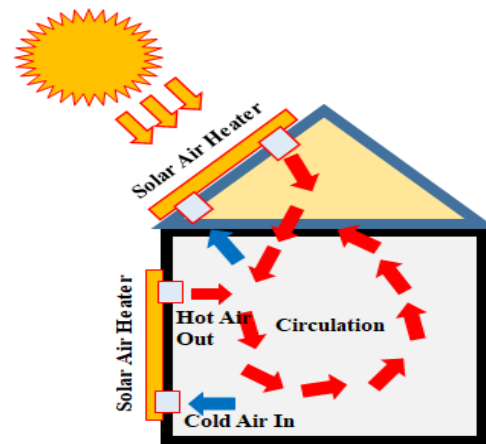


Figure 6. Domestic application of flat-plate collector for house heating.

## 2. Research Objectives

Researchers have been rigorously working on SAH efficiency improvement since the mid-20th century and have also achieved an optimum range of parameters for many types of artificial roughness by applying different approaches available in the domain. As the first paper was published in the 1960s, and after 2000 the average annual scientific production in SAH reached 201 publications by 2021 with an annual growth rate of 8.92% (Figure 7), there is a need for a detailed review assessment of SAH technologies and development assessment so far. Keeping this in mind, the aim of this study covers the following points:

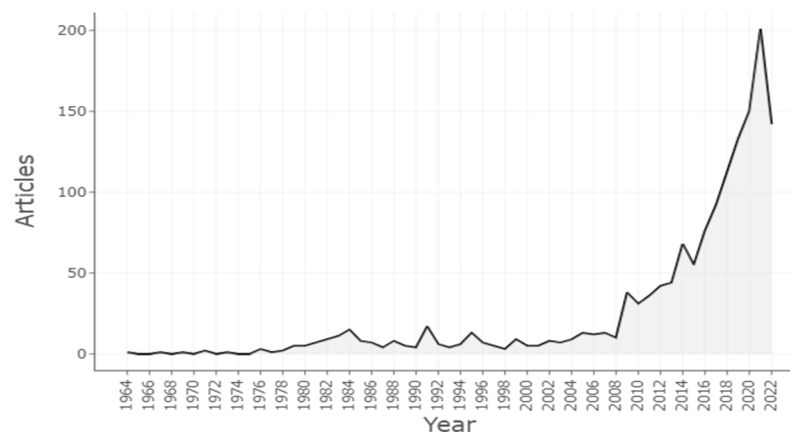


Figure 7. Annual scientific production.

I. To understand the heat-transfer working mechanism and performance-enhancement methods of SAH based on artificial roughness and types of SAH;

II. To become familiar with various forms of artificial-roughness geometry developed so far and the influencing parameters with effective range uses to create a heat-transfer effect;

III. To understand the fundamentals of various roughness approaches used to determine the performance and effectiveness of SAH and provide a suggestion for applications of approaches;

IV. Gap identification of untouched areas for further research and proposed recommendations for the most suitable rib-geometry types and their parameters and the types of solar air heaters developed so far.

### 3. Solar Air-Heater Classification

As per available literature [17], SAH can be classified into various categories, as illustrated in Figure 8. SAHs are classified according to their glass coverings, absorber material, flow characteristics, flow kinds, absorber surface texture, hybrid systems, and applications.

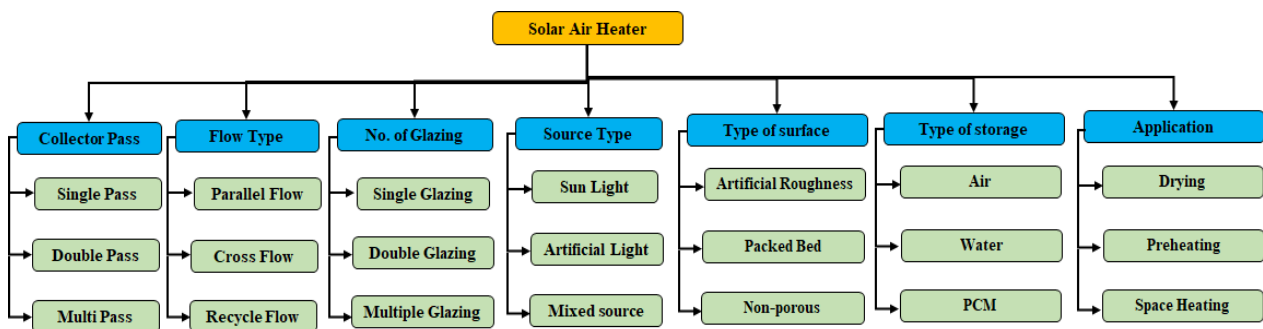


Figure 8. Classifications of SAH.

#### 3.1. Single-Pass SAH

A Single-Pass SAH (SPSAH) has air as a working medium. It has a glass cover, a single flow channel, an absorber plate that has heat-absorbing capacity due to a dark paint or color, and insulation to cover the back side of the channel to decrease the thermal losses to the surrounding area. In general, a blower is attached to the SAH to create a forced circulation of working fluid within the system [2,18–23].

#### 3.2. Double-Pass SAH

Satcunanathan and Deonarine [24] first proposed the Double-Pass SAH (DPSAH) concept to limit top heat losses to the surrounding area. Air passes along both sides of the base plate, extracting heat from the base plate, and then air blows in both directions of the base plate in a double-pass configuration [25]. Different configurations are used to influence the effectiveness of a DPSAH [24,26–30]; DPSAH is further classified based on the direction of working-fluid flow as parallel flow [31–36], counter flow, or cross-flow [37–41], as well as recycling or circular flow [41–45]. The efficiency of a typical DPSAH is 10–15% higher than that of an SPSAH [46]. Figure 9 depicts a traditional double-pass SAH.

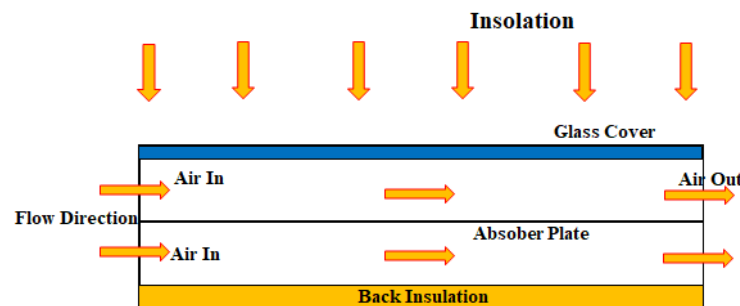


Figure 9. Conventional double-pass SAH.

SAHs were initially invented with a single air pass to use thermal energy from the base plate. Single-pass SAHs have been shown in recent studies to have lower effectiveness

because of a significant heat drop to the surrounding area [47]. The air that travels along the underside of the base surface removes heat, and the airflow that flows above the absorber surface takes back a portion of the heat that has been extracted by the second pass of the DPSAH, resulting in a decrease in total heat loss to the surrounding area [27].

### 3.2.1. Parallel-Flow SAH

In DPPFSAH, the air passes in between the rear insulating layer and the base plate, as shown in Figure 10. The second air pass is positioned slightly above the base plate and in between the glass covers and base plate. Potgieter et al. [48] provided a theoretical model for a DPPFSAH: “the outlet air mean temperature, mean airflow, heat transfer coefficient, and relative humidity could all be predicted using the model.”

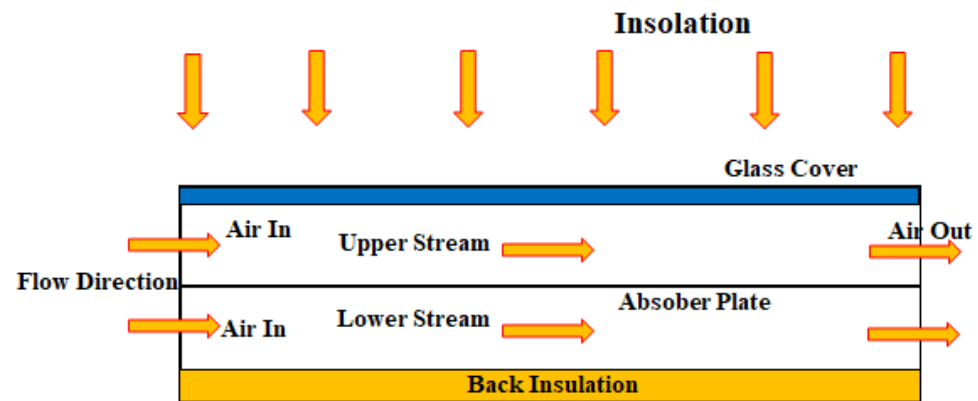


Figure 10. Parallel-flow DPSAH.

The energy equation for the upper airflow is as follows:

$$m_1 C_f \frac{\partial T_{f1}}{\partial t} = h_{c,pf1} (T_p - T_{f1}) - h_{c,f1g} (T_{f1} - T_g) - \frac{G_1 C_f}{W} \frac{\partial T_{f1}}{\partial x} \quad (1)$$

The energy equation for the lower airflow is as follows:

$$m_2 C_f \frac{\partial T_{f2}}{\partial t} = h_{c,pf2} (T_p - T_{f2}) - h_{c,bf2} (T_b - T_{f2}) \quad (2)$$

The energy equation for the absorber plate is as follows:

$$\alpha_p \tau_g I_s - k_p \delta_p \frac{\partial T_p}{\partial x^2} = h_{c,pf2} (T_p - T_{f2}) + h_{c,pf1} (T_p - T_{f1}) + h_{r,pb} (T_p - T_b) + h_{r,pg} (T_p - T_g) + m_p C_p \frac{\partial T_p}{\partial t} \quad (3)$$

The energy equation for the glass cover is as follows:

$$\alpha_g S + h_{r,pg} (T_p - T_g) + h_{c,f1g} (T_{f1} - T_g) = h_{c,gw} (T_p - T_w) + h_{r,ga} (T_g - T_a) + m_g C_g \frac{\partial T_g}{\partial t} \quad (4)$$

The energy equation for the back cover is as follows:

$$h_{r,pb} (T_p - T_b) = h_{c,bf2} (T_b - T_{f2}) + h_b (T_b - T_r) + m_b C_b \frac{\partial T_b}{\partial t} + k_b \delta_b \frac{\partial T_b}{\partial x^2} \quad (5)$$

The following are the beginning and boundary conditions for SAH:

$$T_{f1}(x=0) = T_{fi}, T_{f2}(x=0) = T_{fi} \quad (6)$$

$$\frac{\partial T_p}{\partial x_{x=0}} = 0, \frac{\partial T_p}{\partial x_{x=L}} = 0, \frac{\partial T_b}{\partial x_{x=L}} = 0 \quad (7)$$

Forson et al. [49] constructed a mathematical framework for a DPPFSAH with two glass covers. Various researchers have also developed other theoretical approaches for parallel flow in DPSAHs [49–55]. Furthermore, experimental studies [56–60] for DPPFSAH were conducted, and it was discovered that DPPFSAH outperformed Single-Pass SAH (SPSAH) [56,57].

### 3.2.2. Counter-Flow DPSAH

The counter-flow DPSAH design is attractive because it allows additional heat to be extracted, resulting in improved thermal performance. The design is quite similar to SPSAH [59]. Figure 11 illustrates this setup. The theoretical model for the counter-flow DPSAH, suggested by Verma et al. [61], is as follows:

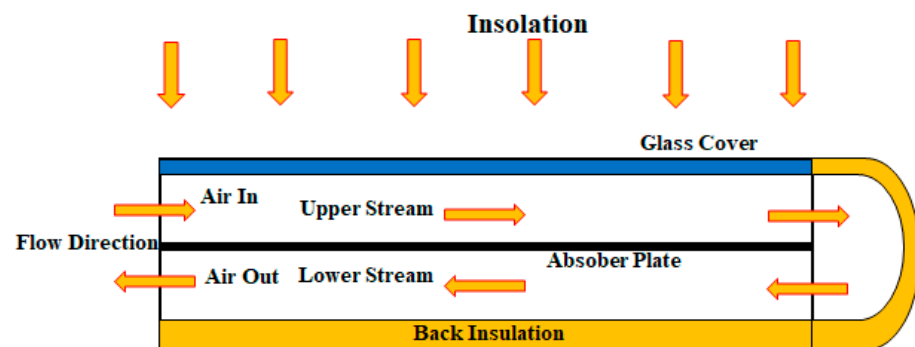


Figure 11. Counter-flow DPSAH.

The energy equation for the upper airflow is as follows:

$$mC_f \frac{\partial T_{f,1}}{\partial x} = h_{c,gf1} (T_g - T_{f1}) - h_{c,f1p} W (T_{f1} - T_p) \quad (8)$$

The energy equation for the lower airflow is as follows:

$$mC_f \frac{\partial T_{f,2}}{\partial x} = h_{c,pf2} W (T_p - T_{f2}) - h_{c,f1b} W (T_{f2} - T_b) \quad (9)$$

The energy equation for the lower absorber plate is as follows:

$$\alpha_p \tau_g S + h_{c,f1p} (T_{f1} - T_p) + h_{r,gp} (T_g - T_p) = h_{c,pf2} (T_p - T_{f2}) + h_{r,pb} (T_p - T_b) \quad (10)$$

The energy equation for the lower glass cover is as follows:

$$\alpha_g S = h_{r,gs} (T_g - T_s) + h_{c,gf1} (T_g - T_{f1}) + h_w (T_g - T_a) + h_{r,gp} (T_g - T_p) \quad (11)$$

The energy equation for the lower-back cover is as follows:

$$h_{c,f2b} (T_{f,2} - T_b) + h_{r,pb} (T_p - T_b) = U_b (T_b - T_a) \quad (12)$$

The boundary conditions are given as follows:

$$T_{f1}(x = 0) = T_{fi}, T_{f1}(x = L) = T_{f2}(x = L) \quad (13)$$

As counter-flow DPSAH has the potential to extract significant thermal energy, the counter-airflow arrangement is a considerable design for improving performance, although significant pressure drop is a primary concern. In counter-flow DPSAHs, the contribution of different thermal performance improvement factors such as porous [62–65], fin [66], packed

wire mesh [67], and V-groove [68] has been studied. Few researchers [69,70], have employed double-glass coverings to reduce overall top-layer thermal losses to increase performance.

### 3.2.3. Recycle or Counter-Flow DPSAH

Air blending and the intensity of forced heat convection have recently proven to have a critical role in heat-transfer augmentation. A similar technique is used in recycle DPSAH, where a part of the heated outflow air is redirected to the intake duct and mixed with new incoming air using a blower. Figure 12 shows a DPSAH with recycling. Ho et al. [42] suggest the following theoretical formulation for recycling operations:

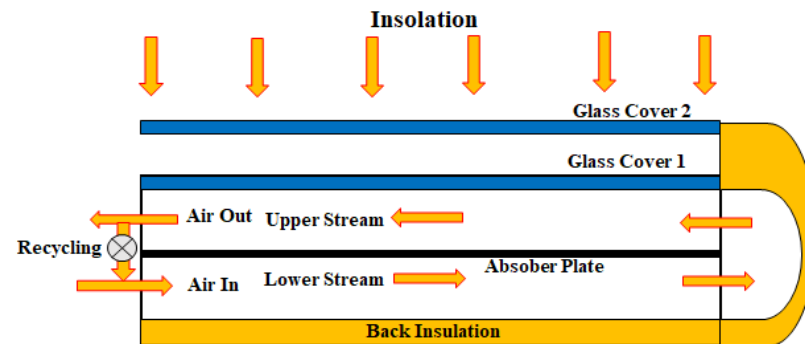


Figure 12. Double-pass SAH with recycling flow.

The absorber-plate energy equation is as follows:

$$\alpha_p \tau_{g1} \tau_{g2} S - h_T (T_P - T_s) + h_b (T_P - T_s) = h_1 (T_P - T_2(x)) + h_2 (T_P - T_1(x)) \quad (14)$$

The energy equation for the back cover is as follows:

$$h_{r,pr} (T_P - T_R) + h' (T_a(x) - T_R) = U_{b1s} (T_P - T_s) \quad (15)$$

The energy equation for the lower airflow is as follows:

$$(1 + R_m) m C_f \frac{\partial T_{f,1}(x)}{\partial x} = h_2 W (T_P - T_a(x)) - h_2' (T_a(x) - T_{Rm}) \quad (16)$$

The energy equation for the upper airflow is as follows:

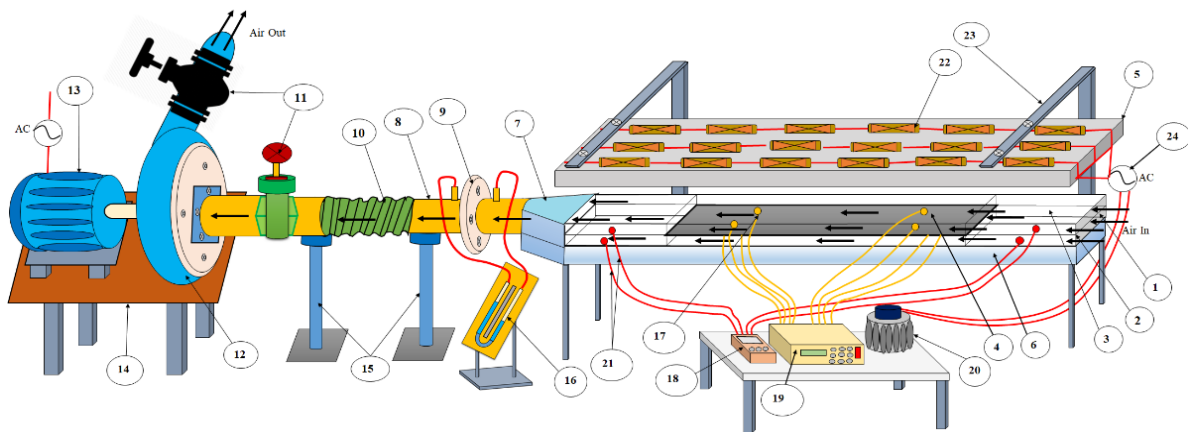
$$(1 + R_m) m C_f \frac{\partial T_{f,2}(x)}{\partial x} = h_1' W (T_b(x) - T_{g1}) - h_1' (T_P - T_b(x)) \quad (17)$$

### 3.2.4. Multi-Pass Solar Air Heater

Using two or more glass coverings is usual practice when the solar air collector operates at relatively high temperatures or is exposed to strong wind. This helps to prevent convection and heat loss from the collector caused by radiation. Because of the absorption and reflection of insolation by the coverings, the amount of solar energy contacting the heated surface is reduced when many glass covers are used [71].

## 4. Experimental Setup

For the purpose of estimating the effectiveness of an artificially roughened SAH, the experimental results of thermo-hydraulic performance (THP) for a given roughness configuration are required [60]. To assure the accuracy of experimental findings, it is necessary to conduct experiments using a verified experimental setup under established test circumstances. Figure 13 depicts a schematic of the indoor test rig of a DPPFSAH for generating data on THP in an artificially roughened SAH as per ASHRAE standard 93-77 [72].



|                                 |                               |                                   |
|---------------------------------|-------------------------------|-----------------------------------|
| 1. Entry Section                | 9. Orifice Plate              | 17. Thermocouples                 |
| 2. Wooden Duct                  | 10. Flexible pipe             | 18. Micro- manometer              |
| 3. Transparent Glass            | 11. Flow Control Valve        | 19. Data Acquisition System (DAQ) |
| 4. Absorber plate               | 12. Centrifugal blower        | 20. Variac                        |
| 5. Halogen tubes ( Heat Source) | 13. Electric Moter            | 21. Pressure pipes                |
| 6. Thermal Insulation           | 14. Support Table             | 22. Halogens                      |
| 7. Exit Section                 | 15. Supporting stand          | 23. Halogen Stand/Frame           |
| 8. PVC Pipe                     | 16. Inclined U-tube manometer | 24. Power Supply                  |

Figure 13. Experimental setup schematic of DPPFSAH.

### 5. Thermal Performance of Flat-Plate SAH

The thermal performance of an SAH refers to its ability to improve heat transmission. The effectiveness of an SAH is the energy balance, comprised of the solar-irradiation energy yield to the collectors, the useable energy gained by airflow, and the losses to the environment. For calculating the usable energy gain from the air, Hottel–Woertz [73] suggested the below-mentioned energy equation.

The energy balance under controlled conditions for a collector is given as:

$$Q_u = [I(\tau\alpha) - U_t(T_{pm} - T_a)] \quad (18)$$

where

$Q_u$  = useful heat gain,  $W/m^2$ ;

$U_t$  = total loss coefficient,  $W/m^2K$ ;

$T_{pm}$  = average plate temperature, K;

$T_a$  = ambient temperature, K.

The effective transmittance absorptance product ( $\tau\alpha$ ) is a factor that handles the dynamic interactions of the optical characteristics of the glass and the absorber surface. In reality, the configuration of the absorber, incident solar energy, fluid velocity, and fluid characteristics all influence the mean temperature of the base plate. Bliss [74] devised an alternative expression in terms of mean fluid temperature,  $T_{fm}$ , that includes a variable known as the collector-efficiency factor  $F'$ :

$$Q_u = F' [I(\tau\alpha) - U_l(T_{fm} - T_a)] \quad (19)$$

However, the mean absorber-plate temperature,  $T_{pm}$ , and average fluid temperature,  $T_{fm}$ , are generally unknown. Bliss [74] modified the above equation for more practical use and is given as follows:

$$Q_u = F_R [I(\tau\alpha) - U_l(T_{fi} - T_a)] \quad (20)$$

where the heat-removal factor ( $F_R$ ) given by Hottel–Whillier [73] and mentioned by Duffie and Beckman [5] can be calculated as follows:

$$F_R = \frac{\dot{m}C_p}{U_l} \left[ 1 - \exp\left(\frac{-F'U_l}{\dot{m}C_p}\right) \right] \quad (21)$$

The thermal efficiency ( $\eta_{th}$ ) of an SAH can be calculated as:

$$\eta_{th} = \frac{Q_u}{I} \quad (22)$$

From Equations (18)–(22), the following relationships can be obtained:

$$\eta_{th} = \left[ \tau\alpha - U_l \frac{(T_{pm} - T_a)}{I} \right] \quad (23)$$

$$\eta_{th} = F' \left[ \tau\alpha - U_l \frac{(T_{fm} - T_a)}{I} \right] \quad (24)$$

$$\eta_{th} = F_R \left[ \tau\alpha - U_l \frac{(T_{fi} - T_a)}{I} \right] \quad (25)$$

The above Equations (23)–(25) are recognized as the Hottel–Whillier–Bliss equations. Bondi [75] provided the expression for SAH thermal efficiency ( $\eta_{th}$ ) that applies to the air-outlet temperature to calculate the  $\eta_{th}$  of SAH when pulling air from the atmosphere:

$$\eta_{th} = F_o \left[ \tau\alpha - U_l \frac{(T_{fo} - T_{fi})}{I} \right] \quad (26)$$

where  $F_o$  is the heat-removal factor based on the temperature of the output air and is written as:

$$F_o = \frac{\dot{m}C_p}{U_l} \left[ \exp\left(\frac{F'U_l}{\dot{m}C_p}\right) - 1 \right] \quad (27)$$

## 6. Heat Transfer in Conventional (Smooth) Collectors

Several empirical heat-transfer correlations exist for the collectors' different configurations and working conditions. Kays [76] proposed correlations for thermal effectiveness for fully developed flow between parallel plates, with the upper plate heated and the lower plate insulated:

(i) For laminar flow ( $Re < 2000$ ):

$$h = 4.364 \frac{K}{D_e} \quad (28)$$

(ii) For turbulent flow ( $Re > 2000$ ):

$$Nu = 0.0158 Re^{0.8} \quad (29)$$

Bondi et al. [75] modified the correlation proposed by Kays [76] by introducing the geometrical coefficient of collector  $K$ .  $L$  is the collector length, and  $b$  is the thickness of the air duct.

$$Nu = 0.0158 \left[ \frac{G_0'K}{u} \right]^{0.8} D_e \quad (30)$$

where

$$K = L/(bD_e)^{0.25}$$

$L$  = collector length and  $b$  = thickness of the air duct.

Kays [76] proposed a correlation between thermal performance and the friction factor ( $f$ ) for turbulence flow in a tube as follows:

$$Nu = \frac{\left(\frac{f_0}{2}\right) Re Pr}{1.07 + 12.7\left(\frac{f_0}{2}\right)^{0.5} (Pr^{\frac{2}{3}} - 1)} \quad (31)$$

$$f_0 = [0.79 \ln Re - 1.64]^{-2.0}$$

Majumdar [77] used an experimental approach for large Reynolds numbers and high Prandtl numbers to develop an equation incorporating the transition region and fully developed flow region into pipes and channels. He recommended the following correlations:

$$u = \frac{\left(\frac{f_0}{2}\right) (Re - 1000) Pr}{1.0 + 12.7\left(\frac{f_0}{2}\right)^{0.5} (Pr^{\frac{2}{3}} - 1)} \quad (32)$$

Equation (32) holds in the Reynolds number ( $Re$ ) range of  $2300 < Re < 10^4$  and Prandtl number ( $Pr$ )  $0.5 < Pr < 200$ .

Niles [78] developed the following correlation to establish the  $h$  value in between the heated base plate and the duct's circulating air:

$$Nu = 0.033 Re^{4/5} Pr^{1/3} \quad (33)$$

Based on experimental data for circular tubes [79], the following correlations, which are known as Dittus and Boelter relations, are used:

$$Nu = 0.024 Re^{0.8} Pr^{0.3} \quad (34)$$

- (i) For cooling
- (ii) For heating

$$Nu = 0.026 Re^{0.8} Pr^{0.3} \quad (35)$$

These correlations apply for  $0.7 \leq Pr \leq 120$  and  $2500 \leq Re \leq 1.24 \times 10^5$ .

## 7. Testing of Solar Air Collector

An SAH performance may be determined using SAH efficiency with the ratio of helpful energy gain to solar radiation during a limiting time. Mathematically, it can be expressed as;

$$\eta = \frac{\int_0^\theta Q_u d\theta}{A_c \int_0^\theta I d\theta} \quad (36)$$

where

- $\eta$  = average collector efficiency over a period of time;
- $I$  = intensity of global incident radiation,  $W/m^2$ ;
- $Q_u$  = useful heat gains over a period of time;
- $A_c$  = collector-plate area,  $m^2$ ;
- $\theta$  = time interval, seconds.

For any short period, the  $\eta_{th}$  of a collector is simply the ratio of the rate of useable energy to the intensity of incoming radiation at that precise moment in time and may be expressed as:

$$\eta_{th} = \frac{Q_u}{I} \quad (37)$$

The thermal efficiency ( $\eta_{th}$ ) can be expressed as:

$$\eta_{th} = \frac{\dot{m}C_p(T_{fo} - T_a)}{IA_c} \quad (38)$$

The  $\eta_{th}$  evaluations of the solar collector are required to obtain the fundamental design data utilized to develop collector systems. (a) The National Bureau of Standards (NBS) [80] and (b) the American Society of Heating Refrigeration and Air Condition Engineering (ASHRAE) standards 93-77 [81] are the two techniques for solar-collector standard testing.

NBS recommends the following  $\eta_{th}$  equation:

$$\eta_{th} = F' \left[ \tau\alpha - U_l \frac{(T_{fm} - T_a)}{I} \right] \quad (39)$$

The ASHRAE [81] recommended the following equation for  $\eta_{th}$ :

$$\eta_{th} = F_R \left[ \tau\alpha - U_l \frac{(T_{fi} - T_a)}{I} \right] \quad (40)$$

where  $F_R$  = receiver heat-removal factor.

Reddy and Gupta [82] provided a graphical method of deciding the configuration for a solar collector of predefined specifications. The  $\eta_{th}$  can be indicated in the following set of equations.

**Case A:** with air recycling, i.e., ( $T_{fi} > T_a$ )

$$\eta_{th} = F' \left[ \tau\alpha - U_l \left\{ \frac{(T_{fo} - T_a) + (T_{fi} - T_a)}{I} \right\} \right] \quad (41)$$

$$\eta_{th} = 2\dot{m}C_p \left[ U_l \left\{ \frac{(T_{fo} - T_a) + (T_{fi} - T_a)}{I} \right\} \right] \quad (42)$$

**Case B:** without air recycling, i.e., ( $T_{fi} = T_a$ )

$$\eta_{th} = F' \left[ \tau\alpha - U_l \left\{ \frac{(T_{fo} - T_a)}{2I} \right\} \right] \quad (43)$$

$$\eta_{th} = F' \left[ \tau\alpha - U_l \left\{ \frac{(T_{fo} - T_a) + (T_{fi} - T_a)}{2I} \right\} \right] \quad (44)$$

$$\eta_{th} = 2\dot{m}C_p \left[ \left\{ \frac{(T_{fo} - T_a)}{2I} \right\} \right] \quad (45)$$

These characteristics are shown in Figure 14, known as design curves, given by Reddy and Gupta [82].

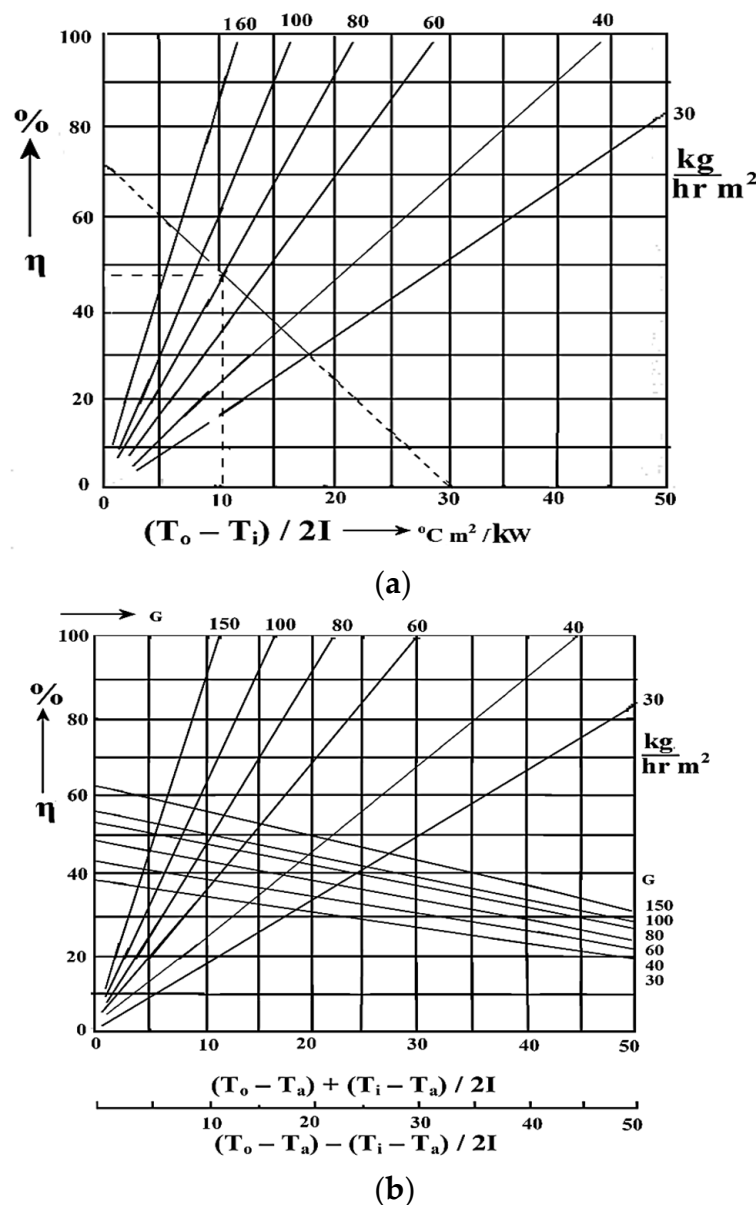


Figure 14. Design curves (a) with air recycling and (b) without air recycling [78].

## 8. Performance-Enhancement Methods of Solar Air Heaters

As discussed above, conventional SAH is used for crop-drying and room-heating applications. It utilizes the air as a heat-transfer medium, which lowers the risk of corrosion and freezing in solar collectors and provides a lightweight and low-cost collector. However, substantial pressure losses occur with lower specific heat and air density and require sizeable volumetric-flow rates [83]. In addition, the lower value of the air's thermal conductivity causes more excellent heat-transfer resistance and a large temperature gradient for the heated plate and airflow; its efficiency is low. Because of this, it must carry the construction of the airflow channel and the heat-collecting surface of the SAH out with a significant energy-extraction rate and minimum pressure losses [84–89].

To achieve this purpose, various investigators have suggested several variations in the design of conventional SAH [43,47,51,71,90–106]. An overview of the literature of various studies related to performance-enhancement techniques for conventional solar air-heating systems are added in this section. The techniques and design modifications related to enhancements in heat-transfer coefficient, solar-radiation flux, and reductions in heat losses are shown in Figure 15.



Salih et al. [108] investigated an indoor flat-plate DPSAH with and without phase-transition material based on paraffin wax (PCM) at various air mass-flow rates and continuous irradiance of  $625 \text{ W/m}^2$ . The results revealed that with an airflow rate of  $1.8 \text{ kg/min}$ , the optimum performance achieved for the DPSAH with and without PCM was 63.53% and 68.23%, respectively, and that values substantially depended on the flow velocity.

### 8.2. Enhancing the Solar-Radiation Flux

#### Use of Reflectors

Flat-plate solar collectors can be made more energy efficient by using reflective surfaces, dramatically enhancing performance. The booster system with a flat-plate SAH, as shown in Figure 17, may achieve a four-times-higher temperature range of up to  $180 \text{ }^\circ\text{C}$ . Bhowmik employed flat reflectors [109] to improve the system's performance.

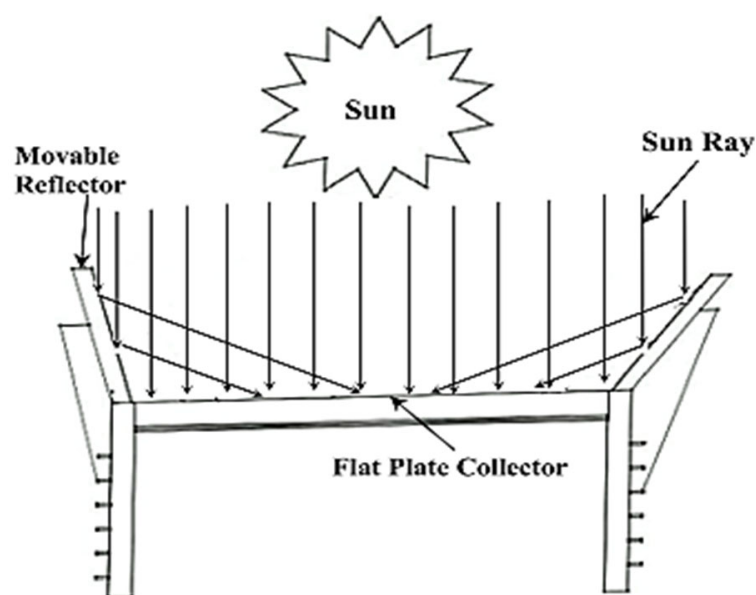


Figure 17. Flat absorber with booster mirror, reprinted with permission from [105], 2022, Elsevier.

### 8.3. Reducing Thermal Losses

#### 8.3.1. Use of Multiple Glass Covers

Installing two or more glass coverings is usual practice whenever the SAH operates at relatively high temperatures or is exposed to substantial wind velocity. This helps to prevent convective heat loss from the collector because of radiation. Along with the reflection and absorption of solar insolation by the glass coverings, the amount of solar energy reaching the heated plate is reduced when many glass covers are used [73]. For various operating conditions, Samdarshi and Mullick [110] provided mathematical equations for the maximum heat-loss coefficient of a flat-plate SAH with two or more numbers of glazing.

#### 8.3.2. Configuration with Double-Exposure Orientation

Sauka [111] constructed a reduced form of a double-pass solar collector. It is made of a passage connecting two parallel plates, one of which is darkened to absorb solar radiation. As shown in Figure 18, the back plate can be darkened and radiated, whereas the back insulation is removed and adequate reflectors are used. This is referred to as a dual-exposed air collector. Suri and Saini [112] used a set of generalized performance prediction curves to examine single- and double-exposed air collectors.

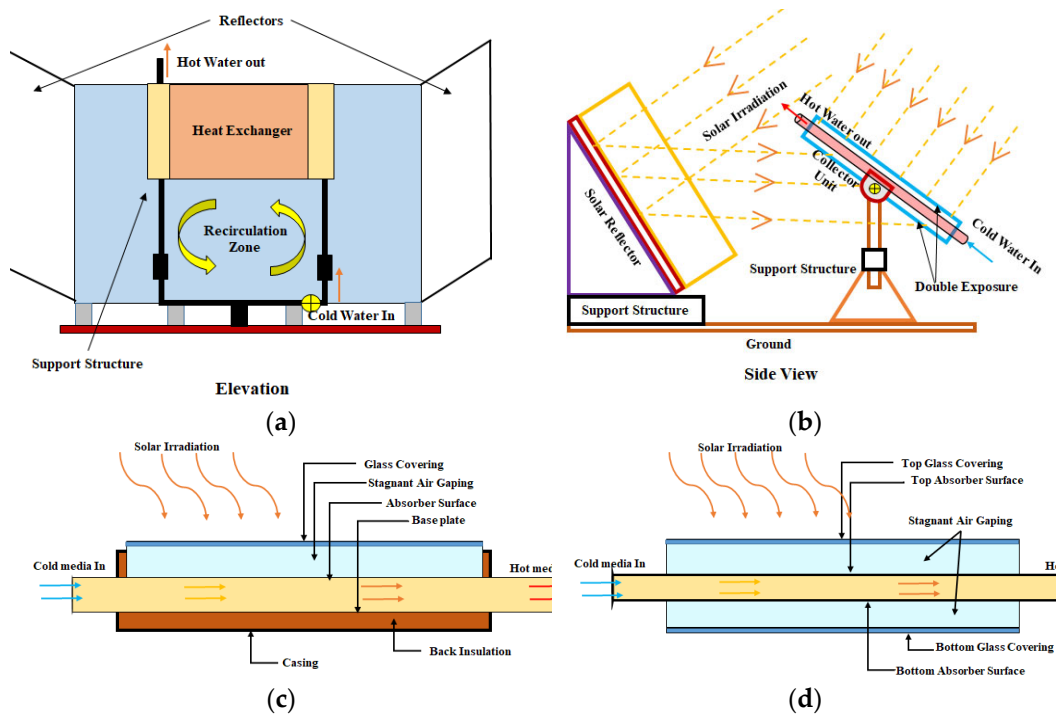


Figure 18. (a,b) Double-exposure solar collector, reprinted with the permission from ref. [107], 2022, Elsevier; (c,d) single- and double-exposure solar collector; reprinted with the permission from ref. [108], 2022, Elsevier.

### 8.3.3. Overlapped Glass-Cover Arrangement

The solar air collector comprises a set of overlapping parallel coverings, the lower one being darkened, as shown in Figure 19. The air flows parallel to and between the glass coverings. At the entrance, a honeycomb cell structure channels the airflow and confirms that its velocity remains in quasi-condition. This type of collector was first used by Löf [113,114] in a residential solar-heating system in Colorado. Selcuk [115] conducted experiments and theoretical analyses of the SAH and observed an improvement in its thermal performance. This kind of collector has a minimal drop in pressure, which is a benefit. The needed glass area is about four times larger than the collection area.

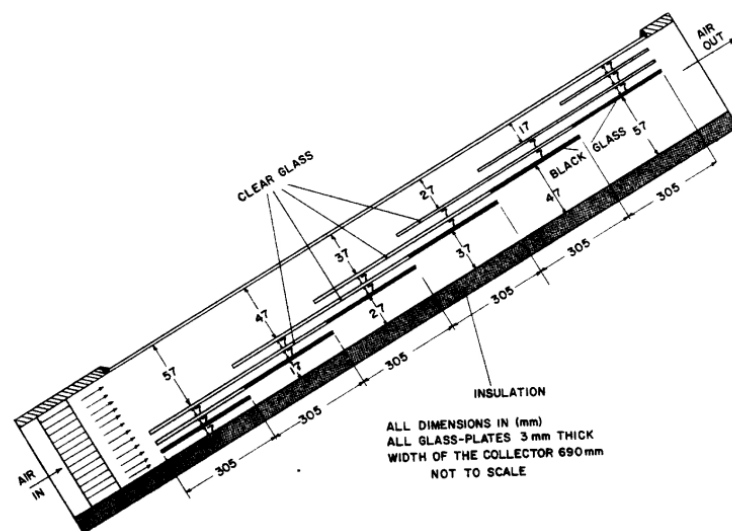
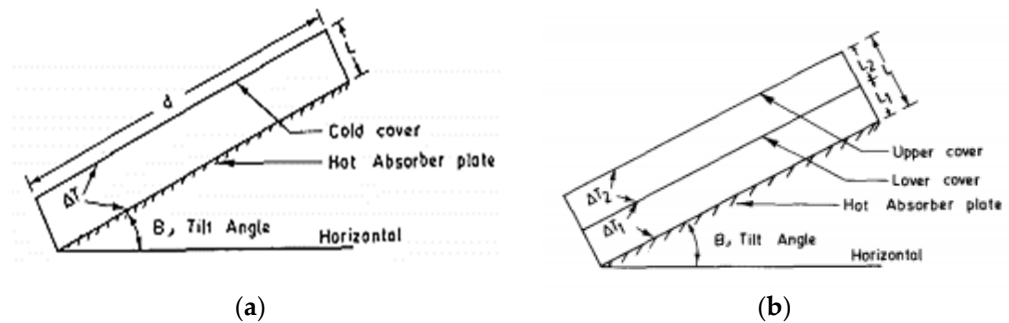


Figure 19. Overlapped glass-cover solar air collector, reprinted with permission from [111], 2022, Elsevier.

### 8.3.4. Evacuated Tube Collector

Using evacuated tubes can reduce convective heat loss from the top glass cover, as illustrated in Figure 20. According to Malhotra et al. [116], using heavier gases can minimize heat losses by 34%. Alternatively, at a 10% drop in pressure, the partial evacuation gap can significantly minimize thermal losses.



**Figure 20.** Application of (a) single- and (b) double-evacuated tube solar air collector, to minimize the heat losses, reprinted with permission from [112], 2022, Elsevier.

### 8.3.5. Using Selective Absorber Surface

Duffie and Backman [10] discussed the characteristics of selective surface coatings such as black nickel on galvanized iron, black copper and ebanol carbon on copper, and black chrome on nickel-plated steel. The highly selective surfaces of the absorber plate require only a clean cover, even at significantly high temperatures.

### 8.3.6. Using Honeycomb Structures

To decrease the convection and radiation losses of the transparent cover, honeycomb modules were formed and sprayed with thin, highly reflective yet infrared-heated surfaces. Abuška et al. [117] conducted an experimental analysis on SAH with PCM with honeycomb under natural convection, as shown in Figure 21a. The thermal-effectiveness observation during sunlight was calculated as 10.1%, 10.9%, and 13.6%. Honeycomb significantly decreases the absorber's thermal-radiation losses. As shown in Figure 21b, Buchberg [118,119] designed a collector comprising a multiple glass-cell array with substantially specular reflecting surfaces covered with a dielectric layer. Solar energy passes through the layer while longwave radiation is absorbed. Measurements were taken using a test module with a honeycomb of rectangular honeycombs that produced a high collection efficiency.

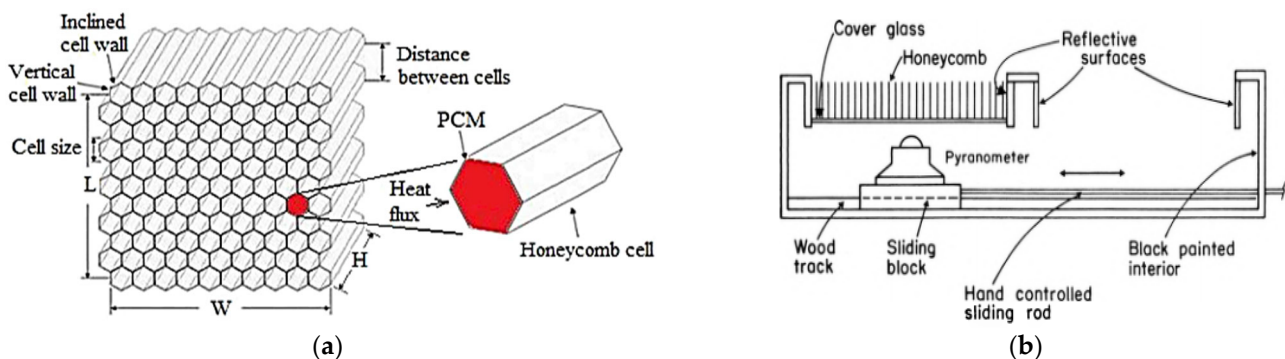


**Figure 21.** (a) Honeycomb geometry, reprinted with permission from [113], 2022, Elsevier and (b) schematic of honeycomb air-collector test apparatus [114].

### 8.3.7. Using Double-Pass Arrangement

A two-pass design helps reduce transmission losses. Satcunanathan and Deonarine [24] were the first to study the notion of a DPSAH, followed by Caouris et al. [120]. These

researchers tested the double-passage concept with air flowing in two different channels and discovered that heat losses from the glass cover could decrease using such approaches. The DPSAH has a higher thermal performance than SPSAH. Wijeyesundera et al. [70] constructed and examined a thermal model for a DPSAH and related the findings to a SPSAH, as given in Figure 22. Mohamad [121] discussed a new form of counter-flow SAH. Blowing air to travel via two air passageways helps decrease energy loss from the glass. Before passing over the absorber plate, air travels through two glass covers and is warmed. When compared to a traditional SAH, this one had greater efficiency.

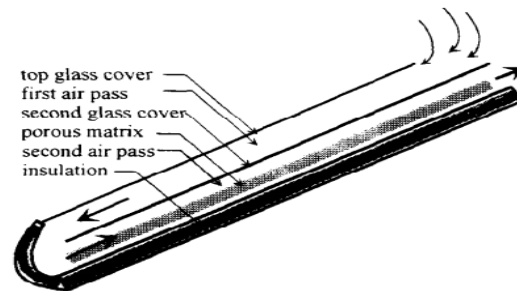


Figure 22. DPSAH diagram, reprinted with permission from [117], 2022, Elsevier.

Prasad and Satcunanathan [122] created a mathematical model to evaluate SPSAH and DPSAH effectiveness with two glass coverings, as shown in Figure 23. The effectiveness of a DPSAH depends on the collector temperature. The effect of airflow rate and collector length on the effectiveness of double-pass parallel-flow SAH (DPPFSAH) was investigated by Sodha et al. [123]. Because the thermal gradient was higher with double flow even though 50% of the air was flowing above and the other half underneath the same base plate, it was observed that the thermal performance of the DPSAH was preferable to the SPSAH for the same range of working parameters. It was also discovered that twin glass covers improved collector efficiency only for low flow rates.

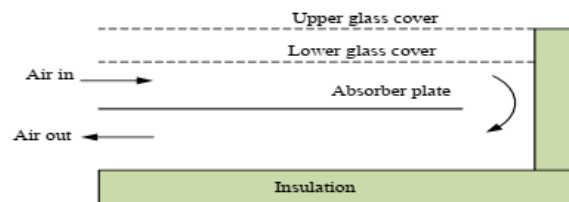


Figure 23. Diagram of counter-flow DPSAH, reprinted with permission from [118], 2022, Elsevier.

Choudhary et al. [124] evaluated the costs and effectiveness of the counter-flow SAH with single- and double-glass coverings above the absorber plates to the SPSAH without glass coverings, as shown in Figure 24.

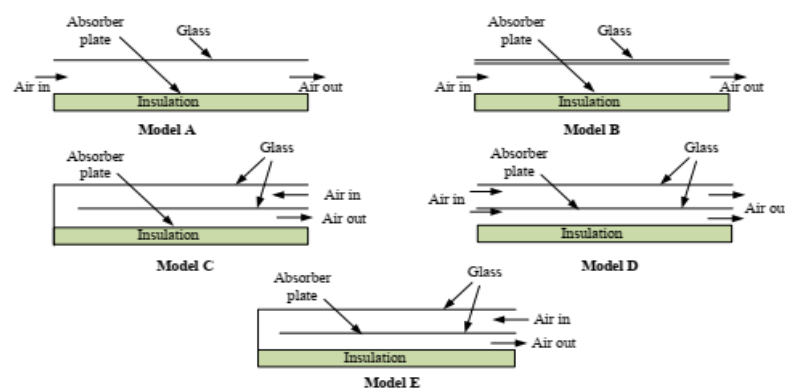


Figure 24. Schematic diagram of SAHs, reprinted with permission from [120], 2022, Elsevier.

### 8.4. By Reducing Loss Coefficient

#### 8.4.1. Evaluation of Loss Coefficients

The precise estimation of the heat-loss coefficient ( $U_L$ ) is critical for evaluating the solar collector's efficiency. The overall heat-loss coefficient is the integration of the top-, bottom-, and side-loss coefficients  $U_T$ ,  $U_B$ , and  $U_E$ , respectively, and can be expressed as:

$$U_L = U_T + U_B + U_E \quad (46)$$

#### Top-Loss Coefficient

The most significant heat loss in a flat-plate SAH is from above the transparent glass cover. The calculations of the top-loss coefficient ( $U_T$ ) are tedious processes that require trial-and-error methodology. Hottel and Woertz [73] proposed a basic semi-empirical equation, which was changed later on by Klein [10,125]:

$$U_T = \left[ \frac{N_g}{\frac{C_t}{T_{pm}} \left\{ \frac{T_{pm} - T_a}{N_g + f_t} \right\}^{0.25} + \frac{1}{h_w}} \right]^{-1.0} + \left[ \frac{\sigma(T_{pm}^2 + T_a^2)(T_{pm} + T_a)}{\left( \frac{1}{\varepsilon_p} + \frac{(2N_g + f_t - 1)}{\varepsilon_p} - N_g \right)} \right] \quad (47)$$

Duffie and Beckman [10] developed the following correlation, which is helpful for both hand and computer calculation. It is applicable for the mean temperature of the absorber plate up to 200 °C and can predict  $U_T$  within  $\pm 0.3$  W/m<sup>2</sup> °C.

$$U_T = \left[ \frac{N_g}{\frac{C_t}{T_{pm}} \left\{ \frac{T_{pm} - T_a}{N_g + f_t} \right\}^e + \frac{1}{h_w}} \right]^{-1.0} + \left[ \frac{\sigma(T_{pm}^2 + T_a^2)(T_{pm} + T_a)}{\left( (\varepsilon_p + 0.00591N_g h_w)^{-1.0} + \left[ \frac{(2N_g + f_t - 1) + 0.166\varepsilon_p}{\varepsilon_p} \right] - N_g \right)} \right] \quad (48)$$

$$f_t = (1.0 + 0.089h_w - 0.1166h_w\varepsilon_p) + (1 + 0.07866N_g) \quad (49)$$

$$e = 0.043 \left( 1 - \frac{100}{T_{pm}} \right) \quad (50)$$

$N_g$  is the number of glass covers;

$C_t = 520(1 - 0.000051 s^2)$  for  $0^\circ \leq \beta \leq 90^\circ$  use  $\beta = 70^\circ$ ;

$T_p$  = average plate temperature, K;

$B$  = collector tilt angle, °;

$h_w$  = convective heat-transfer coefficient, W/m<sup>2</sup>-K;

$\varepsilon_p$  = absorbing-plate emissivity;

$\varepsilon_g$  = glass-cover emissivity;

$\sigma$  = Stefan-Boltzman constant ( $5.6697 \times 10^{-8}$ , W/m<sup>2</sup>K<sup>4</sup>)

The set of above equations shows an excellent agreement for the highly selective ( $\varepsilon_p = 0.1$ ) and non-selective ( $\varepsilon_p = 0.95$ ) regimes, whereas the value differs significantly in the moderately selective regimes ( $\varepsilon_p = 0.4$  to  $0.7$ ). Agarwal and Larson [126] proposed a new statistical correlation for the estimation of  $U_T$ , with tilt-angle effect and gap spacing.

$$U_T = \left[ \frac{N_g}{\frac{204.43}{T_{pm}} \left\{ \frac{L_s^3 \cos s(T_{pm} - T_a)}{(N_g + f_t)} \right\}^{0.252} L_s^{-1} + \frac{1}{h_w}} \right]^{-1.0} + \left[ \frac{\sigma(T_{pm}^2 + T_a^2)(T_{pm} + T_a)}{\left\{ (\varepsilon_p + 0.00425N_g(1 - \varepsilon_p))^{-1.0} + \left[ \frac{(2N_g + f_t - 1) + 0.133\varepsilon_p}{\varepsilon_p} \right] - N_g \right\}} \right] \quad (51)$$

where

$$f_t = \left[ \frac{9}{h_w} - \frac{9}{h_w^2} \right] \left[ \frac{T_a}{316.9} \right] (1 + 0.091N_g)$$

### Bottom-Loss Coefficient

The two terms represent the energy loss from the downside of the SAH: first, the conduction heat loss by insulation; and second, losing due to radiation and convection from the bottom of the SAH to the environment. Therefore, the bottom-loss coefficient ( $U_B$ ) can be estimated as:

$$U_B = \left[ \frac{T_{ins}}{K_{ins}} + \frac{9}{h_b} \right]^{-1.0} \quad (52)$$

### Side- or Edge-Loss Coefficient

The edge-loss coefficient ( $U_e$ ) can be evaluated with the following equation, which is based on the collector area:

$$U_e = \frac{(U_e A)_{edge}}{A_c} \quad (53)$$

where  $(U_e A)_{edge}$  shows the edge-loss coefficient is a product of the solar collector, where  $U_e$  is suggested to be  $0.50 \text{ W/m}^2\text{K}$  by Klein [125].

## 8.5. Enhancing the Heat-Transfer Coefficient

### 8.5.1. Jet-Plate Arrangement

Performance evaluation of jet SAH has been conducted by various research scholars [127–130]; Choudhury and Garg [130] explored an SAH using a jet plate, as seen in Figure 25. The impinging air jet, which improves overall thermal efficiency, increases the heat-recovery rate from the heated surface.

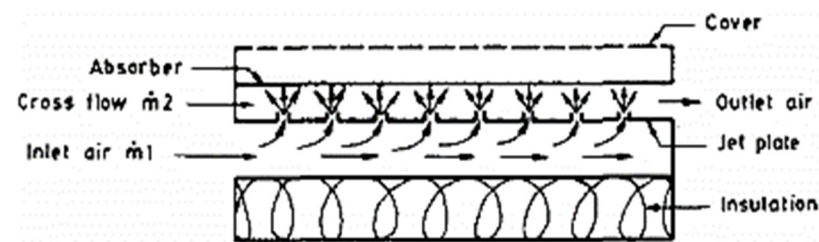


Figure 25. Jet-plate solar collector, reprinted with permission [126], 2022, Elsevier.

### 8.5.2. Using Extended Surface

Extended surfaces inside the airflow passages, such as fins and turbulators, give a greater area for heat exchange, increasing the convection coefficient of heat transfer and the duct's thermal performance [131]. Yeh et al. [132,133] investigated the effectiveness of finned geometry with smooth-plate DPSAH (both theoretically and experimentally). The best airflow proportion for optimum efficiency was determined to be unity, implying that the airflow rate in both flow tubes should be identical in the DPSAH with extended fins connected to each face of the base plate, as seen in Figure 26. Naphon [66] developed modelling for thermal performance analysis. It was observed that as fin height and number increased, thermal efficiency increased whereas entropy generation decreased. Fudholi et al. [34] examined the effects of flow rate, elevation, and frequency of fins on the effectiveness of the DPSAH channel, as shown in Figure 27. The efficacy of the collector was determined to be a significant function of flow rate.

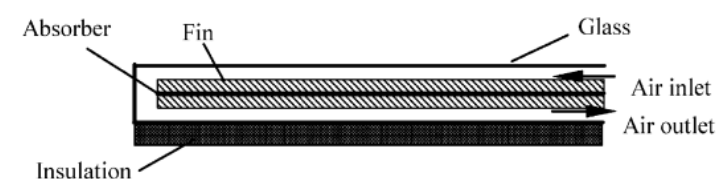
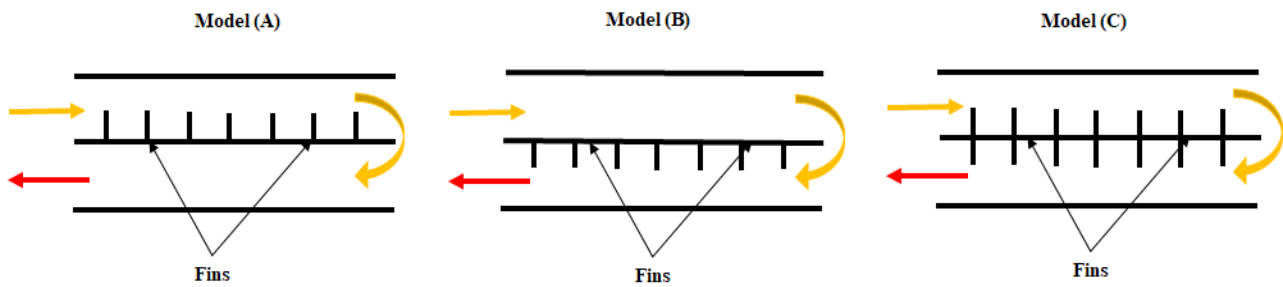


Figure 26. DPSAH with extended surfaces, reprinted with permission [63], 2022, Elsevier.



**Figure 27.** Diagram of the DPSAH comprising (a) upper-longitudinal fins, (b) lower-longitudinal fins, and (c) both fins [31].

### 8.5.3. Using Obstacles on the Absorber Plate

Ozgen et al. [33] analyzed the effectiveness of a DPSAH with aluminum as extended surface attachments on the base plate. The heat-collecting surface was arranged in three different ways, as shown in Figure 28. It was shown that the DPSAH with aluminum cans improved the heat-transfer area and induced turbulent flow, increasing the convection coefficient. As the airflow rate reached 0.05 kg/s, the thermal efficiency of cans with the staggered arrangement was determined to be the highest.

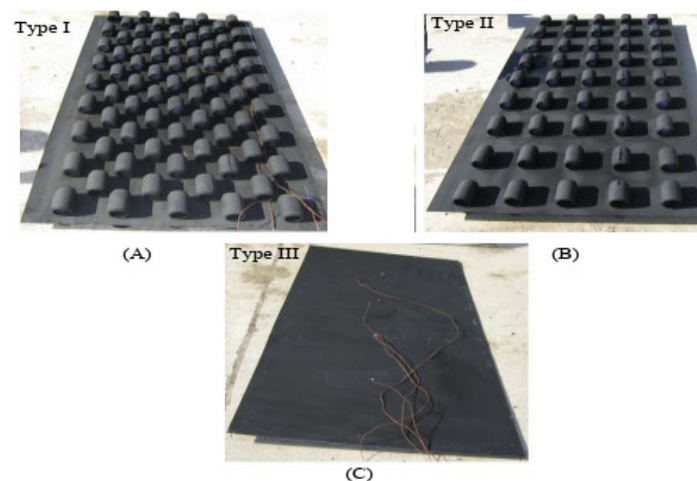


**Figure 28.** Absorber configuration: (A) aluminum containers with a stagger configuration; (B) containers with an inline configuration; (C) a flat duct without containers, reprinted with permission [30], 2022, Elsevier.

### 8.5.4. Using Corrugated Absorber

Joudi and Mohammad [134] studied V-corrugated roughness with flow rates ranging from 0.016 to 0.0385 kg/s and found that the collector efficiency was 42%. Using recycling, Dhiman and Singh [53] investigated flat and V-corrugated roughness in DPSAH (Figure 29). EI-Sebaili et al. [69] discovered that the heat-transfer rate of the flat-plate and V-corrugated plate collector increased with the increased airflow rate before 0.04 kg/s was attained, beyond which the thermal effectiveness of the two systems was deemed insignificant. The DPSAH with V-corrugated roughness was 11–14% more efficient than the smooth DPSAH. When the airflow rate was 0.02 kg/s, the thermohydraulic effectiveness of the two heaters under investigation reached its maximum. Karim et al. [35] published a theoretical simulation code in MATLAB to investigate the air temperature at the intake and outlet sections and plate temperature at any section of a counter flow V-groove-collector-type SAH.

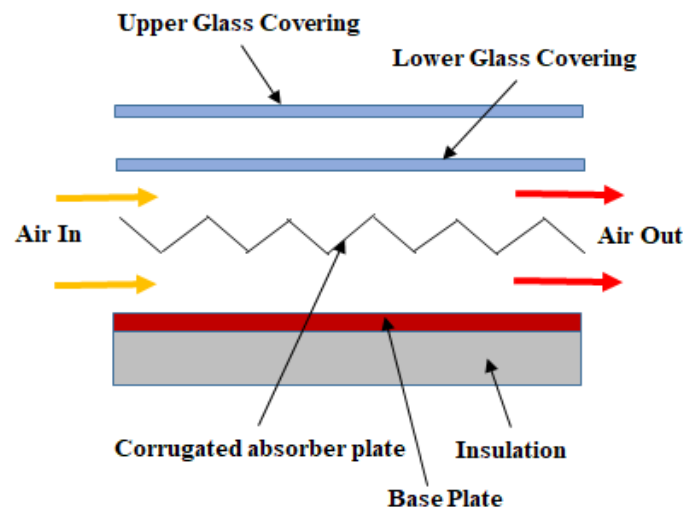


Figure 29. DPSAH with corrugated absorber plate; reprinted with permission from ref. [66], 2022, Elsevier.

#### 8.5.5. Using Twisted-Tape Inserts

Using a twisted-tape swirl generator in a straight, smooth pipe or duct is a well-known heat-transfer augmentation technique with a solid practical and theoretical foundation from previous studies. Using a basic superposition model, Hong and Bergles [135] sought to account for the higher flow speed (produced by the spiral flow) and the centrifugal buoyancy effect. Figure 30 depicts the explored geometry. Wen et al. [136] experimented to find the properties of the enhanced thermal performance and pressure reduction by different strip-type inserts in a small segment.

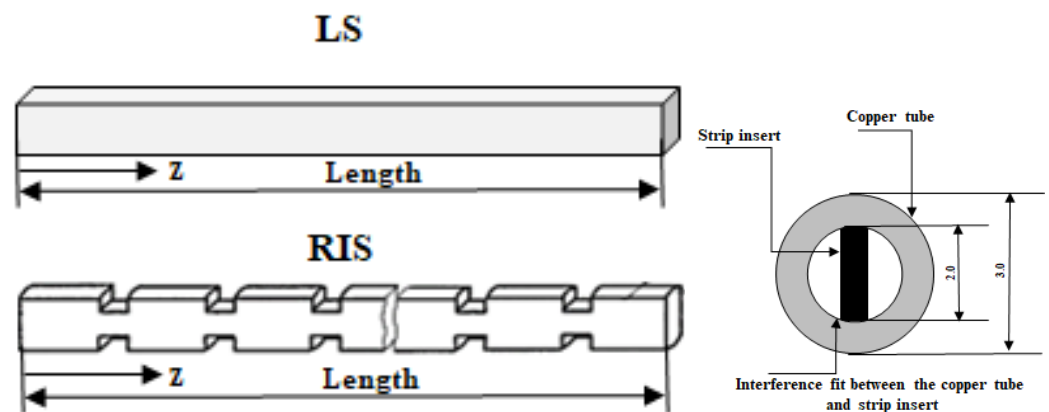
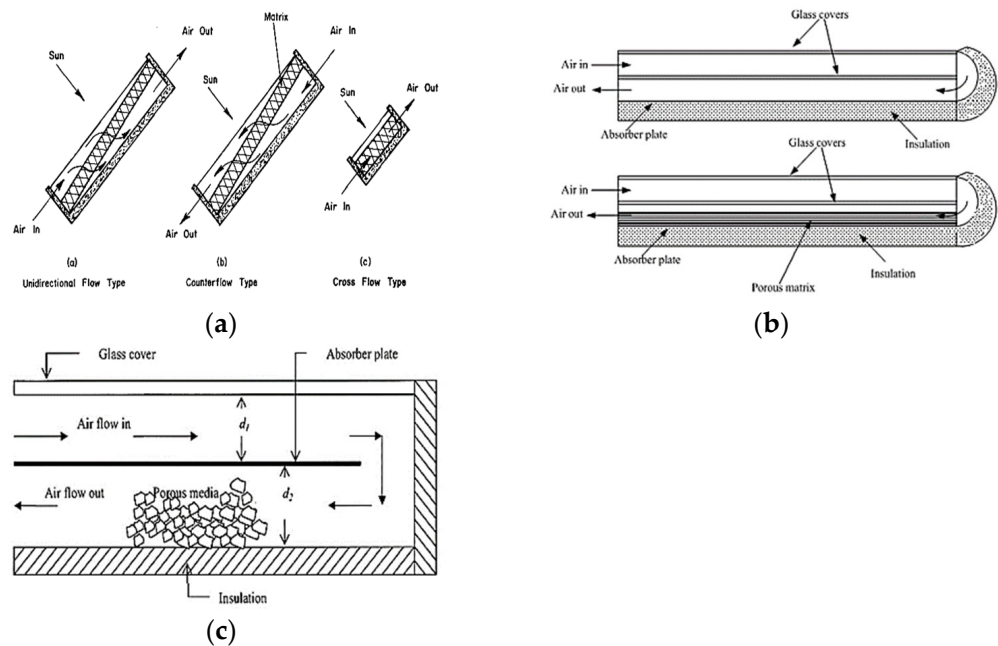


Figure 30. Geometry of the strip inserts; reprinted with the permission from ref. [131], 2022, Elsevier.

#### 8.5.6. Using Porous Absorber Matrix (Packed Duct)

The different flow arrangements using a porous absorber matrix may be categorized as unidirectional, counter, and cross flow, as shown in Figure 31a. For cross-flow configuration, the air flow and radiation direction are perpendicular to each other [137]. Several researchers have suggested using packing material to increase SAH performance [138–142]. The energy transferred from the packing material to the flowing air is more significant than the conventional collector. In the event of a packed duct, the fluid-flow path is always convoluted. As a result, heat transfer and equations that apply to fluid flowing in channels and ducts do not apply to clogged ducts, just as the criterion of laminar and turbulent fluid flow in circular tubes and ducts does not apply to packed duct flows.



**Figure 31.** Solar air collector with (a) matrix absorber, reprinted with permission [132], 2022, Elsevier (b); porous matrix, reprinted with permission [138], 2022, Elsevier; (c) DPSAH with packed bed material, reprinted with permission [61], 2022, Elsevier.

Ramani et al. [143] tested the thermo-hydraulic effectiveness of a DPSAH with and without porous media in an outdoor experiment. It has been claimed that the heat transfers of a DPSAH containing porous materials in the secondary channel is higher compared to SPSAH and DPSAH without porous materials. Figure 31b shows a schematic illustration of the investigated geometry. Sopian et al. [63,64,144] investigated the effects of variation in mass-flow rate and porous media on the performance of a DPSAH both theoretically and empirically. The geometry under investigation is depicted in Figure 31c.

Roy and Hoque [145] experimentally examined the heat transfer of a DPSAH with steel wire mesh as a porous medium. For a temperature differential of  $42.7\text{ }^{\circ}\text{C}$  and a flowrate of  $0.025\text{ kg/s}$ , the collector efficiency peaked at  $82.2\%$  for an insolation of  $1000\text{ W/m}^2$ . In a theoretical study, Verma and Varshney [146] evaluated the impact of various parameters on performing a wire-screen matrix packed-type SAH. The effective efficiency rose as flowrate improve, with the optimum value recorded for a flowrate of  $0.02$  to  $0.025\text{ kg/s}$ .

#### 8.5.7. Using Artificial Roughness

As mentioned before, poor thermal transmission from the face of an SAH duct is caused by forming a laminar sublayer close to the thermal-transfer surface's wall. This layer provides thermal resistance. This layer must be disrupted to improve heat transmission from the duct. Turbulence promoters or artificial roughness, such as repetitive ribs on a base plate, modify the laminar sublayer in the turbulence border area, creating turbulence in the fluid near the duct walls. One impact, such as a rise in the  $h$  value, is desirable, whereas the other, an increment in the pressure loss, is undesirable. As a result, the collector must be designed to achieve the goal of optimizing the heat-transfer coefficient while minimizing the pressure drop. To accomplish this objective, turbulence should be induced at the base plate surface, namely, in the laminar sublayer where heating is observed, without disturbing the core flow excessively to prevent pressure loss. This may be obtained by keeping the heights of the roughness components low relative to the height of the duct [147].

### 9. Artificial Roughness and Its Repercussions

Joule [148] suggested the concept of artificial roughness first. After that, different mathematical and empirical studies on the approaches of artificially roughened topologies

in the sectors of electronic devices, nuclear power stations, compact heat exchangers, and gas-turbine cooling, among others, were carried out [149,150]. The various roughness geometries have been examined; these can be broadly separated into regular and irregular roughened geometries. Depending on the scale, shape, and position of the roughness elements on the absorbent surface, a design of bumps, protrusions, and wire ribs may be utilized to create uniform or typical surface roughness [151–154]. The sandblasting procedure may generate uneven or intermittent surface-roughness patterns. To increase the heat-transmission rate of an SAH used for drying purposes, Prasad and Mullick [155] utilized circular cross-sectional wires to create a roughened shape and applied it for the first time on the absorbent surface. Ribs such as repeating wires, rib grooves, metal mesh, dimples, protrusions, and other rough surfaces were generated on the heated plate. The presence of a rib produces two flow-separation areas because of the production of secondary flow vortices on each side of the rib. Hence, ribs in the shape of repeating wires are often utilized. These flow vortices create turbulence in the flow field, which improves both thermal and hydraulic performance.

## 10. Investigations of Different Types of Artificial Roughness

Gee and Webb [156] investigated single-phase induced convective flow within a tubular with varied helix angles and rib roughness. Ghrilahre and Prasad investigated the THPP of roughened SAH using the ANN technique and found promising results with  $R^2$  values of 0.99532 and 0.9979. Garg and Prakash [54] depicted a traditional SAH system consisting primarily of rectangular wooden conduits with entrance, testing, and departure parts. The absorber surface absorbs solar radiation and transmits it through the convection to moving air via a glass or glazed cover. The thermal act of SAH was approximated using the Hottel–Whillier–Bliss equation published by Duffie–Beckman [148]. Creating roughness also encouraged undesirable flow resistance, which tends to cause blower-pump loss. Frank and Mark [157] provided a dimensionless parameter called the friction factor for analyzing the pressure decrease caused by the blower’s use of energy to move air through a channel. Webb and Eckert [158] described SAH’s overall behavior by combining heat discharge and frictional resistance using a well-known thermo-hydraulic performance parameter (THPP). A classification of different artificial rib roughness is shown in Figure 32.

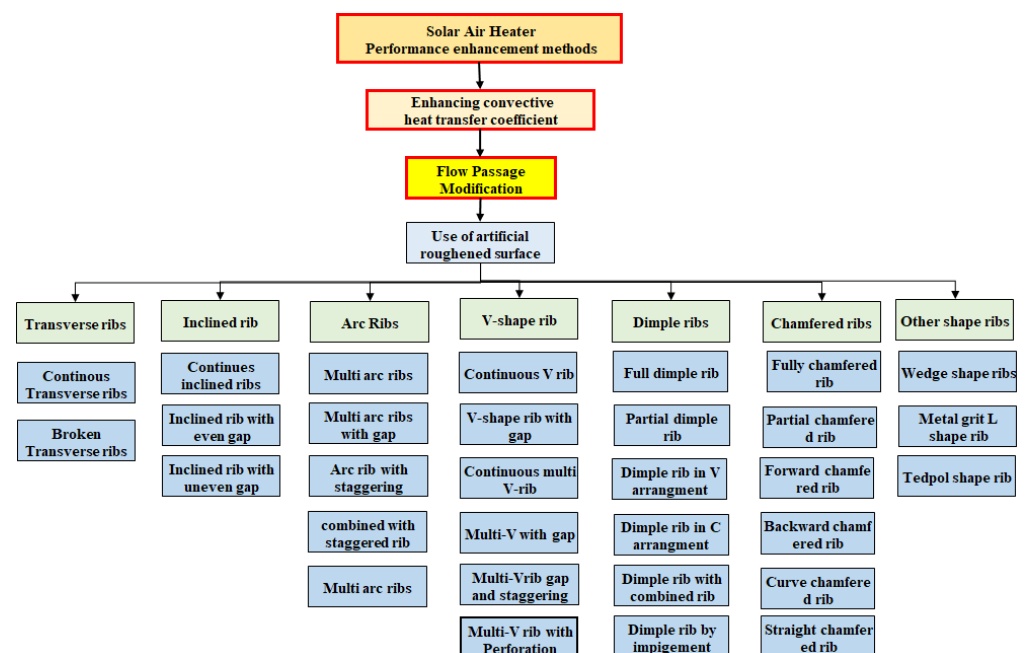


Figure 32. Classification of rib roughness on the basis of geometry.

Table 1 in the annexure summarizes major investigations on SPSAH and DPPFSAH conducted by various researchers. Table 2 also shows the range and values of various roughness and operational variables; a comparison between THPP and correlations of variation roughness are also given in the annexure.

**Table 1.** Optimum performance table of suggested rib configuration for SAH.

| S. No. | Researcher                | Proposed-Roughness Shape of Rib | $Nu/Nu_s$                      |           | $f f_s$      |            | THPP       |           |           |
|--------|---------------------------|---------------------------------|--------------------------------|-----------|--------------|------------|------------|-----------|-----------|
| 1      | Varun et al. [18]         | Multi-V (perforated) SPSAH      | 8.20                           |           | 6.20         |            | 5.15       |           |           |
| 2      | Varun et al. [60]         | Multi-V (perforated) DPPFSAH    | 9.70                           |           | 12.32        |            | 3.96       |           |           |
| 3      | Prasad-Saini [159]        | Transverse                      | 2.39                           |           | 4.26         |            | –          |           |           |
| 4      | Momin et al. [160]        | V(Continuous)                   | 2.31                           |           | 2.84         |            | 1.80       |           |           |
| 5      | Saini et al. [161]        | V(gap)                          | 3.61                           |           | 3.68         |            | –          |           |           |
| 6      | Saini et al. [162]        | Multi-V(gap)                    | 6.33–6.75                      |           | 6.13–6.36    |            | –          |           |           |
| 7      | Hans et al. [147]         | Multi-V(regular)                | 6.01                           |           | 5.01         |            | –          |           |           |
| 8      | Bhagoria et al. [163]     | V and W                         | 2.14–2.35                      |           | 2.18–2.01    |            | 1.28–1.97  |           |           |
| 9      | Patel and Lanjewar [164]  | Multi-V(staggering)             | 2.27                           |           | 3.41–2.02    |            | 1.58       |           |           |
| 10     | Karwa et al. [165]        | V down(discrete)                | St 65.0–90.0% and 102.0–142.0% |           | 2.65–3.55    |            | 1.52–1.79  |           |           |
| 11     | Singh [166]               | V down(gap)                     | 3.05                           |           | 3.12         |            | 1.71–2.04  |           |           |
| 12     | Chander et al. [98]       | Multi-V(gap—down)               | 3.35                           |           | 3.37–2.45    |            | 2.08–2.46  |           |           |
| 13     | Kumar et al. [167]        | V down(broken—staggered)        | 1.76–3.19                      |           | 2.10–2.83    |            | 1.36–2.20  |           |           |
| 14     | Han et al. [168]          | Angle rib                       | Discrete (angled)              | 1.72–3.96 | 1.73–3.98    | 6.35–9.25  | 6.50–8.10  | 1.20–1.85 | 1.42–1.76 |
| 15     |                           | V                               | V(discrete)                    | 2.46–4.19 | 2.32–4.62    | 7.91–14.50 | 7.20–8.30  | 1.25–1.86 | 1.46–1.93 |
| 16     |                           | W                               | W(discrete)                    | 3.02–4.59 | 2.57–4.83    | 9.20–14.50 | 7.20–13.10 | 1.46–1.85 | 1.45–1.86 |
| 17     | Kumar [169]               | Multi-V (dimple)                | –                              |           | –            |            | 2.23–3.26  |           |           |
| 18     | Promvongse et al. [170]   | Multi-V baffle(single BVG)      | 3.62–6.47                      |           | 10.02–78.60  |            | 1.43–1.84  |           |           |
| 19     |                           | Multi-V baffle(line array)      | 4.45–7.53                      |           | 12.50–129.60 |            | 1.14–1.68  |           |           |
| 20     |                           | Multi-V baffle (staggering)     | 4.13–7.14                      |           | 40.50–118.63 |            | 1.09–1.62  |           |           |
| 21     | Agrawal et al. [171]      | V down (gap)                    | 1.80–2.29                      |           | 1.18–1.65    |            | 1.54–2.05  |           |           |
| 22     | Kumar et al. [172]        | Vortex generator (winglet)      | 2.27                           |           | –            |            | –          |           |           |
| 23     | Maithani et al. [173]     | Transverse-blockage (perf.)     | 12.20–12.80                    |           | 13.80–14.80  |            | 2.34–2.63  |           |           |
|        |                           | Tilted blockage (perf.)         | 12.76–13.50                    |           | 13.26–14.15  |            | 2.59–2.72  |           |           |
|        |                           | V Blockage (cont.)              | 13.00–13.80                    |           | 13.00–13.80  |            | 2.81–2.86  |           |           |
|        |                           | V blockage (gap)                | 13.26–14.10                    |           | 12.75–13.50  |            | 2.96–3.11  |           |           |
|        |                           | V blockage (perf.)              | 13.86–14.86                    |           | 12.23–12.82  |            | 2.96–3.18  |           |           |
| 24     | Alam et al. [174]         | V baffles(holes)                | 6.76                           |           | 28.85        |            | 1.51       |           |           |
| 25     | Thakur et al. [175]       | V baffles(perf.)                | 1.50–3.00                      |           | –            |            | –          |           |           |
| 26     | Promthaisong et al. [176] | WVGs (rectangular)              | 7.10                           |           | 109.50       |            | 1.84       |           |           |
| 27     |                           | WVGs (trapezoidal)              | 6.79                           |           | 84.31        |            | 2.01       |           |           |
| 28     | Agrawal et al. [177]      | V baffles (perf.)               | 4.24                           |           | 14.73        |            | 2.24       |           |           |
| 29     | Thianpong et al. [178]    | $\Delta$ Winglet                | 2.30–2.60                      |           | 4.70–10.10   |            | 1.03–1.38  |           |           |
| 30     | Promvongse et al. [179]   | Wavy-groove( $\Delta$ -WVG)     | 3.77–6.18                      |           | 47.88–34.25  |            | 1.68–2.25  |           |           |
| 31     | Maheshwari et al. [180]   | Baffle (hole)                   | 1.78–2.68                      |           | 2.99–8.01    |            | –          |           |           |
|        |                           | Baffle (partial hole)           | 2.34–3.75                      |           | 4.41–17.50   |            | –          |           |           |

**Table 2.** Overview of the different options used by researchers to improve the THP of SPSAH and DPPFSAH.

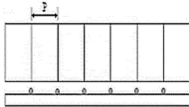
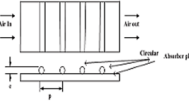
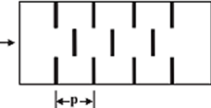
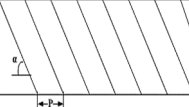
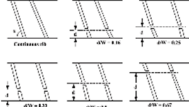
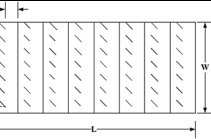
| Researcher              | Rib Geometry                      | Correlation  | Rib Geometry  | Roughness Parameters  | Outcomes (Nu and f)  |
|-------------------------|-----------------------------------|--|---|---|--|
| Prasad and Saini [159]  | Transverse wire ribs              | $\overline{St} = \frac{f}{1 + \sqrt{\frac{f}{2} \left\{ 4.5(e+)^{0.28} Pr^{0.57} - 0.95 \left(\frac{P}{e}\right)^{0.53} \right\}}}$ $f = 2 / \left[ 0.95 \left(\frac{P}{e}\right)^{0.53} + 2.5 \ln \left(\frac{D}{2e}\right) - 3.75 \right]^2$   |    | $e/D_h = 0.014/0.032,$<br>$P/e = 10.0/20.0, e_{opt} = 24,$<br>$Re = 5000/20,000$                                      | Nu and f improvements of 2.38 and 4.25 times, respectively, were recorded across the smooth plate.                             |
| Prasad and Verma [181]  | Small-diameter transverse wire    | $Nu = 0.08596 \left(\frac{P}{e}\right)^{-0.54} \left(\frac{e}{D_h}\right)^{0.0726} Re^{0.723} \quad (e \leq 24)$ $Nu = 0.0245 \left(\frac{P}{e}\right)^{-0.016} \left(\frac{e}{D}\right)^{0.021} Re^{0.802} \quad (e \geq 24)$ $f = 0.0245 \left(\frac{P}{e}\right)^{-0.0206} \left(\frac{e}{D_h}\right)^{0.021} Re^{-1.25}$   |    | $e/D_h = 0.014/0.03,$<br>$P/e = 10/40,$<br>$e+_{opt} = 8/42, Re = 5000-20,000$  | The ideal thermo-hydraulic efficiency referring to $e+_{opt} = 24$ was observed to be around 71%.                              |
| Sahu and Bhagoria [182] | 90° broken transverse ribs        | —  |    | $e/D_h = 0.0338$<br>$e = 1.5 \text{ mm}$<br>$d = 44.44 \text{ mm}$<br>$P = 10,20,30$<br>$W/H = 8.0, Re = 3000/12,000$ | A 1.25- to 1.4-times increase in the thermohydraulic performance over smooth plate was recorded.                               |
| Gupta et al. [183]      | Traverse rib                      | $Nu = 0.000824 \left(\frac{e}{D}\right)^{-0.178} \left(\frac{W}{H}\right)^{0.284} Re^{1.062} \quad (e \leq 35)$ $Nu = 0.000307 \left(\frac{e}{D}\right)^{-0.019} \left(\frac{W}{H}\right)^{0.237} Re^{-0.185} \quad (e \geq 35)$ $f = 0.06412 \left(\frac{e}{D_h}\right)^{0.019} \left(\frac{W}{H}\right)^{0.237} Re^{-0.185}$ |    | $e/D_h = 0.02/0.033$<br>$P/e = 10$<br>$Re = 4000/18,000$<br>$\alpha = 61.90^\circ$                                    | For solar insolation of 1000 W/m <sup>2</sup> , the highest increase of about 5.7 over smooth plate was obtained at Re = 8000. |
| Aharwal et al. [184]    | Inclined continuous with gap ribs | $Nu = 0.0102 \left(\frac{e}{D}\right)^{60.51} Re^{1.148} \left[ \left\{ 1 - \left(0.25 - \frac{d}{w}\right)^2 \left\{ 0.01 \left(1 - \frac{g}{e}\right)^2 \right\} \right\} \right]$ $f = 0.5 \left(\frac{e}{D}\right)^{0.72} Re^{-0.0836}$  |   | $e/D_h = 0.0377$<br>$Re = 3000/21,000$<br>$P/e = 10, \alpha = 60^\circ$<br>$W/H = 5.84; g/e = 1; d/W = 0.25$          | In Nu and f, improvements of 2.8 and 3.6 times, respectively, were recorded.   |
| Varun et al. [185]      | Inclined/transverse combination   | $Nu = 0.00060 \left(\frac{P}{e}\right)^{0.0104} Re^{1.213}$ $f = 1.0858 \left(\frac{P}{e}\right)^{0.0114} Re^{-0.3685}$  |  | $e/D_h = 0.030$<br>$Re = 3000/18,000$<br>$P/e = 10, \alpha = 60^\circ, W/H = 5.84;$<br>$g/e = 1; d/w = 0.25$          | The optimum result obtained for (p/e) = 8 for roughened absorber plate.  |

Table 2. Cont.

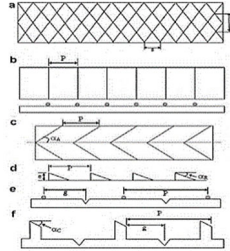
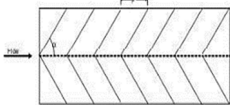
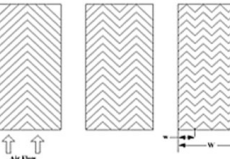
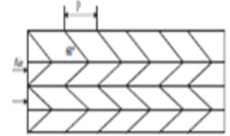
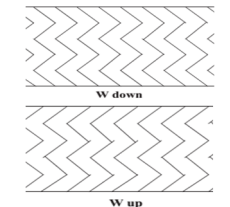
| Researcher            | Rib Geometry  | Correlation   | Rib Geometry  | Roughness Parameters   | Outcomes (Nu and f)   |
|-----------------------|---|---|---|--|---|
| Gupta et al. [186]    | Six: smooth rib, (mess), V-shaped; wedge; expanded mesh; grooved rib-type and chamfered grooved rib | $Nu = 0.00824 \left(\frac{e}{D_h}\right)^{-0.178} \left(\frac{W}{H}\right)^{0.284} Re^{1.062} \exp\left[-0.04\left(1 - \frac{\alpha}{60}\right)^2\right] \left(\frac{k}{D}\right) e \leq 35$ $Nu = 0.00307 \left(\frac{e}{D_h}\right)^{-0.469} \left(\frac{W}{H}\right)^{0.245} Re^{8.812} \exp\left[-0.0475\left(1 - \frac{\alpha}{60}\right)^2\right] \left(\frac{k}{D}\right) e \geq 35$ $f = 0.06412 \left(\frac{e}{D_h}\right)^{0.019} \left(\frac{W}{H}\right)^{0.0237} Re^{-0.185} \exp\left[-0.0993\left(1 - \frac{\alpha}{60}\right)^2\right]$ |    | $Re = 500/50,000,$<br>$P/e = 10/40$<br>$e/D_h = 0.02/0.053$  | At high Re, circular- and V-shaped ribs achieved high THP.  |
| Momin et al. [160]    | V-shaped continuous wire rib  | $Nu = 0.08596 \left(\frac{P}{e}\right)^{-0.54} \left(\frac{e}{D}\right)^{0.072} Re^{0.723} (e \leq 24)$ $Nu = 0.245 \left(\frac{P}{e}\right)^{-0.016} \left(\frac{e}{D}\right)^{0.021} Re^{0.802} (e \geq 24)$ $f = 6.266 \left(\frac{e}{D}\right)^{0.565} \left(\frac{\alpha}{60}\right)^{-0.093} Re^{-0.425} \exp\left[-0.719 \ln\left(\frac{\alpha}{60}\right)^2\right]$   |    | $e/D = 0.02/0.035$<br>$P/e = 10,$<br>$Re = 2000/15,500$<br>$\alpha = 60^\circ$                           | A 2.3- and 2.83-times improvement in Nu and f, respectively, was recorded.  |
| Hans et al. [147]     | Multiple V-shaped rib   | $Nu = 3.35 \times \left[10\right]^{-5} Re^{0.92} (e/D)^{0.77} (W/w)^{0.43} (\alpha/90)^{-0.49} \exp\left[-0.1177 \{L_n (W/w)\}^2\right] \exp\left[-0.611 (L_n (\alpha/90))^2\right]$ $f = 4.47 \times \left[10\right]^{-4} Re^{-0.3188} \left[ (e/D)^{0.732} (W/w)^{0.22} (\alpha/90)^{-0.39} \exp\left[-0.522 (L_n (\alpha/90))^2\right] (P/e)^{8.9} \exp\left[-2.1330 (L_n (P/e))^2\right] \right]$   |    | $e/D_h = 0.03$<br>$Re = 2000/20,000$<br>$P/e = 6/12$<br>$\alpha = 60^\circ$<br>$W/H = 5.87$              | A 6.0- and 5.0-times improvement in Nu and f was recorded above smooth SAH, respectively.   |
| Lanjewar et al. [163] | V- and W-shaped ribs  | $Nu = 0.0613 (Re)^{0.9079} \left(\frac{e}{D_h}\right)^{0.4487} \left(\frac{\alpha}{60}\right)^{-0.1331} \exp\left[-0.5307 \left\{\ln\left(\frac{\alpha}{60}\right)\right\}^2\right]$ $f = 0.61282 (Re)^{-0.2254} \left(\frac{e}{D_h}\right)^{0.4622} \left(\frac{\alpha}{60}\right)^{0.0817} \exp\left[-0.28 \left\{\ln\left(\frac{\alpha}{60}\right)\right\}^2\right]$   |   | $s/e = 15.62/46.87$<br>$e/D_h = 0.012/0.0390$<br>$Re = 2300/14,000$<br>$P/e = 10$                        | In Nu and f, 2.36- and 2.01-times improvements were recorded over smooth SAH, respectively.   |
| Lanjewar et al. [187] | W shape with upward and downward orientations   | $R = \sqrt{\frac{f}{\tau}} + 2.5 \ln\left(\frac{2e}{D_h}\right) + 3.75$ $e^+ = \sqrt{\frac{f}{\tau}} Re \left(\frac{e}{D_h}\right)$ $g = \left[\left(\frac{f}{25\tau}\right) - 1\right] \sqrt{\frac{f}{\tau}} + R$  |  | $e/D_h = 0.018/0.03375$<br>$W/H = 8$<br>$P/e = 10$<br>$Re = 2300/14,000$<br>$\alpha = 30^\circ/75^\circ$ | A 2.36- and 2.01-times improvement over smooth SAH in Nu and f were recorded. The downward W ribs with a streamattack angle of $60^\circ$ provide the best thermo-hydraulic efficiency. |

Table 2. Cont.

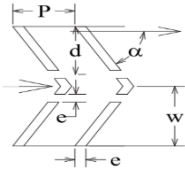
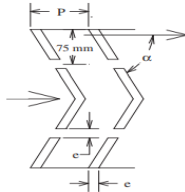
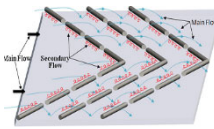
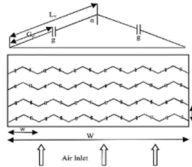
| Researcher            | Rib Geometry            | Correlation  | Rib Geometry  | Roughness Parameters  | Outcomes (Nu and f)  |
|-----------------------|-------------------------|--|---|---|--|
| Singh et al. [188]    | Discrete V-down ribs    | $Nu = 2.360 \times [10]^{-5} Re^{0.90} (P/e)^{3.5} (\alpha/60)^{-0.023} (g/e)^{-0.014} (d/w)^{-0.043} (e/D_h)^{0.47}$ $\exp[-0.084\{\ln(p/e)\}^2] \exp[-0.720\{\ln(\alpha/60)\}^2]$ $\exp[-0.050\{\ln(d/w)\}^2] \exp[-0.150\{\ln(g/e)\}^2]$ $f = 44.130 \times [10]^{-2} Re^{-0.126} (P/e)^{-0.034} (\alpha/60) (d/w)^{-0.058}$ $(g/e)^{-0.0310} (e/D_h)^{0.700} \exp[-0.685\{\ln(p/e)\}^2]$ $\exp[-0.930\{\ln(\alpha/60)\}^2] \exp[-0.058\{\ln(d/w)\}^2]$ $\exp[-0.210\{\ln(g/e)\}^2]$  |    | $e/D_h = 0.043$<br>$e = 0.8/1.5 \text{ mm}$ ,<br>$P/e = 10$<br>$Re = 3000/15,000$<br>$d/w = 0.2/0.8$ (Five value) 0.65;<br>$g/e = 1$<br>$\alpha = 60^\circ$ | In Nu and f, 3.04 and 3.11 times improvement were recorded over smooth duct, respectively.   |
| Singh et al. [166]    | V-down ribs with a gap  | —  |    | $e/D_h = 0.043$<br>$\alpha = 60^\circ$<br>$P/e = 8Re = 3000/15,000$<br>$W/H = 12$   | Nu = 3.04 and f = 3.11 were recorded. The highest THPP = 2.06 at $\alpha = 60^\circ$ .   |
| Maithani et al. [189] | V ribs (continuous/gap) | $Nu = 1.8 \times [10]^{-6} Re^{0.9636} [N_g]^{0.1260} (g/e)^{0.112} (p/e)^{5.74190} (\alpha/60)^{0.1307}$ $\exp[-0.0551\{\ln(N_g)\}^2] \exp[-0.04013\{\ln(g/e)\}^2]$ $\exp[-1.2990\{\ln(P/e)\}^2] \exp[-0.895\{\ln(\alpha/60)\}^2]$ $f = 3.60 \times [10]^{-7} Re^{-0.1512} Ng^{0.1484}$ $(g/e)^{0.072} (P/e)^{9.24} (\alpha/60)^{0.070} \exp[-0.0764\{\ln(N_g)\}^2]$ $\exp[-0.0249\{\ln(g/e)\}^2] \exp[-2.080\{\ln(P/e)\}^2]$ $\exp[-0.33364\{\ln(\alpha/60)\}^2]$  |    | $e/D_h = 0.022/0.043$<br>$g/e = 1/5$<br>$P/e = 6/12$<br>$W/w = 1/10$<br>$\alpha = 30/75^\circ$<br>$Re = 4000/18,000$  | The overall increase in the magnitude of 3.6 times that of the smooth SAH was achieved by Nu; likewise, the f also increased by 3.67 times the smooth SAH. |
| Kumar et al. [162]    | Multi-V rib (gap)       | $Nu = 8.5340 \times [10]^{-3} Re^{0.9320} (e/D)^{0.1750} (W/w)^{0.506}$ $\exp[-0.7530\{\ln(W/w)\}^2] (G_d/L_v)^{-0.0348}$ $\exp[-0.0653\{\ln(G_d/L_v)\}^2] (g/e)^{-0.0708}$ $\exp[-0.2231\{\ln(g/e)\}^2] (\alpha/60)^{-0.0239}$ $\exp[0.12530\{\ln(\alpha/60)\}^2] (P/e)^{1.1960} \exp[0.2805\{\ln(P/e)\}^2]$ $f = 3.1934Re^{-0.391} (e/D)^{0.2680} (W/w)^{0.1133}$ $\exp[-0.9740\{\ln(W/w)\}^2] (G_d/L_v)^{0.0610}$ $\exp[-1.0650\{\ln(G_d/L_v)\}^2] (g/e)^{-0.1769}$ $\exp[-0.6349\{\ln(g/e)\}^2] (\alpha/60)^{0.1554}$ $\exp[0.1527\{\ln(\alpha/60)\}^2] (P/e)^{-0.7941}$ $\exp[0.14860\{\ln(P/e)\}^2]$ |  | $e/D_h = 0.043, g/e = 0.5/1.5$ ,<br>$P/e = 10$<br>$G_d/L_v = 0.24/0.80$<br>$Re = 2000/20,000$   | Nu = 6.32 and f = 6.12 were the recorded times.  |

Table 2. Cont.

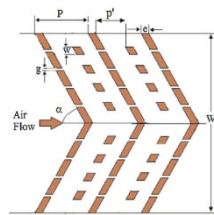
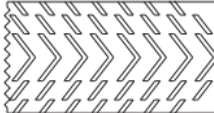
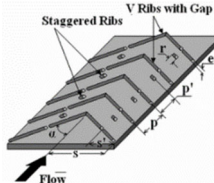
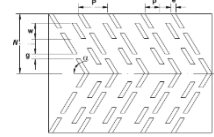
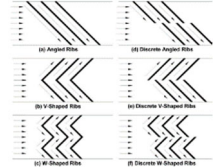
| Researcher            | Rib Geometry                                   | Correlation  | Rib Geometry  | Roughness Parameters  | Outcomes (Nu and f)   |
|-----------------------|--|--|---|---|---|
| Lanjewar et al. [164] | Multi-V rib(staggering)                        | $Nu = 2.36x \left[ \left[ \frac{10}{3} Re^{0.9} (p/e)^{3.5} (\beta/60)^{-0.023} (Re/e)^{-0.0140} \right] \times \exp \left[ \left[ -0.84 (\ln(p/e))^2 \right] \right] \exp \left[ \left[ -0.72 (\ln \left[ \left( \frac{\beta}{60} \right)^2 \right] (e/D) \right) \right] \right] \exp \left[ \left[ -0.05 (\ln(d/wh))^2 \right] \right] \exp \left[ \left[ -0.150 (\ln(Re/e))^2 \right] \right] (d/wh)^{-0.043} \right] \right] \left[ \right]$ $f = 4.13 * \left[ \left[ \frac{10}{3} \right] \right]^{-2} Re^{-0.126} (p/e)^{2.74} (\beta/60)^{-0.034} (Re/e)^{0.031} * \exp \left[ \left[ -0.685 (\ln \left[ \left( \frac{p}{e} \right)^2 \right] \right] \right] \exp \left[ \left[ -0.930 \left( \left[ \ln \left( \frac{\beta}{60} \right) \right]^2 \right) \right] \right] (e/D)^{0.70} * \exp \left[ \left[ -0.058 (\ln(d/wh))^2 \right] \right] \exp \left[ \left[ -0.21 (\ln(Re/e))^2 \right] \right] (d/wh)^{-0.058} \right] \right] \left[ \right]$ |    | <p>P/e = 12<br/>                     e/Dh = 0.045<br/>                     alpha = 60°<br/>                     Ng = 4<br/>                     w/e = 2, 3.5, 4.5, 5.5<br/>                     p0/P = 0.65<br/>                     Re = 3000/12,000</p> | There was a significant increase in Nu = 2.27 and f = 3.40, whereas THPP reached 1.59.  |
| Karwa et al. [165]    | Discrete V-down rib                            | —  |    | <p>e/Dh = 0.0470<br/>                     p/e = 10.0<br/>                     Re = 2800/15,000 alpha = 60°</p>  | A significant increase in Nu = 2.27 and f = 4.28.   |
| Patil et al. [167]    | V-down rib(broken-staggered)                   | $Nu = 0.0089 Re^{0.97} \exp \left[ \frac{0.12}{1 + \{20.42 \ln(\frac{e}{s}) + 1.19\}^2} + \frac{0.11}{1 + \{20.3 \ln(\frac{p'}{p}) + 1.41\}^2} + 0.004 \left[ \ln \left( \frac{r}{e} \right) \right]^{0.71} \right]$ $f = 0.09 Re^{-0.18} \exp \left[ \frac{0.10}{1 + \{30.18 \ln(\frac{e}{s}) + 1.56\}^2} + \frac{0.08}{1 + \{20.6 \ln(\frac{p'}{p}) + 1.40\}^2} + 0.017 \left\{ \ln \left( \frac{r}{e} \right) \right\}^{2.5} \right]$   |    | <p>P/e = 10.0<br/>                     alpha = 60°<br/>                     Re = 3000–17,000<br/>                     e/Dh = 0.0430<br/>                     W/H = 12</p>   | Nu = 3.18 and f = 2.82 at (s0/s) = 0.6, (p0/p) = 0.6 and (r/e) = 2.5.   |
| Deo et al. [98]       | V-down ribs with multi-gap staggering          | $Nu = 0.02253 Re^{0.8} \left( \frac{p}{e} \right)^{-0.06} \left( \frac{e}{D} \right)^{0.18} \left( \frac{\beta}{60} \right)^{0.04}$ $f = 0.3715 Re^{-0.15} \left( \frac{p}{e} \right)^{0.21} \left( \frac{e}{D} \right)^{0.65} \left( \frac{\beta}{60} \right)^{0.57}$   |  | <p>P/e = 4.0–14.0<br/>                     (8 levels), e/Dh = 0.0260/0.0570<br/>                     (4 levels), alpha = 40/80°, w/e = 4.5,<br/>                     Re = 4000/12,000</p>   | Nu = 3.34, f = 2.45 THPP = 3.38.  |
| Wright et al. [168]   | Continuous and discrete, V and W ribs (angled) | $f = (p_i - p_e) / (4 \left( \frac{L}{Dh} \right) \left( \frac{1}{2\rho V^2} \right))$   |  | <p>e/Dh = 0.078<br/>                     p/e = 10.0<br/>                     alpha = 45°<br/>                     Re = 10,000/40,000,<br/>                     Ro = 0.0/0.15 Delta rho / rho = 0.120</p>  | THPP = 1.41–1.96. Across both revolving and non-revolving ducts, the distinct V-shaped geometry and distinct W-shaped roughness had the highest thermal efficiency. |

Table 2. Cont.

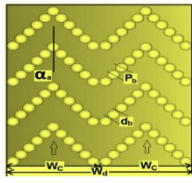
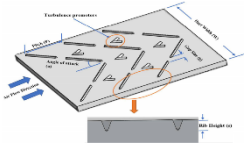
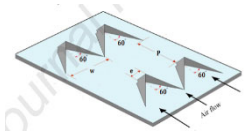
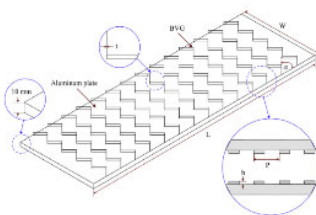
| Researcher         | Rib Geometry                                 | Correlation   | Rib Geometry  | Roughness Parameters   | Outcomes (Nu and f)  |
|--------------------|--|---|---|--|--|
| Kumar et al. [169] | Multiple V-type pattern with dimpleobstacles | $Nu = 9.351 \times [10]^{-14} Re^{1.066} (W_c/W_d)^{2.9852} \exp[0.91 \{ \ln(W_c/W_d) \}^2] (p_b/e_d)^{2.99} \{ \exp[\ln\{p_b/e_d\}] \}^2 (e_d/d_d)^{-0.2481} \exp\{-0.1910 \{ \ln(e_d/d_d) \}^2\} (\alpha/55)^{-1.097} \exp[-2.5629 \{ \ln(\alpha/55) \}^2]$ $f = 2.05 \times [10]^{-5} Re^{-0.6307} (W_c/W_d)^{0.0854} \exp[0.0676 \{ \ln(W_c/W_d) \}^2] (p_b/e_d)^{19.131} \{ \exp[\ln\{p_b/e_d\}] \}^2 (e_d/d_d)^{-0.1621} \exp\{-0.341 \{ \ln(e_d/d_d) \}^2\} (\alpha/55)^{-0.22541} \exp[-2.3031 \{ \ln(\alpha/55) \}^2]$ |    | $e/Dh = 0.50/2.0,$<br>$P/e = 8/11,$<br>$e/d = 0.037,$<br>$\alpha = 35^\circ/75^\circ,$<br>$W/w = 5,$<br>$Re = 5000/17,000$     | Custom multi-V configuration dimpled roughness had approximately 7.0% higher THPP than some other roughness structure.   |
| Misra et al. [171] | V-down rib (multiple gaps)                   | —   |    | $P/e = 8-14$<br>$\alpha = 45^\circ \text{ to } 60^\circ$<br>$\beta = 23\%$<br>$Re = 4000-20,000$                               | At $P/e = 10$ and $\alpha = 45^\circ$ $Nu = 2.26$ (optimum)  |
| Kumar et al. [172] | Vortex generator with winglet type           | $Nu = 3.641 * [10]^{-5} Re^{0.951} (\alpha/75)^{-0.91} (Pi/e)^{3.731} (W/w)^{2.37} * \exp[-1.22 (\ln [\alpha/75]^2) * \exp[-0.90 (\ln [Pi/e])^2] * \exp[-0.81 (\ln W/w)^2]]$ $f = 0.131 Re^{-0.37} (\frac{\alpha}{75})^{-0.12} (\frac{W}{w})^{2.411} \exp[-0.77 (\ln W/w)^2]$   |    | $P/e = 5 \text{ to } 12,$<br>$\alpha = 30^\circ \text{ to } 75^\circ, W/w = 3 \text{ to } 7$<br>$Re = 3000 \text{ to } 22,000$ | The number of Nu hit its maximum at $W/w = 5$ , whereas the f calculated at $W/w = 3$ at $\alpha = 60^\circ$ was maximal for the structural properties specified.  |
| Tamna et al. [170] | Multi-V baffles vortex generator (BVG)       | <p>for single BVG</p> $Nu = 0.281 Re^{0.761} Pr^{0.41} (PR + 1.0)^{0.6581}$ $f = 0.28 Re^{0.066} (PR + 1.0)^{-2.07}$ $TEF = 5.108 Re^{0.116} (PR + 1.0)^{0.107}$ <p>in-line BVG:</p> $Nu = 0.343 Re^{0.753} Pr^{0.41} (PR + 1.0)^{0.621}$ $f = 8.9 Re^{0.06} (PR + 1.0)^{0.85}$ $TEF = 5.505 Re^{0.126} (PR + 1.0)^{0.338}$ <p>for staggered BVG1</p> $Nu = 0.3112 Re^{0.756} Pr^{0.41} (PR + 1.0)^{0.6191}$ $f = 10.491 Re^{0.077} (PR + 1.0)^{0.9821}$ $TEF = 4.961 Re^{0.122} (PR + 1.0)^{0.296}$                            |  | $Re = 8000,$<br>$P/H = 0.50/2.0$<br>$b/H = 0.250$  | <p>BVG (single) <math>Nu/Nu_s = 3.98-6.95</math><br/> <math>f/f_s = 12.75-79.20</math><br/> <math>TEF = 1.45-1.85</math></p> <p>In-line array <math>Nu/Nu_s = 4.45-7.53</math><br/> <math>f/f_s = 52.5-129.6</math><br/> <math>TEF = 1.13-1.67</math></p> <p>For staggered <math>BVG Nu/Nu_s = 4.12-7.13</math><br/> <math>f/f_s = 40.5-118.6</math><br/> <math>TEF = 1.08-1.62</math></p> |

Table 2. Cont.

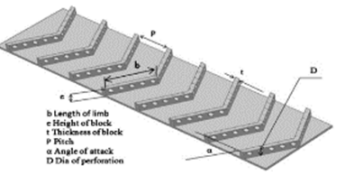
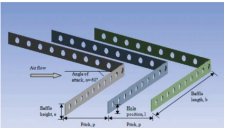
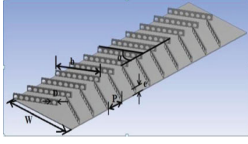
| Researcher               | Rib Geometry                               | Correlation  | Rib Geometry  | Roughness Parameters  | Outcomes (Nu and f)   |
|--------------------------|--|--|---|---|---|
| Kumar et al. [173]       | Perforated transverse blockage             | _____  |    | $\alpha = 60^\circ$<br>$H_B/B_D = 0.50, P_B/B_B = 10,$<br>$\beta_O = 12.00\%$<br>$G_L/D_V = 0.65$<br>$Re = 3000-18,000$                             | $Nu/Nu_s = 12.2-12.8$<br>$f/f_s = 13.8-14.8$<br>$(THPP)_{max} = 2.35-2.62$  |
|                          | Perforated blockage at an angle            |  |    |   | $Nu/Nu_s = 12.75-13.50$<br>$f/f_s = 13.25-14.15$<br>$(THPP)_{max} = 2.58-2.72$  |
|                          | Continuous V-blockage                      |  |    |   | $Nu/Nu_s = 13.0-13.8$<br>$f/f_s = 13.0-13.8$<br>$(THPP)_{max} = 2.81-2.86$  |
|                          | V-blockage with gap                        |  |    |   | $Nu/Nu_s = 13.25-14.1$<br>$f/f_s = 12.75-13.50$<br>$(THPP)_{max} = 2.95-3.11$   |
|                          | Perforated V-blockage                      |  |    |   | $Nu/Nu_s = 13.85-14.85$<br>$f/f_s = 12.22-12.81$<br>$(THPP)_{max} = 2.95-3.19$  |
| Alam et al. [174]        | Baffles V-shaped roughness (hole)          | $Nu = 0.0135 * Re^{0.815} \left[ \left( \frac{e}{H} \right)^{\gamma(-0.12150)} \left( \frac{P}{e} \right)^{1.83680} \beta^{(-0.23450)} \left( \frac{\alpha}{60} \right)^{\gamma(-0.02330)} \left( \varphi \right)^{\gamma(-0.63790)} * \exp[-0.91050 \{ \ln \left[ \left( \frac{e}{H} \right) \right]^2 \} \exp[-0.455 \{ \ln(P/e) \} 2.0] * \exp\{-0.071 \{ \ln(\beta) \} 2.0\} * \exp[-0.2761 \{ \ln(\alpha/60) \} 2.0] * \exp[-0.968 \{ \ln(\varphi) \} 2.0]} \right]$ $f = 0.4613 Re^{0.815} (-0.942) \left( \frac{e}{H} \right)^{1.3377} \left( \frac{P}{e} \right)^{\gamma(-0.195)} \left( \frac{\alpha}{60} \right)^{0.0017} \left( \varphi \right) - 0.43360 * \exp[-0.7097 \{ \ln(e/H) \}^2] \exp[-0.29730 \{ \ln(\alpha/60) \}^2] \left[ \exp \left[ \left[ -0.6106 \{ (\varphi) \}^2 \right] \right] \right]$ |    | $\alpha = 30^\circ, 45^\circ, 60^\circ$ and $75^\circ$<br>$P/e = 4-12$<br>$\beta = 0.05-0.25$<br>$e/H = 0.4-1.0$<br>$Re = 2000-20,000$              | When tubular perforation holes were substituted by rectangle types holes with a circularity = 0.69, the enhancement of the Nusselt number (Nu) = 1.13 ratio was observed. |
| Chamoli and Thakur [175] | Perforated V-baffles                       | $Nu = 0.0296 Re^{0.7848} \left( \frac{p}{e} \right)^{0.3007} \left( \frac{H}{e} \right)^{\gamma(-0.6774)} \left( \beta \right)^{\gamma(-0.3571)} \exp(-0.2548 \left[ \ln(P/e) \right]^2) \times \exp(-0.4406 \left[ \ln(H/e) \right]^2) \exp(-0.0863 \left[ \ln(\beta) \right]^2)$ $f = 0.632 Re^{(-0.18)} \left( \frac{P}{e} \right)^{\gamma(-0.16)} \left( \frac{H}{e} \right)^{1.05} \left( \beta \right)^{\gamma(-0.13)}$  |  | $e/H = 0.285/0.6$ (4 values), $P/e = 1/4$ (7 values), $\alpha = 60^\circ$ , $AR = 10$ , $\beta = 12/44\%$ (4 values), $Re = 3800-19,000$ (6 values) | Maximum Nusselt number ranged from 1.5 to 3.  |
| Jain et al. [177]        | Baffles with discrete V-shaped perforation | _____  |  | $P/e = 6$<br>$e/H = 0.3/0.5$ (4 levels), $\beta = 23\%$<br>$\alpha = 60^\circ$<br>$Re = 4000/18,000$  | $Nu = 4.24$ and $f = 14.73$ and optimum THPP = 2.24 at $e/H = 0.4$ .  |

Table 2. Cont.

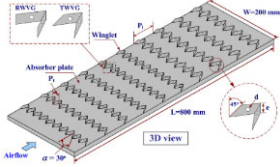
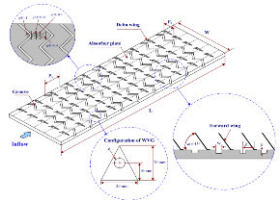
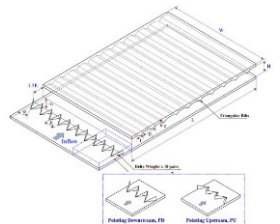
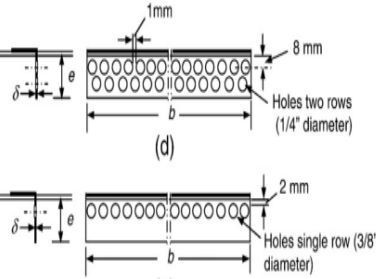
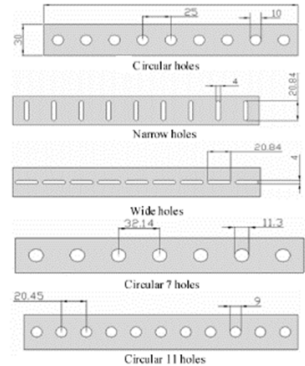
| Researcher              | Rib Geometry  | Correlation   | Rib Geometry  | Roughness Parameters   | Outcomes (Nu and f)   |
|-------------------------|---|---|---|--|---|
| Skullung et al. [176]   | Perforated-winglet with vortex generator (WVGs)(rectangular +trapezoidal) | $Nu = 0.347Re^{0.729} Pr^{0.4} (B_R)^{0.215} (P_R)^{-0.203}$ $f = 8.334 Re^{-0.056} (B_R)^{0.682} (P_R)^{-0.525}$ $Nu = 0.279 Re^{0.736} Pr^{0.4} (B_R)^{0.13} (P_R)^{-0.104}$ $f = 5.102 Re^{-0.062} (B_R)^{0.471} (P_R)^{-0.247}$   |    | $Re = 4100/25,500, \alpha = 30^\circ$<br>$BR = e/H = 0.2/0.4, PR = Pl/H = 1/2$                                 | $Nu = 7.1$ and $f = 109.5$ at $BR = 0.48$ and $THPP = 1.84$ at $PR = 1$ at rectangle WVGs, whereas trapezoidal WVG for $BR = 0.2$ and $PR = 1.5$ produced $Nu = 6.78$ and $f = 84.32$ with $THPP = 2.01$ .  |
| Skullung et. al. [179]  | Wavy groove (delta -WVG)  | <p>For Forward-WVG</p> $Nu = 0.0763Re^{0.7758} Pr^{0.4} \alpha^{0.1878}$ $f = 0.1059Re^{-0.0397} \alpha^{0.6062}$ <p>For Backward-WVG</p> $Nu = 0.0576 Re^{0.7747} Pr^{0.4} \alpha^{0.2487}$ $f = 0.4467 Re^{-0.257} \alpha^{0.4535}$ |    | $W/H = 10, P/H = 1$<br>$Ah/Aw = 0.0310/0.1670, g/H = 0.4/1.0, \alpha = 45^\circ$<br>$Re = 4800/23,000$         | $Nu = 3.77-6.18$ and $f = 47.88-34.25$ and optimum $TEF = 1.69-2.24$ .  |
| Promvongse et al. [178] | Delta-winglet blockages   | _____   |   | $AR = 10.0, \alpha = 30^\circ / 60^\circ, e/H = 0.20, P_1/H = 1.330, b/H = 0.40, Pt/H = 1.0, Re = 5000/22,000$ | $Nu = 2.3-2.6$ and $f = 4.7-10.1$ , whereas $TEF = 1.02-1.39$ .   |
| Karwa et al. [180]      | Baffles with full and half perforation                                    | _____   |  | $p/e = 7.2-28.8$<br>$\beta = 26-46.8\%$<br>$W/H = 7.77$<br>$e/H 0.495$<br>$Re = 2700-11,150$                   | A 79 to 169% improvement in $Nu$ as compared to smooth plate for the completely perforated baffles and 133.0% to 274.0% for the partial baffle perforation, whereas the $f$ for the completely perforated baffles was 2.95–8.02 times that for the smooth plate and 4.42–17.5 times that for the half-perforated baffles. |

Table 2. Cont.

| Researcher          | Rib Geometry                | Correlation  | Rib Geometry  | Roughness Parameters   | Outcomes (Nu and f)  |
|---------------------|-----------------------------|--|---|--|--|
| Shin and Kwak [190] | Wall of perforated blockage | $Nu = \frac{\left[\left(\frac{f}{8}\right)(Re-1000)Pr\right]}{\left[1+12.7\left(\frac{f}{8}\right)^{\frac{1}{2}}(Pr^{\frac{2}{3}}-1)\right]}$ <p>for <math>0.5 &lt; Pr &lt; 2000, 3000 &lt; Re, &lt; 5 * 10^6</math></p> $f = [0.79 \ln(Re) - 1.64]^{-2}$ <p>for <math>3000 &lt; Re &lt; 5 * 10^6</math></p> |  <p>The diagrams illustrate five different rib geometries for a duct: 1. Circular holes: A duct with a height of 30 and a width of 20, featuring seven circular holes. 2. Narrow holes: A duct with a height of 20.84 and a width of 4, featuring seven narrow rectangular holes. 3. Wide holes: A duct with a height of 20.84 and a width of 4, featuring seven wide rectangular holes. 4. Circular 7 holes: A duct with a height of 20.45 and a width of 32.14, featuring seven circular holes. 5. Circular 11 holes: A duct with a height of 20.45 and a width of 32.14, featuring eleven circular holes.</p> | <p><math>T_w = 35.42 \text{ }^\circ\text{C}</math><br/> <math>T_m = 27.75 \text{ }^\circ\text{C}</math><br/> <math>41.2 \text{ }^\circ\text{C}</math><br/> <math>T_i = 27.5 \text{ }^\circ\text{C/w}</math><br/> <math>\sqrt{\alpha/k} = 0.0018634</math><br/> <math>T = 30 \text{ s}</math><br/> <math>K = 0.0263 \text{ W/mK}</math><br/> <math>H = 264.59 \text{ W/mK}</math></p> | <p>The percentage of the Nu and the TPF decreased as the Re increased. The wall of the blockage with broad holes gave a more uniform coefficient of heat transfer and better thermal efficiency. Whereas the number of holes rose to between 7 and 11, the convective heat transfer distribution grew constant and the TPF rose.</p> |

## 11. Effectiveness of Geometry and Operating Parameters of Artificial Roughened SAH

The  $Nu$  and  $f$ , the effectiveness of SAH with an artificially rough surface, was evaluated with a smooth SAH. Lewis [191] evaluated the roughness features of the heat-transfer roughness function  $g(e^+, Pr)$  and momentum transfer roughness function  $R(e^+)$ . The variable  $g(e^+, Pr)$  depicts the rough surface's capacity to transport heat, whereas  $R(e^+)$  indicates the momentum losses caused by the surface's roughness.  $G(e^+, Pr)$  and  $R(e^+)$  may be represented as functions of roughness parameters for incompressible flow:

$$R = R(e^+, e/b, e/p, e/d, \text{roughness shape})$$

$$g = g(e^+, e/b, e/p, e/d, \text{roughness shape})$$

Many researchers correlate  $Nu$  and  $f$  in an SAH duct regarding  $Re$ , roughness, and duct parameters. The  $Nu$  and  $f$  are expressed as follows:

$$Nu = Nu[Re, p/e, e/D, \alpha], \text{ rib geometry, duct shape;}$$

$$f = f[Re, p/e, e/D, \alpha], \text{ rib geometry, duct shape;}$$

### 11.1. Effect of Absorber-Roughness Parameters

Major geometric characteristics that influence SAH effectiveness include relative roughness pitch ( $P/e$ ), aspect ratio ( $W/H$ ), relative roughness height ( $e/D_h$ ), angle of attack ( $\alpha$ ), relative roughness width ( $W/w$ ), open-area ratio ( $\beta$ ), relative gap position ( $d/w$  or  $Gd/Lv$ ), and relative gap width ( $g/e$ ). Investigators showed the findings of their experiments using a range of artificial roughness and tuned the geometric properties for optimal thermo-hydraulic performance (THP) [37,192–194]. During the empirical examination, specific ambient characteristics, such as surrounding temperature, surrounding pressure, and solar irradiance, are held constant. The temperature rise parameter ( $\Delta T/l$ ) and Reynolds number ( $Re$ ) are operational variables with changeable values. Numerous scholars have shown a correlation between heat transmission and friction in an SAH duct regarding  $Re$ , roughness characteristics, and duct characteristics. The effects of each geometric parameter are detailed in this section.

#### 11.1.1. Effect of Relative Roughness Pitch ( $P/e$ )

At a  $p/e$  pitch of 8, reattachment of the shear layer is difficult due to flow isolation downstream. The maximum heat transmission happens in the reattachment zone. Reduction in  $P/e$  value for fixed  $e/D$  or increase in  $e/D$  for fixed  $P/e$  to improve heat transfer is shown in Figure 40. The  $P/e$  value can be adjusted up to a value of 10, beyond which the heat-transfer enhancement decreases [181].

#### 11.1.2. Effect of Relative Roughness Height ( $e/D$ )

The influence of rib height on the effectiveness of the SAH duct was explored by Prasad and Saini [159] and Prasad and Verma [181]. It had no influence on the thermal transmission and pressure decrease when the measurements of the rib  $I <$  the transition sub-layer thickness ( $\delta$ ), i.e.,  $e < \delta$ , as shown in their study, but when rib height approached the thickness equal to the laminar sub-layer thickness, i.e.,  $e \geq \delta$ , heat transmission had a greater impact, with a mild impact on pressure decrease. Furthermore, if rib height is going far beyond the laminar sub-layer thickness i.e.,  $e \gg \delta$ , due to the likely influence of produced turbulence within a turbulence region, pressure losses will be excessively large relative to the heat-transfer rate. Figure 41 shows flow patterns on a rib with varying rib  $e/D_h$  [159].

#### 11.1.3. Effect of Duct Aspect Ratio ( $W/H$ )

Aspect ratio ( $W/H$ ) refers to the width-to-height ratio of an SAH channel. SAH is an example of an unevenly heated rectangular channel in which one or both (two) sides exhibit constant heat flow. Low channel height is frequently used for ordinary purposes.

Consequently,  $W/H$  plays a crucial role in determining the effectiveness of SAH. High  $W/H$  values results in a low channel height at a fixed cross-section, bringing the heated face of the plate near to the adjacent wall, and minimizes the airflow in the channel, which allows the primary flow to enter the interface with the heating element.  $W/H$  has been a contender for investigation in turbo rotor-blade passages and micro-channels, but it has not been given much consideration in SAH studies. Gas-turbine propellers and micro-channels work at very low (4) as well as very high ( $>15$ )  $W/H$  values, respectively, whereas SAH performs in the midrange of  $W/H$  and the stream is always turbulent, which is the justification [195]. The  $W/H$  effect becomes unimportant; thus, in the majority of the experiments, it is obtained as an optimum value in-between 8 and 12, as shown in Figure 33.

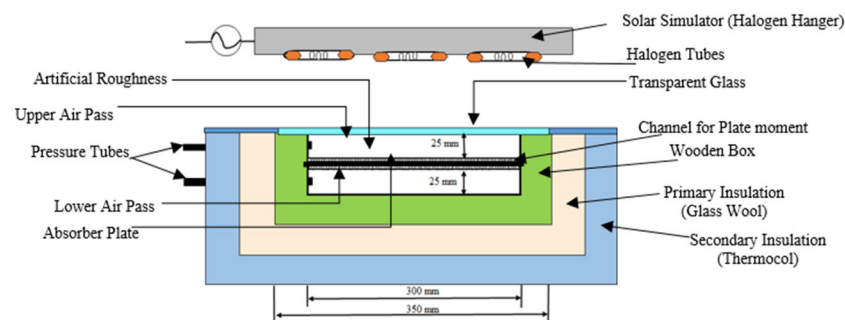


**Figure 33.** Side view of a DPPFSAH where  $H = 25$  mm,  $W = 300$  mm, and  $W/H = 12$ .

#### 11.1.4. Effect of Angle of Attack ( $\alpha$ )

The angle of attack ( $\alpha$ ) of the flow with respect to the placement of the ribs or the rib's skewness with respect to the stream is another crucial factor that determines the flow pattern. Due to the rib's angle, which generates span-wise counter-rotating secondary flow vortices, the rate of heat transmission varies dramatically. As seen in Figure 34, as the vortices flow along the rib and eventually join the mainstream. Moving vortices create turbulence that brings more excellent increases in the heat-transfer rate at the leading end by bringing fluid into the interface with it, whereas the heat-exchange rate at the leading end is rather low. This effect shows substantial heat-transmission fluctuations over the span [196].

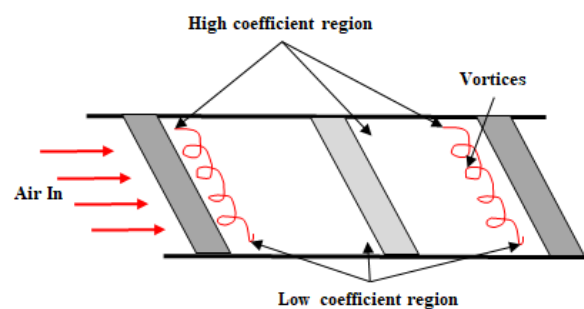


**Figure 34.** Effect of inclination of the rib, reprinted with permission [155], 2022, Elsevier.

#### 11.1.5. Effect of Relative Roughness Width ( $W/w$ )

This reflects the rib-geometry numbers throughout the width; the higher the ratio of  $W/w$ , the greater the rib-geometry number, but the smaller the rib size. Air hits the center of V-shaped or arc-shaped ribs, and secondary flow is generated across both sides of the rib architecture. The frequency of ribs rises span-wise with an increase in  $W/w$ , resulting in an increase in the number of secondary flows in the span-wise orientation, which generates a great deal of turbulence and distinguishing combinations between the two temperature streams. Because of the decrease in the length of separate rib branches, the rib's strength decreases, resulting in the production of a boundary that impedes heat transmission and eliminates secondary flow. Multiple experiments have been undertaken to determine the

optimal value of  $W/w$ , and the majority of studies agree that  $W/w$  6 provides the most heat transmission with the lowest friction loss [148,197–199] as shown in Figure 35.

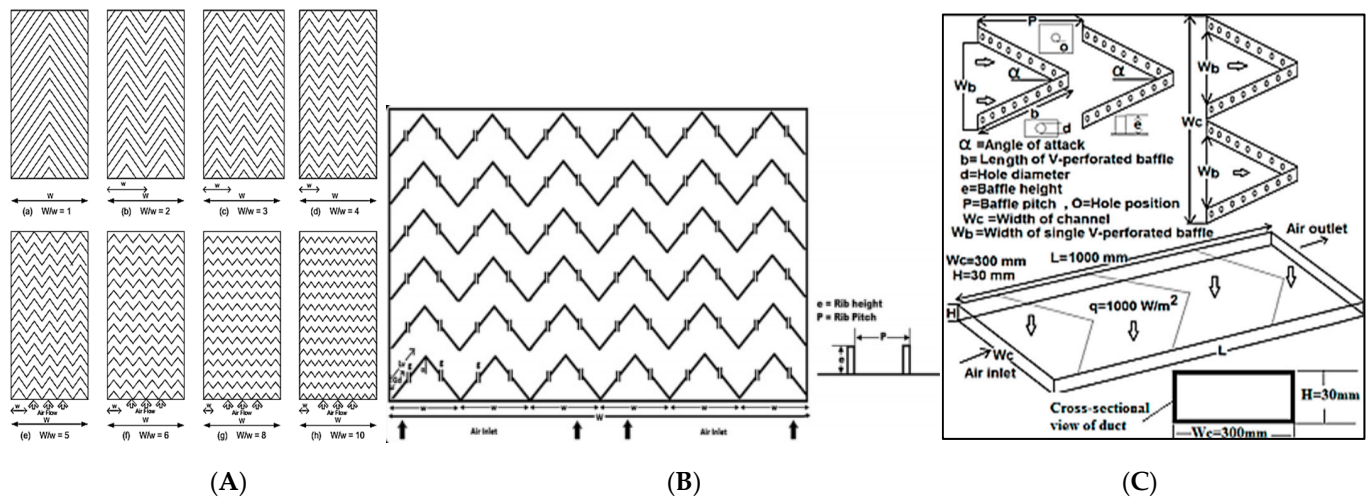


**Figure 35.** (A) Multi-V-shaped ribs with different  $W/w$ , reprinted with permission [148], 2022, Elsevier; (B) multi-V-shaped rib, reprinted with permission [197], 2022, Elsevier; (C) multi-V-perforated baffles, reprinted with permission [198,199], 2022, Elsevier.

11.1.6. Effect of Perforation (Open-Area Ratio ( $\beta$ ))

Figure 36a,b briefly describes that the perforation in a multi-V rib leads to complicated fluid-flow patterns at the wall surfaces compared to unbroken ribs [19]. The fluid-flow area and stream-reattachment interval beneath the ribs limit the quantity of transferred energy from the base plate [190]. Geometry parameters drive the THP enhancements, which may be addressed through the Reynolds number ( $Re$ ), rib roughness, and duct characteristics. In perforated ribs, the zone of reattachment shrinks, and the growth of upstream and downstream vertices decreases, leading to even more close connection for fresh fluid flow with the heated surface and improved thermal interaction inside the reattachment zone [60,200]. Perforation promotes mixing throughout the rib- and plate-contact area and lowers vortices for smaller Reynolds numbers, and it can accelerate the levels of turbulent mixing in the stream, the phenomenon of producing turbulence in between the two consecutive ribs. As a result of the increased turbulence, rib perforation increases THP.

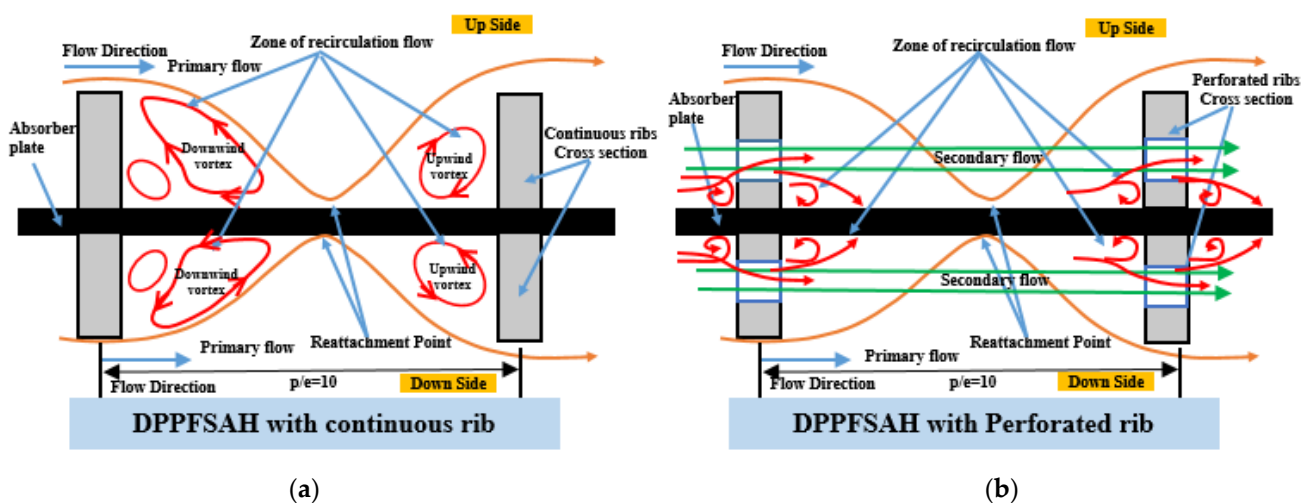


**Figure 36.** Near-wall flow development of (a) continuous rib ( $\beta = 0.0$ ) [200]; (b) perforated rib [201].

### 11.1.7. Effect of Relative Gap Position ( $d/w$ or $Gd/Lv$ or $Gd/La$ )

Ribs create a secondary flow in the duct, causing more turbulence in the flow field. Furthermore, the opening of a rib releases secondary flow units, which mix with the main flow stream to expedite it and activate the flow in the retarded boundary layer on the plate's surface, improving the duct's performance, as shown in Figure 37 [202]. Measured from the sidewall ( $d/W$ ) or the leading edge ( $Gd$ ), the relative location of the gap influences the intensity of the secondary flow. The gap at the leading edge has weaker secondary flow and considerable recirculation in the following section. Whereas the gaps location along the trailing edge have adequate strength, the temperature rise of the secondary flow along the rib hinders heat transmission with the primary flow [203].

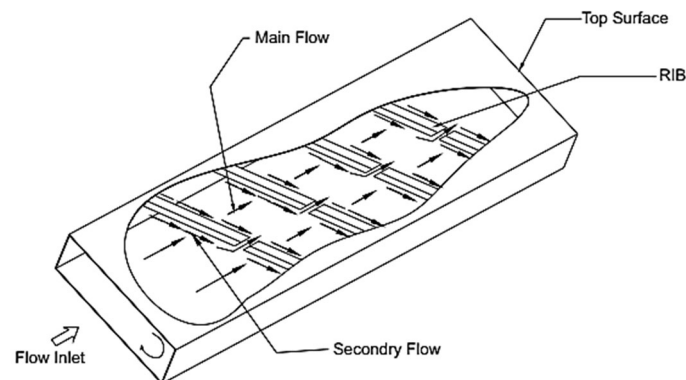


**Figure 37.** Effect of  $d/w$  or  $Gd/Lv$  or  $Gd/La$ , reprinted with permission [191], 2022, Elsevier.

### 11.1.8. Effect of Relative Gap Width ( $g/e$ )

Intercostal spaces and related characteristics: Whenever a rib is fragmented or contains a space in its limbs, it is referred to as broken, discontinuous, or a rib with gaps. The intervals in the continual ribs decrease frictional resistance, direct secondary flow, and allow a vortex to combine with the primary flow. Therefore, to accomplish this, several studies utilizing various rib-gap parameters have indeed been undertaken: relative gap breadth ( $g/e$ ), relative gap location from sidewalls ( $d/W$ ), relative gap positioning from any of the outer parts ( $Gd/Lv$ ), number of gaps ( $N_g$ ), both symmetrical and asymmetrical spaces, etc. Recent advances in the study of enhancement of the heat transfer of an SAH with repeating rib roughness include ribs with gaps. Now, continuous ribs are solely researched to determine the impact of a change in the cross-sectional area. Secondary flow and vortices may easily pass through inclined ribs, but they must travel a great distance to reach the sidewalls, which increases traffic upstream of the ribs and creates a dead zone at the side walls. It results in a homogeneous heat transfer throughout the span, and there is no dead zone at the sides since comparatively little secondary flow reaches the sidewalls [196]. Secondary-flow and dead-zone vortices interact with the main flow at several points throughout the span, which boosts heat transfer and decreases pressure drop compared to continuous ribs, as seen in variables in the research, including the gap's size, quantity, and location ( $V$ -up discrete  $>$   $V$ -down continuous  $>$   $V$ -up continuous  $>$  inclined  $>$  transverse  $>$   $V$ -up continuous) [165]. The void breaks the thick boundary condition; increases the fluid velocity through it, which in turn increases the flow pattern downstream; and raises the overall local turbulence.

Width ratio of the gaps ( $g/e$ ): The flow rate across a void is determined by its size. For  $g/e = 1$ , auxiliary flowrate is strong, but mass flux decreases significantly via the gap, and vice versa for  $g/e > 1$ . Therefore,  $g/e = 1$  provides the optimal circumstances for flow to diffuse through the gap with the necessary velocity and quantity, therefore enhancing turbulence in the main flow, as shown in Figure 38. V-shape, arc shape, and inclined ribs with a single gap provide comparable outcomes [184,202]; however, V-shape with multiple gaps yields remarkably optimal outcomes at  $g/e = 4$  [189].

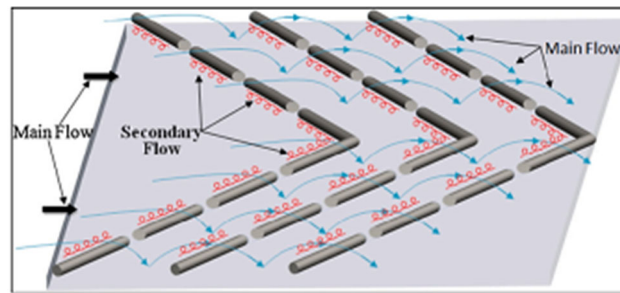


Figure 38. V-shape with gap, reprinted with permission [191], 2022, Elsevier.

#### 11.1.9. Effect of Staggering Parameters

In symmetric intervals with a low  $P/e$  ratio, the flow increases, and the majority of it reaches the next downward gaps without creating significant span-wise disruption. The most recent advancement in rib-with-gap construction to combat this issue is staggering ribs (Figure 39a). These are staggered and positioned at a proper distance from the downward entrance of the gaps. Increased reattachment is seen in Figure 39c, with increased heat absorbed from the base plate and more turbulence as a result of airflow splitting in the wake zone of the staggered ribs. With a little improvement in the pressure difference, Figure 39b shows that heat transmission was improved even more, but only for higher pitch levels.

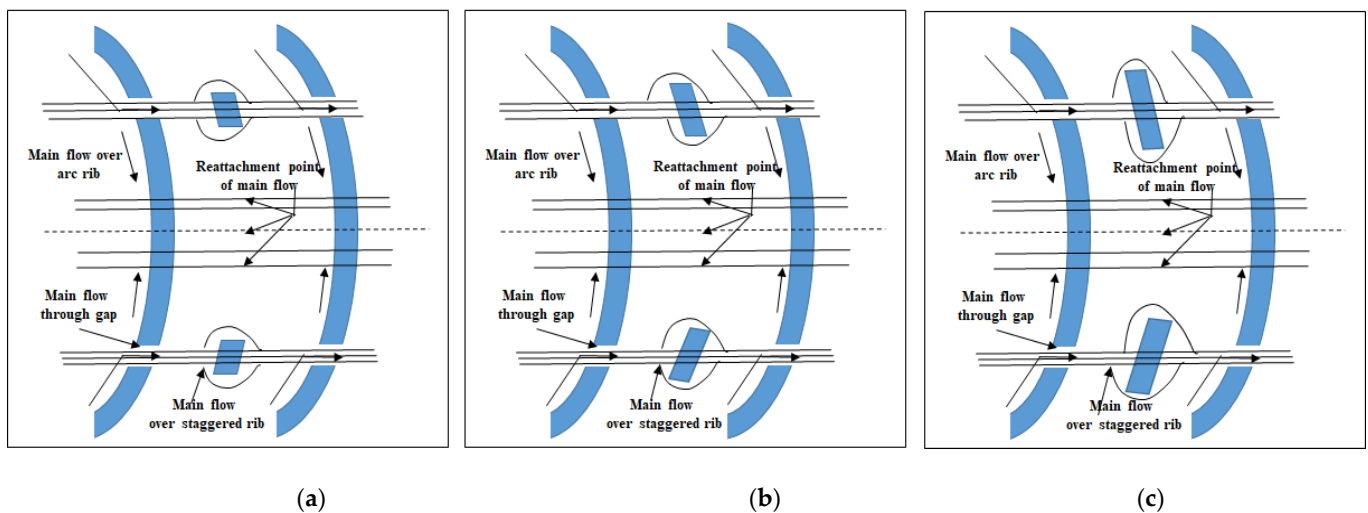


Figure 39. Different relative width with staggering (a)  $r/g = 2$ , (b)  $r/g = 4$  and (c)  $r/g = 6$ ; in rib arc [204].

#### 11.1.10. Effect of Rib Cross-Section

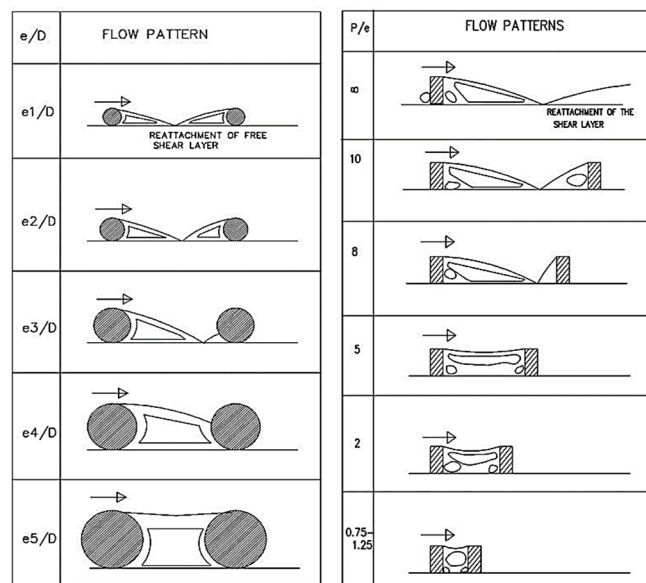
The passage in the rib affected fluid flow and the flow-separation region. Circular cross-sectional ribs demonstrated more reduced frictional losses than their rectangular or square counterparts. This is related to the contraction of the isolated flow zone. As a consequence, inertial losses decrease and surface friction rises, resulting in a reduction in the friction factor. Reduced turbulence in the flow has a significant influence on heat transmission as the size of the separated zone decreases. The drop in  $Nu$  is a result of the decreased surface area of heat transfer connected with circular cross-sections [149]. Circle, semi-circle, triangle, square, rectangle, chamfered, wedge, pentagonal, trapezoidal, ragged, semi-ellipse, and hyperbola geometries are the shapes used very frequently for the development of cross-sections of ribs.

Table 1 summarizes major investigations on SPSAH and DPPFSAH conducted by various researchers. Table 2 shows the range and values of various roughness and operational

parameters, and a comparison between THP and correlations of variation roughness are also given.

### 11.1.11. Effect of SAH Slop ( $\beta$ )

For optimal effectiveness throughout the year, the SAH gradient should be equivalent to the local latitudes. Winter temperatures should be  $10^\circ$  to  $20^\circ$  lower than the latitude values. SAH effectiveness is little influenced by the slope, but a flat SAH gets much less irradiance in the wintertime, maybe 70% less than a  $45^\circ$  collector [180]. In generally,  $45^\circ$  gets the most sunlight. Flat SAHs with  $\beta = 0^\circ$  are more popular because of the ease of manufacture and accessibility during operations.



**Figure 40.** Airflow pattern above the rib as a function of  $e/D_h$  and  $p/e$ , reprinted with permission [181], 2022, Elsevier.

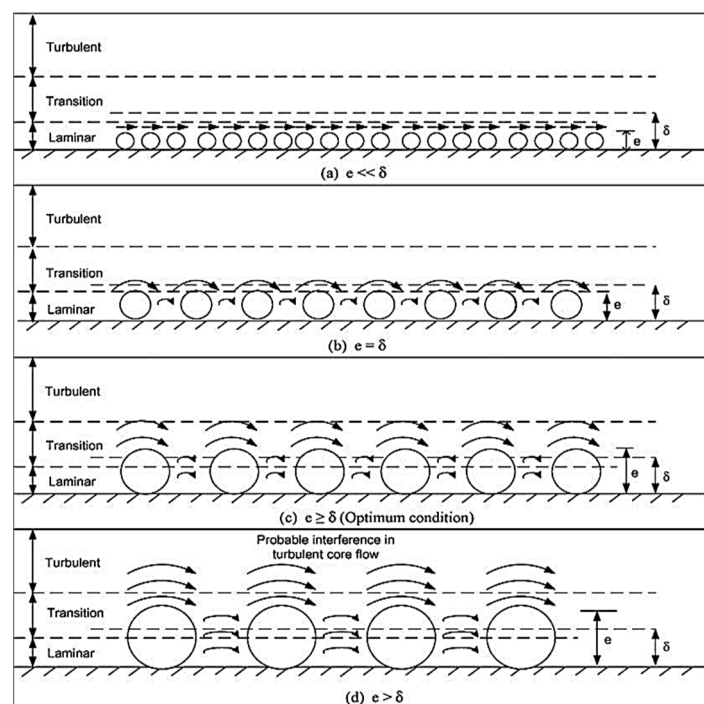


**Figure 41.** Effect of  $e/D_h$  on flow pattern, reprinted with permission [181], 2022, Elsevier.

### 11.2. Effect of Environmental Parameters on SAH Channel

Actual SAH studies take environmental factors such as solar irradiance, atmosphere and overhead temperatures, and air velocity into account. In contrast to a controlled condition, when heated plates or halogen lamps are employed as a heating element, unrestricted real-time investigations are encouraged. Controlled research allows for the modification of the variables so whole ranges may be examined.

#### 11.2.1. Solar Insolation ( $I$ )

Solar radiation is the major energy source that is subsumed by the solar collector, and the real impact of solar irradiance is more predominant at relatively high  $Re$  values. The incidence of SAH rises with increasing solar irradiance for  $Re > 10,000$ . Optimum efficiency changes to lower  $Re$  values when insolation falls for a given  $e/D_h$ , provided there is a constant  $e/D_h$ . For  $Re > 10,000$ ,  $\eta_{eff}$  drops as insolation increases.  $\eta_{eff}$  rises when  $I$  increases because of a gain in effective solar gain, and the impact is more perceptible at higher  $\Delta T/I$  values. There is little variation in performance between  $I$  values of 800 to 1000 W/m<sup>2</sup>, but it reduces substantially for 500 W/m<sup>2</sup> [197] and the reduction is greater for flat plates than for rough ones. Lower  $I$  values require lower limits of  $G$ , and inversely; hence, the airflow rate must vary during the day to maintain a steady air-temperature source.

#### 11.2.2. Temperatures of the Surrounding Air ( $T_a$ ), Sky ( $T_{sky}$ ), and Sun ( $T_{sun}$ )

These factors must be addressed when conducting real-time research. Pollution levels may increase  $T_s$  about 10 °C more than predicted by correlation. Increases bring a rise in  $T_a$  value, and the impact is more significant at high  $\Delta T/I$  since top-losses are minimized by the low-temperature differential between the cover glass and the surrounding air.  $\Delta T/I$  readings rise with  $T_{sky}$  and  $T_{sun}$  for all  $\Delta T/I$  values.

#### 11.2.3. Air Velocity ( $V_a$ ), Heat-Loss Coefficients ( $U_L$ ), and Heat-Transfer Coefficients ( $h_w$ )

Air velocity influences the effectiveness of SAH, whereas energy from the sun is used to conduct real-time, active investigations. SAH duct is topped with a glass plate and protected on the three remaining edges. However, glass and uniform insulation exhibit considerable thermal conductivity, and wind blowing beyond the established SAH-duct contributes to the energy loss from all four sides. The coefficient of heat transfers among surrounding air and all four sides is a substantial function of airspeed. The following is provided for airspeed (0.0–7.0 m/s):

$$h_w = 2.8 + 3V_w \quad (54)$$

The  $\eta_{eff}$  drops whenever  $V_w$  increases because of a rise in top losses, and the fluctuation is especially noticeable at high  $\Delta T/I$  or low flow rates when the air has a high temperature [57,205].

## 12. Thermal Performance of Artificially Roughened SAH

The heat-transfer coefficient's increasing value accounts for the SAH thermal efficiency rise [198]. Numerous studies have studied the variation in roughness geometries on the effectiveness of SAH. Prasad and Saini [159] studied the collector thermal efficiency and heat removal factor of an SAH with a tiny diameter wire on the base plate. Compared to a smooth SAH, the thermal efficiency of a collector with a rough surface increased by 1.8 times. Similar findings were reached by Gupta et al. [143], who discovered that placing transverse ribs on the base plate increased the thermal effectiveness of the SAH by 1.16 to 1.25 times. Singh et al. [199] examined the effectiveness of an SAH with discrete V-rib and discovered a 1.9-fold increase in thermal performance. Karmarea and Tikekar [206] employed the roughness of metal rib grits to demonstrate the relationship between energy usage as a function of  $Re$ , insolation ( $I$ ), and thermal efficiency as a function of different  $Re$  and relative roughness height ( $e/D_h$ ). The variation of thermal efficiency with  $Re$  and the temperature-rise parameter ( $\Delta T/I$ ) were for different values of relative roughness pitch

( $P/e$ ), angle of attack ( $\alpha$ ), insolation ( $I$ ), and relative roughness height ( $e/D_h$ ), as shown in Figures 42 and 43, respectively.

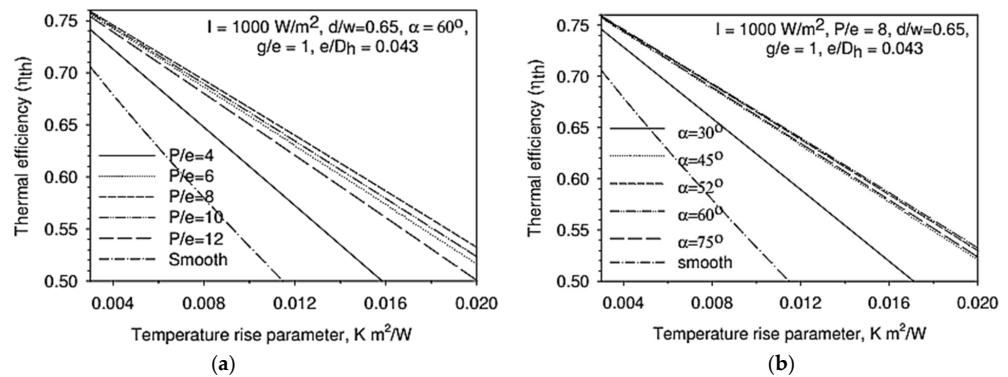


**Figure 42.**  $\eta_{th}$  as a function of  $\Delta T/I$  and (a)  $P/e$  and (b)  $\alpha$ ; reprinted with the permission from ref. [152], 2022, Elsevier.

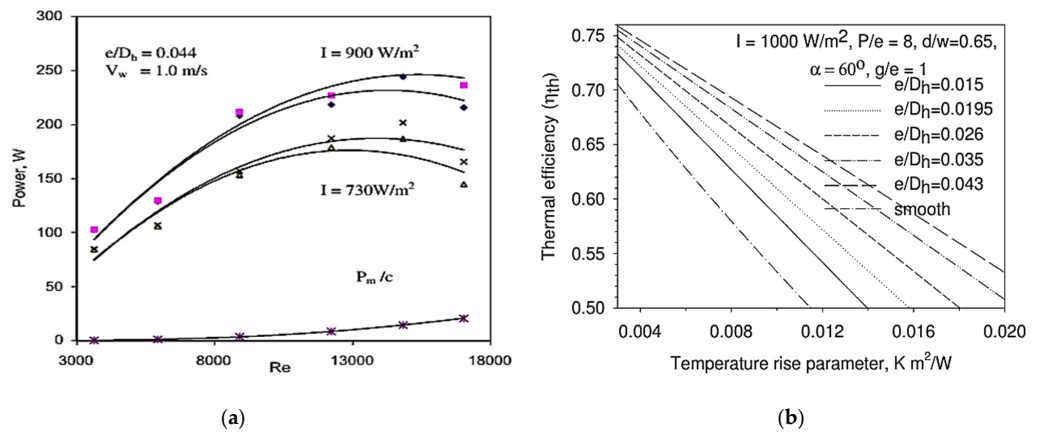


**Figure 43.**  $\eta_{th}$  as a function of  $\Delta T/I$  and different values of (a)  $I$  and (b)  $e/D_h$ ; reprinted with the permission from ref. [152], 2022, Elsevier.

Hans et al. [147] achieved a 97% change in the  $\eta_{th}$  of the SAH by employing multiple- $v$  roughness. The  $\eta_{th}$  also improved with an increase in  $Re$  values, whereas with an increase in the  $\Delta T/I$ , the  $\eta_{th}$  of the duct decreased. Kumar et al. [207] examined the  $\eta_{th}$  of an SAH duct with multi- $v$  roughness. The change in  $\eta_{th}$  with  $Re$  and  $\Delta T/I$  is shown in Figure 44. The maximum and minimum enhancement in the  $\eta_{th}$  of the duct was found to be 1.91 and 1.17 times that of a smooth channel.

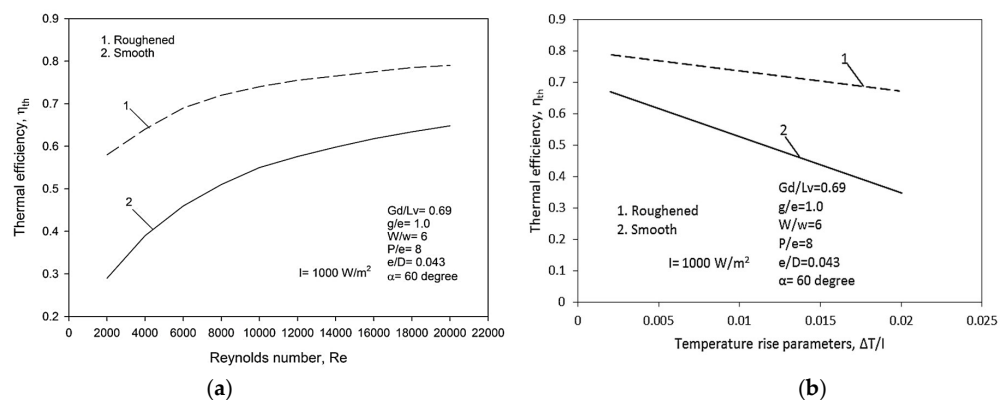


**Figure 44.**  $\eta_{th}$  as a function of (a)  $Re$  [154] and (b)  $\Delta T/I$ ; reprinted with the permission from ref. [154], 2022, Elsevier.

### 13. Thermo-Hydraulic Performance of Artificially Roughened SAH

It is noted that, by using artificial roughness in SAH, thermal performance can be enhanced simultaneously, gaining an increase in friction factor. In order to get an effective or net improvement in overall performance, it is necessary to evaluate the improvement in thermal performance with pressure drop or frictional losses. The selection of optimum roughness and operating parameters includes the determination of the improvement in the thermal efficiency along with an increment in frictional losses because of artificial roughness and higher turbulence. Therefore, to analyze the actual performance of SAH with and without the roughened absorber, the effective or thermo-hydraulic criterion was considered. Cortes and Piacentini said that the analysis should show the net energy gain after removing the equivalent energy gain that would be needed to cut down on frictional losses [208]. The expression for effective efficiency ( $\eta_{eff}$ ) can be written as:

$$\eta_{eff} = \frac{\left(Q_u - \frac{P_m}{c}\right)}{IA_c} \quad (55)$$

where concentration factor, ' $c$ ' =  $\eta_{th} \times \eta_{tr} \times \eta_F \times \eta_m$

Here,

$\eta_{th}$  is the thermal-conversion efficiency of the power plant;

$\eta_{tr}$  is the electrical-transmission efficiency;

$\eta_F$  is the fan efficiency;

$\eta_m$  is the electric-motor efficiency.

Several researchers [146,206,209–215] calculated the  $\eta_{th}$  and  $\eta_{eff}$  of intentionally roughened SAH using the correlation established in Equation (55). Karmarea and Tikekar [206] used the effective efficiency criteria to improve the geometric parameters of an artificially roughened SAH. A typical curve of  $\eta_{th}$  and  $\eta_{eff}$  as a function of  $Re$  is shown in Figure 45. The value of  $\eta_{eff}$  grows with  $Re$ , reaches a peak, and then declines with additional  $Re$  increases, but the  $\eta_{th}$  progressively increases with  $Re$  increases.

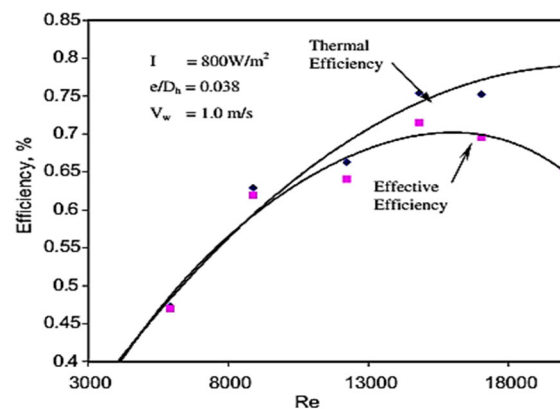


Figure 45.  $\eta_{th}$  and  $\eta_{eff}$  at various  $Re$  values; reprinted with the permission from ref. [153], 2022, Elsevier.

Hans et al. [147] produced  $\eta_{eff}$  charts for multi-V-shaped ribs in terms of  $Re$ , as illustrated in Figure 46. At a  $W/w = 6$ , the optimum value of  $\eta_{eff}$  was discovered. Similarly, Kumar et al. [83] and Mittal et al. [216] showed how exergetic efficiency ( $\eta_{exg}$ ) varies with  $Re$  and  $\Delta T/l$ . The design plots for artificially roughened SAH duct parameters, as shown in Figures 47 and 48, were provided by investigators [199,209,216] compared for different SAH ([20,41,143,147,160,163,181]). These design graphs reveal the roughness parameter's optimal values. Designers may use these charts to choose acceptable roughness settings to improve SAH thermohydraulic performance.

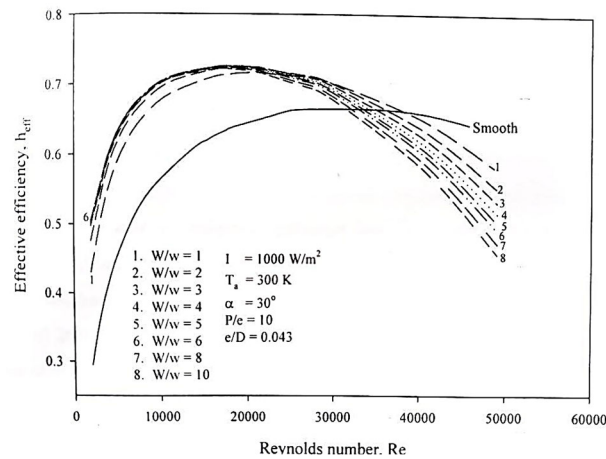


Figure 46. Effect of  $W/w$  on the  $\eta_{eff}$  in terms of  $Re$ ; reprinted with the permission from ref. [72], 2022, Elsevier.

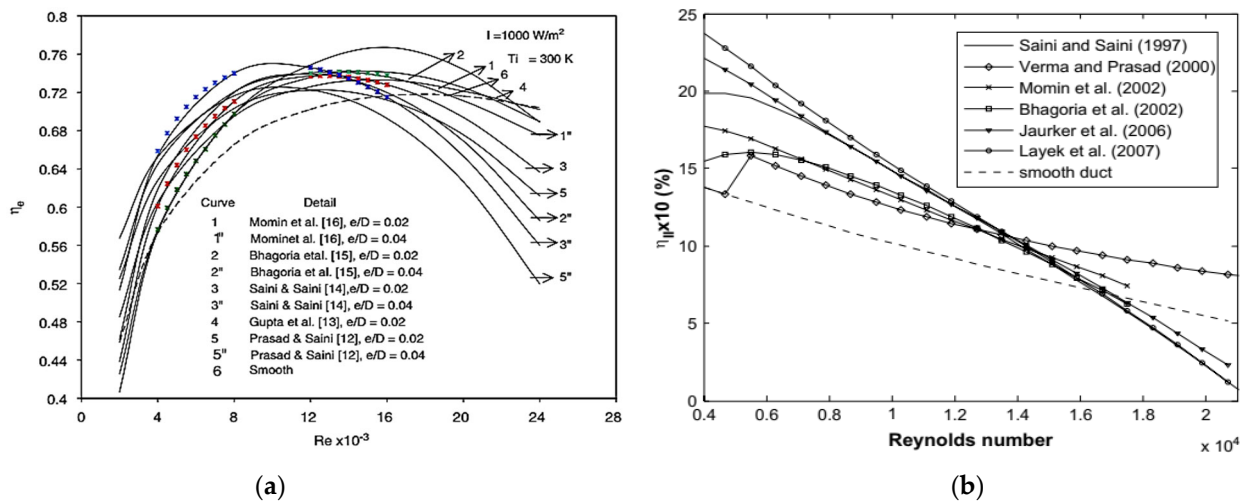


Figure 47. (a)  $\eta_{eff}$  vs.  $Re$  comparison for different authors SAH configuration ([20,143,147,160,163]) reprinted with the permission from ref. [194], 2022, Elsevier. (b)  $\eta_{exg}$  vs.  $Re$  for different SAH ([20,41,147,160,163,181]); reprinted with the permission from ref. [156], 2022, Elsevier.

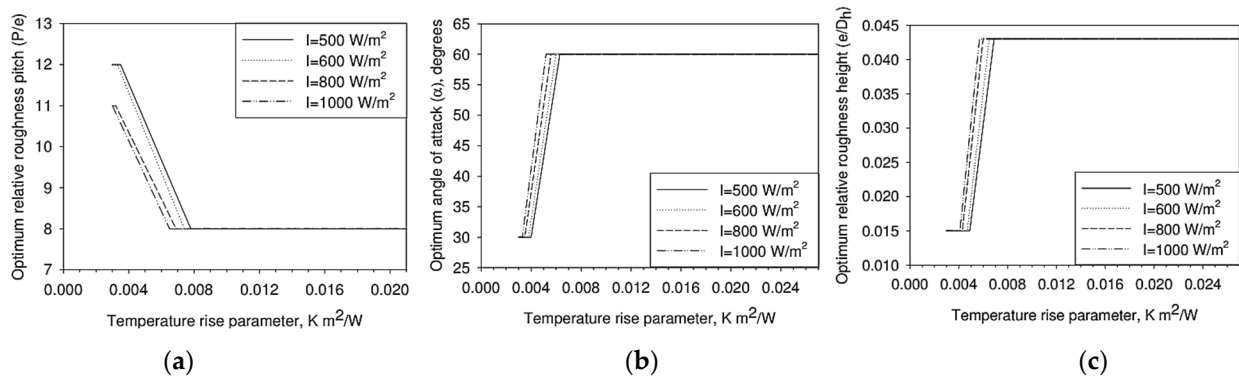


Figure 48. Optimum value plots of (a)  $p/e$ , (b)  $\alpha$ , and (c)  $e/D_h$  based on  $\eta_{eff}$  criteria; reprinted with the permission from ref. [152], 2022, Elsevier.

The cohabitation of the  $Nu$  and the  $f$  produces confusing scenarios, which makes it challenging to evaluate the genuine benefits of artificial roughness implementations. Webb-Eckert [156] established a new Thermo-Hydraulic Performance Parameter (THPP) as shown in Equation (56), that ties thermal gains to frictional losses and helps to determine

the increase in thermal gain for rough surfaces when compared to a smooth channel with identical inputs.

$$\eta_{th} = \left[ \frac{Nu}{Nu_s} \right] / \left[ \frac{f}{f_s} \right]^{1/3} \tag{56}$$

The variation in THPP with  $Re$  for different roughness is shown in Figure 49a, which compares the THP of different roughness geometries. The compaction of multi-V-shaped rib-roughness geometries done with multi-V-shaped ribs with a gap-roughness pattern demonstrated maximum effectiveness, as illustrated in Figure 49b.

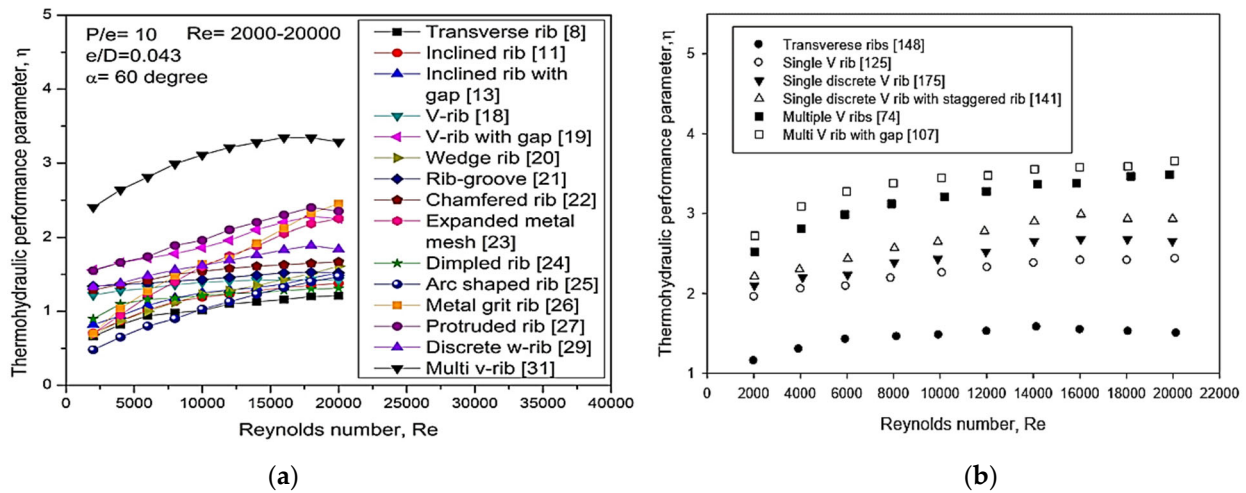


Figure 49. Comparison of THPP for various roughness geometries: (a) all types; reprinted with the permission from ref. [159], 2022, Elsevier, and (b) V-type; reprinted with the permission from ref. [181], 2022, Elsevier.

### 14. Comparison of Thermal Efficiency and Effective Efficiency for Various Roughness Shapes

The  $\eta_{th}$  of different forms of roughness elements as a function of the  $\Delta T/l$  is shown in Figure 50. By increasing the  $\Delta T/l$ -value, the  $\eta_{th}$  of all roughness geometries (inclined, single-V, multi-V, and multi-V with a gap) diminishes. The  $\eta_{th}$  of the multi-v rib with gap roughness geometry was determined to be the highest among all roughness geometries compared to the smooth SAH.

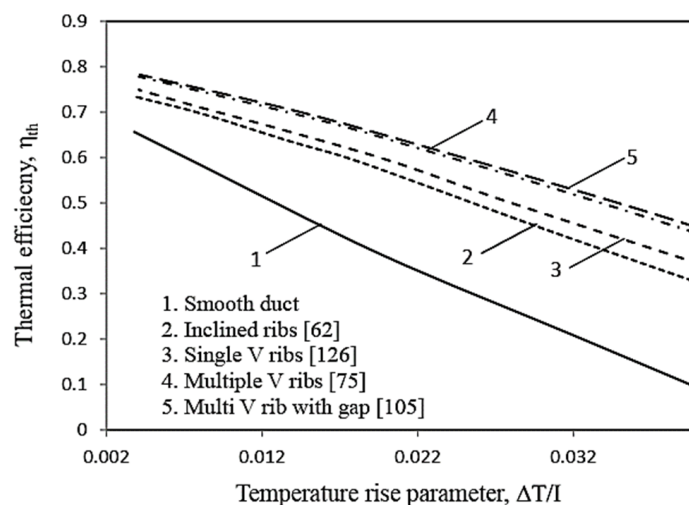
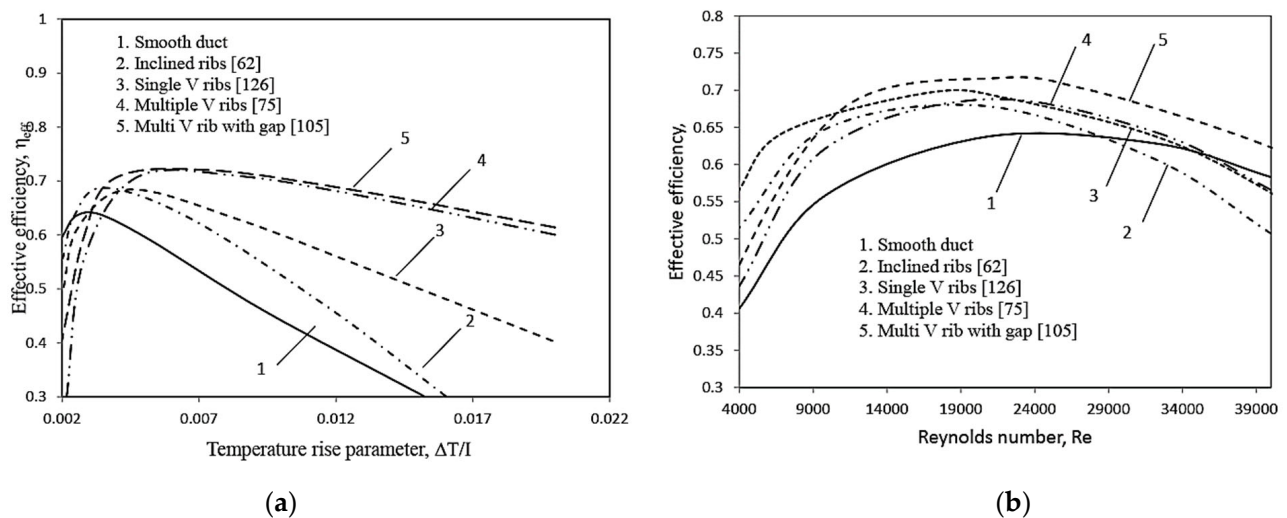


Figure 50. Comparison of  $\eta_{th}$  for various roughness shapes; reprinted with permission from ref. [180], 2022, Elsevier.

The influence of ribs like inclined, V, multi-V, and multi-V with gap geometric parameters on the SAH's effective efficiency ( $\eta_{eff}$ ) as a time function: Figure 51a,b illustrates the  $Re$  and  $\Delta T/l$ . The  $\eta_{eff}$  of the multi-V rib with gap [180] and multi-V with perforation-roughened [18,60,217] SAH had the optimum performance of all roughness geometries. However, when the  $\Delta T/l$  was low, it had a lower net output than other roughness geometries. As a result, the multi-V-rib with gap and perforation roughness should be utilized for high-temperature-range application in the DPPFSAH case, whereas the single-V rib roughness is better for improving air temperature.



**Figure 51.** Comparison of  $\eta_{eff}$  for various roughness in terms of (a)  $\Delta T/l$  and (b)  $Re$ ; reprinted with permission from ref. [180], 2022, Elsevier.

In the case of  $Re$ , a similar finding for a multi-V-rib with a gap and perforate roughness was observed, and had a far more significant impact on the  $\eta_{eff}$  of the solar air collector than other rib shapes. Increases in  $Re$  significantly increase the turbulence and provide a secondary path for fluid flow through the multi-V rib with a perforation-roughened duct, which significantly improves heat transfer over pressure losses up to a certain point, after which blower energy consumption increases, which prevents increases in  $Re$ .

## 15. Major Observations and Research Gaps Identified

Based on the detailed literature review, a significant amount of research on THPP improvement and reduction of friction value was carried out on artificially roughened SAHs with various shapes and design parameters in single- and double-pass cases. Comparative studies between single- and double-pass SAH have been conducted, and during the literature review, the following observations were made:

1. The multi-V-shaped rib is one of the best roughness geometries among all the studies. Most geometry parameters are optimized for continuous, gap, and staggered multi-V-rib roughness. However, very few works have been conducted to optimize parameters of perforated rib roughness, which perform far better than others.
2. Because of a significant increase in the contact area, the thermal performance of DPSAH improved significantly, but a considerable gain in pumping power also occurred. The overall efficiency of DPSAH was observed to be better than SPSAH in all aspects.
3. With DPSAH, most of the studies paid attention to packed bed materials and extended surfaces like fins or corrugated structures to improve the THP of SAH; only a few works of literature were available to determine the THP of the optimum roughness parameters with artificial roughness in the case of DPSAH.

4. Because of significant increases in surface area and unidirectional airflow, DPPFSAH has high heat-transfer efficiency while creating minimum drag forces and reducing pumping power [218].
5. Perforation in rib and baffle roughness provided in various rib designs significantly increases THPP compared to continuous rib configurations under similar operating conditions. During detachment and reattachment, the secondary stream's mass-flow rate is accelerated through perforations, causing further turbulence [149].
6. There was very little research available on the effect evaluation of perforation, especially in terms of variation in open-area ratio ( $\beta$ ) on THP of SAH, and only few attempts have been made to optimize the open-area ratio ( $\beta$ ) and its impact on a perforated multi-V-rib roughness in SPSAH and DPPFSAH [18].

This review recommends that a wide scope be available for the study of SAH where a comparison can be conducted between continuous ribs and perforated ribs of various shapes and sizes in single-pass SAH and double-pass SAH with parallel, cross-, and recycled flow under well-defined geometry and operational parameters by using an experimental setup, numerical modeling, or simulations. This can provide new optimum values of well-defined parameters that have already been optimized for continuous ribs under different operating conditions.

**Author Contributions:** The main contributions of authors are as follows: conceptualization: V.P.S., C.S.M. and S.J.; methodology: A.K. (Ashish Karn) and A.G.; structuring of paper: A.K. (Ashwani Kumar), G.D., A.K. (Ashish Karn) and C.S.M.; investigation and data collection: V.P.S., N.D. and G.D.; resources: S.J. and G.D.; data curation: V.P.S. and A.K. (Ashwani Kumar); writing—original draft: V.P.S. and C.S.M.; writing—review and editing: V.P.S., S.J., A.K. (Ashwani Kumar), A.G. and A.K. (Ashish Karn); visualization: S.J., G.D. and C.S.M.; supervision: S.J., A.G., C.S.M. and N.D.; project administration: S.J. and G.D. All authors have read and agreed to the published version of the manuscript.

**Funding:** This research received no external funding.

**Institutional Review Board Statement:** Not applicable.

**Informed Consent Statement:** Not applicable.

**Data Availability Statement:** Not applicable.

**Conflicts of Interest:** The authors declare no conflict of interest.

## Nomenclature

| Details of Symbols | Greek Symbols                                   |                      |   |
|--------------------|---|----------------------|---|
| A                  | Area, (m <sup>2</sup> )                         | $\Delta$             | Drop/gradient                           |
| C <sub>d</sub>     | Coefficient of discharge                        | $\delta$             | Partial                                 |
| P                  | Mean static pressure (N/m <sup>2</sup> )        | $\eta$               | Efficiency                              |
| H                  | Height (m)                                      | $\epsilon$           | Emissivity                              |
| h                  | Heat-transfer coefficient (W/m <sup>2</sup> °C) | <i>ν</i> hook        | Kinematic viscosity (m <sup>2</sup> /s) |
| I                  | Irradiance (W/m <sup>2</sup> )                  | $\alpha$             | Absorptivity                            |
| k                  | Thermal conductivity (W/m °C)                   | $\rho$               | Air density (kg/m <sup>3</sup> )        |
| t                  | Thickness (m)                                   | $\alpha$             | Angle of attack (°)                     |
| $\dot{m}$          | Air mass-flow rate (kg/s)                       | $\beta$              | Collector slope (°), open-area ratio    |
| P                  | Pitch distance (m)                              | $\mu$                | Dynamic viscosity (N.s/m <sup>2</sup> ) |
| Q                  | Thermal energy transferred (J)                  | $\psi$               | Circularity                             |
| q                  | Average heat generation (W/m <sup>3</sup> )     | $\nu$                | Kinematic viscosity (m <sup>2</sup> /s) |
| T                  | Mean temperature (°C)                           | $\tau$               | Transmissivity                          |
| W                  | Width of channel (m)                            | <b>Abbreviations</b> |   |
| w                  | Width of one set of ribs (m)                    | SP                   | Single pass                             |
| V                  | Velocity of working fluid (m/sec)               | DP                   | Double pass                             |
| D <sub>h</sub>     | Hydraulic diameter (m)                          | THPP                 | Thermohydraulic performance parameter   |
|                    | SAH   |                      | Solar air heater                        |

### Subscripts

|     |                        |     |            |
|-----|------------------------|-----|------------|
| A   | Ambient, air           | m   | Mean       |
| abs | Absorber               | u   | Useful     |
| Amb | Ambient                | th  | Thermal    |
| d   | Duct/channel, diameter | eff | Effective  |
| g   | Glass cover            | ex. | Exergetic  |
| h   | Height, hole           | Ins | Insulation |

### References

- Sukhatme, S.P.; Nayak, J.K. Solar energy in western Rajasthan. *Curr. Sci.* **1997**, *72*, 62–68. Available online: <http://www.jstor.org/stable/24098631> (accessed on 5 July 2022).
- Singh, V.P.; Jain, S.; Kumar, A. Establishment of correlations for the Thermo-Hydraulic parameters due to perforation in a multi-V rib roughened single pass solar air heater. *Exp. Heat Transf.* **2022**, 1–20. [\[CrossRef\]](#)
- Duffie, J.A.; Kalogirou, S.A.; Duffie, S.A.; Kalogirou, J.A. Solar Economic Analysis. In *Solar Energy Engineering*; Elsevier: Amsterdam, The Netherlands, 2014.
- Murthy, S.G. *Chapter Ten—Solar Energy in India*; Elsevier Inc.: Amsterdam, The Netherlands, 2022.
- Duffie, J.A.; Beckman, W.A. *Solar Engineering of Thermal Processes*, 4th ed.; John Wiley and Sons: Hoboken, NJ, USA, 2013.
- Sakthivadivel, D.; Balaji, K.; Dsilva Winfred Rufuss, D.; Iniyar, S.; Suganthi, L. Chapter 1—Solar energy technologies: Principles and applications. In *Renewable-Energy-Driven Future*; Ren, J., Ed.; Academic Press: Cambridge, MA, USA, 2021; pp. 3–42. ISBN 978-0-12-820539-6.
- Sareen, S.; Kale, S.S. Energy Research & Social Science Solar ‘power’: Socio-political dynamics of infrastructural development in two Western Indian states. *Energy Res. Soc. Sci.* **2018**, *41*, 270–278. [\[CrossRef\]](#)
- Fuqiang, W.; Ziming, C.; Jianyu, T.; Yuan, Y.; Yong, S.; Linhua, L. Progress in concentrated solar power technology with parabolic trough collector system: A comprehensive review. *Renew. Sustain. Energy Rev.* **2017**, *79*, 1314–1328. [\[CrossRef\]](#)
- Saini, M.; Sharma, A.; Singh, V.P.; Jain, S.; Dwivedi, G. Solar Thermal Receivers—A Review. *Lect. Notes Mech. Eng.* **2022**, *II*, 311–325. [\[CrossRef\]](#)
- Klein, S.A.; Beckman, W.A.; Duffie, J.A. A design procedure for solar air heating systems. *Sol. Energy* **1977**, *19*, 509–512. [\[CrossRef\]](#)
- Boer, K.W.; Duffie, J.A. *Advances in Solar Energy: An Annual Review of Research and Development Volume 2*; Springer: New York, NY, USA, 2012.
- Luo, X.; Ma, X.; Xu, Y.F.; Feng, Z.K.; Du, W.P.; Wang, R.; Li, M. Solar Water Heating System. In *Handbook of Energy Systems in Green Buildings*; Springer: Berlin/Heidelberg, Germany, 2018.
- Ravi Kumar, K.; Krishna Chaitanya, N.V.V.; Sendhil Kumar, N. Solar thermal energy technologies and its applications for process heating and power generation—A review. *J. Clean. Prod.* **2020**, *282*, 125296. [\[CrossRef\]](#)
- Kalogirou, S.A.; Florides, G.A. *Solar Space Heating and Cooling Systems*; Elsevier Inc.: Amsterdam, The Netherlands, 2016.
- Lupi, F.; Borri, C.; Harte, R.; Krätzig, W.B.; Niemann, H. J Facing technological challenges of Solar Updraft Power Plants. *J. Sound Vib.* **2015**, *334*, 57–84. [\[CrossRef\]](#)
- Alam, T.; Saini, R.P.; Saini, J.S. Heat and flow characteristics of air heater ducts provided with turbulators—A review. *Renew. Sustain. Energy Rev.* **2014**, *31*, 289–304. [\[CrossRef\]](#)
- Pandey, A.K.; Kumar, R.; Samykano, M. Chapter 1—Solar energy: Direct and indirect methods to harvest usable energy. In *Dye-Sensitized Solar Cells*; Pandey, A.K., Shahabuddin, S., Ahmad, M.S., Eds.; Academic Press: Cambridge, MA, USA, 2022; pp. 1–24.
- Singh, V.P.; Jain, S.; Gupta, J.M.L. Analysis of the effect of variation in open area ratio in perforated multi-V rib roughened single pass solar air heater—Part A. *Energy Sources Part A Recover. Util. Environ. Eff.* **2022**, *30*, 1–20. [\[CrossRef\]](#)
- Singh, V.P.; Jain, S.; Gupta, J. Analysis of the effect of perforation in multi-v rib artificial roughened single pass solar air heater—Part A. *Exp. Heat Transf.* **2021**, 1–20. [\[CrossRef\]](#)
- Prasad, B.N.; Saini, J.S. Optimal thermohydraulic performance of artificially roughened solar air heaters. *Sol. Energy* **1991**, *47*, 91–96. [\[CrossRef\]](#)
- Varshney, L.; Saini, J.S.S. Heat transfer and friction factor correlations for rectangular solar air heater duct packed with wire mesh screen matrices. *Sol. Energy* **1998**, *62*, 255–262. [\[CrossRef\]](#)
- Meena, C.S.; Raj, B.P.; Saini, L.; Agarwal, N. Performance Optimization of Solar-Assisted Heat Pump System for Water Heating Applications. *Energies* **2021**, *14*, 3534. [\[CrossRef\]](#)
- Meena, C.S.; Meena, S.; Bajpai, V.K. Correlation between absorber plate thickness  $\delta$  and collector efficiency factor  $F'$  of solar flat-plate collector. *Appl. Mech. Mater.* **2014**, 592–594, 2341–2344. [\[CrossRef\]](#)
- Deonaraine, S.S.; Satcunanathan, D. A two-pass solar air heater. *Sol. Energy* **1973**, *15*, 41–49. [\[CrossRef\]](#)
- Aldabbagh, L.; Egelioglu, F.; Ilkan, M. Single and double pass solar air heaters with wire mesh as packing bed. *Energy* **2010**, *35*, 3783–3787. [\[CrossRef\]](#)
- Hu, J.; Zhang, G. Performance improvement of solar air collector based on airflow reorganization: A review Performance improvement of solar air collector based on airflow reorganization: A review. *Appl. Therm. Eng.* **2019**, *155*, 592–611. [\[CrossRef\]](#)

27. Alam, T.; Kim, M.-H. Performance improvement of double-pass solar air heater—A state of art of review. *Renew. Sustain. Energy Rev.* **2017**, *79*, 779–793. [[CrossRef](#)]
28. Ravi, R.K.; Saini, R.P. A review on different techniques used for performance enhancement of double pass solar air heaters. *Renew. Sustain. Energy Rev.* **2016**, *56*, 941–952. [[CrossRef](#)]
29. Kumar, A.; Kumar, N.; Kumar, S.; Maithani, R. Exergetic efficiency analysis of impingement jets integrated with internal conical ring roughened solar heat collector. *Exp. Heat Transf.* **2021**, 1–21. [[CrossRef](#)]
30. Caliskan, S.; Dogan, A.; Sahin, U.R. Effect of new punched vortex generators in a rectangular channel on heat transfer using Taguchi method. *Exp. Heat Transf.* **2022**, *35*, 611–636. [[CrossRef](#)]
31. El-Sebaï, A.A.; Aboul-Enein, S.; Ramadan, M.R.I.; Shalaby, S.M.; Moharram, B.M. Investigation of thermal performance of double pass-flat and v-corrugated plate solar air heaters. *Energy* **2011**, *36*, 1076–1086. [[CrossRef](#)]
32. Metwally, M.N.; Abouziyan, H.Z.; Elleathy, A.M. Performance of advanced corrugated-duct solar air collector compared with five conventional designs. *Renew. Energy* **1997**, *10*, 519–537. [[CrossRef](#)]
33. Ozgen, F.; Esen, M.; Esen, H. Experimental investigation of thermal performance of a double-flow solar air heater having aluminium cans. *Renew. Energy* **2009**, *34*, 2391–2398. [[CrossRef](#)]
34. Fudholi, A.; Sopian, K.; Ruslan, M.H. Thermal Efficiency of Double Pass Solar Collector with Longitudinal Fins Absorbers Thermal Efficiency of Double Pass Solar Collector with Longitudinal Fins Absorbers. *Am. J. Appl. Sci.* **2011**, *8*, 254–260. [[CrossRef](#)]
35. Karim, M.A.; Hawlader, M.N.A. Performance investigation of flat plate, v-corrugated and finned air collectors. *Energy* **2006**, *31*, 452–470. [[CrossRef](#)]
36. Kumar, A.; Akshayveer; Singh, A.P.; Singh, O.P. Efficient designs of double-pass curved solar air heaters. *Renew. Energy* **2020**, *160*, 1105–1118. [[CrossRef](#)]
37. Ravi, R.K.; Saini, R.P. Experimental investigation on performance of a double pass artificial roughened solar air heater duct having roughness elements of the combination of discrete multi V shaped and staggered ribs. *Energy* **2016**, *116*, 507–516. [[CrossRef](#)]
38. Kumar, A.; Kumar, A.; Dutt, N.; Singh, V.P.; Meena, C.S.; Prasad, A. Experimental Study of Process Parameter for Surface Roughness in WEDM. *J. Mech. Eng. Prakash* **2022**, *1*, 7–13. [[CrossRef](#)]
39. Singh, S. Experimental and numerical investigations of a single and double pass porous serpentine wavy wiremesh packed bed solar air heater. *Renew. Energy* **2020**, *145*, 1361–1387. [[CrossRef](#)]
40. Hassan, H.; Yousef, M.S.; Abo-elfadl, S. Energy, exergy, economic and environmental assessment of double pass V-corrugated-perforated finned solar air heater at different air mass ratios. *Sustain. Energy Technol. Assess.* **2020**, *43*, 100936. [[CrossRef](#)]
41. Kumar, A.; Layek, A. Evaluation of the performance analysis of an improved solar air heater with Winglet shaped ribs. *Exp. Heat Transf.* **2020**, *35*, 239–257. [[CrossRef](#)]
42. Ho, C.D.; Yeh, H.M.; Wang, R.C. Heat-transfer enhancement in double-pass flat-plate solar air heaters with recycle. *Energy* **2005**, *30*, 2796–2817. [[CrossRef](#)]
43. Hassan, H.; Abo-Elfadl, S. Experimental study on the performance of double pass and two inlet ports solar air heater (SAH) at different configurations of the absorber plate. *Renew. Energy* **2018**, *116*, 728–740. [[CrossRef](#)]
44. Ho, C.-D.; Tien, Y.-E.; Hsiao, C.-F. The influences of recycle effect on double-pass V-corrugated solar air heaters. *Int. J. Green Energy* **2017**, *14*, 1083–1092. [[CrossRef](#)]
45. Nanjundappa, M. Optimum thermo-hydraulic performance of solar air heater provided with cubical roughness on the absorber surface. *Exp. Heat Transf.* **2020**, *33*, 374–387. [[CrossRef](#)]
46. Abo-Elfadl, S.; Hassan, H.; El-Dosoky, M.F.F. Study of the performance of double pass solar air heater of a new designed absorber: An experimental work. *Sol. Energy* **2019**, *198*, 479–489. [[CrossRef](#)]
47. Arunkumar, H.S.; Vasudeva Karanth, K.; Kumar, S. Review on the design modifications of a solar air heater for improvement in the thermal performance. *Sustain. Energy Technol. Assess.* **2020**, *39*, 100685. [[CrossRef](#)]
48. Sharma, S.; Kumar, A.; Maithani, R. Influence of twisted tape with collective protruded rib parameters of thermal–hydraulic performance of Al<sub>2</sub>O<sub>3</sub>-H<sub>2</sub>O nanofluid flow in heat exchanger tube. *Mater. Today Proc.* **2022**, *50*, 1129–1133. [[CrossRef](#)]
49. Forson, F.K.; Nazha, M.A.A.; Rajakaruna, H. Experimental and simulation studies on a single pass, double duct solar air heater. *Energy Convers. Manag.* **2003**, *44*, 1209–1227. [[CrossRef](#)]
50. Abdullah, A.S.; Abou Al-sood, M.M.; Omara, Z.M.; Bek, M.A.; Kabeel, A.E. Performance evaluation of a new counter flow double pass solar air heater with turbulators. *Sol. Energy* **2018**, *173*, 398–406. [[CrossRef](#)]
51. Esen, H.; Ozgen, F.; Esen, M.; Sengur, A. Artificial neural network and wavelet neural network approaches for modelling of a solar air heater. *Expert Syst. Appl.* **2009**, *36*, 11240–11248. [[CrossRef](#)]
52. Pawar, R.S.; Takwale, M.G.; Bhide, V.G. Evaluation of the performance of the solar air heater. *Energy Convers. Manag.* **1994**, *35*, 699–708. [[CrossRef](#)]
53. Hegazy, A.A. Thermohydraulic performance of air heating solar collectors with variable width, flat absorber plates. *Energy Convers. Manag.* **2000**, *41*, 1361–1378. [[CrossRef](#)]
54. Garg, H.P.; Prakash, J.; Hrishikesan, D.S. Performance prediction of a solar timber kiln. *Energy Convers. Manag.* **1993**, *34*, 569–575. [[CrossRef](#)]
55. Forson, F.K.; Nazha, M.A.A.; Rajakaruna, H. Modelling and experimental studies on a mixed-mode natural convection solar crop-dryer. *Sol. Energy* **2007**, *81*, 346–357. [[CrossRef](#)]

56. Dhiman, P.; Thakur, N.S.; Kumar, A.; Singh, S. An analytical model to predict the thermal performance of a novel parallel flow packed bed solar air heater. *Appl. Energy* **2011**, *88*, 2157–2167. [CrossRef]
57. Dhiman, P.; Thakur, N.S.; Chauhan, S.R. Thermal and thermohydraulic performance of counter and parallel flow packed bed solar air heaters. *Renew. Energy* **2012**, *46*, 259–268. [CrossRef]
58. Yeh, H.; Ho, C.; Hou, J. The improvement of collector efficiency in solar air heaters by simultaneously air flow over and under the absorbing plate. *Energy* **1999**, *24*, 857–871. [CrossRef]
59. González, S.M.; Larsen, S.F.; Hernández, A.; Lesino, G. Thermal evaluation and modeling of a double-pass solar collector for air heating. *Proc. Energy Procedia* **2014**, *57*, 2275–2284. [CrossRef]
60. Singh, V.P.; Jain, S.; Gupta, J. Performance assessment of double-pass parallel flow solar air heater with perforated multi-V ribs roughness—Part B. *Exp. Heat Transf.* **2022**, 1–18. [CrossRef]
61. Verma, R.; Chandra, R.; Garg, H.P. Optimization of solar air heaters of different designs. *Renew. Energy* **1992**, *2*, 521–531. [CrossRef]
62. Naphon, P. Effect of porous media on the performance of the double-pass flat plate solar air heater. *Int. Commun. Heat Mass Transf.* **2005**, *32*, 140–150. [CrossRef]
63. Sopian, K.; Supranto; Daud, W.R.W.; Othman, M.Y.; Yatim, B. Thermal performance of the double-pass solar collector with and without porous media. *Renew. Energy* **1999**, *18*, 557–564. [CrossRef]
64. Sopian, K.; Alghoul, M.A.; Alfegi, E.M.; Sulaiman, M.Y.; Musa, E.A. Evaluation of thermal efficiency of double-pass solar collector with porous—Nonporous media. *Renew. Energy* **2009**, *34*, 640–645. [CrossRef]
65. Kumar, N.; Kumar, A.; Maithani, R.; Iqbal, Q.; Chen, C.; Hossain, F.; Small, H.; Shenton, A.K.; Hay-Gibson, N.V.; Mayr, P.; et al. Overview of V-RIB geometries in solar air heater and performance evaluation of a new V-RIB geometry. *Renew. Energy* **2020**, *152*, 77–90. [CrossRef]
66. Naphon, P. On the performance and entropy generation of the double-pass solar air heater with longitudinal fins. *Renew. Energy* **2005**, *30*, 1345–1357. [CrossRef]
67. Nowzari, R.; Aldabbagh, L.B.Y.; Egelioglu, F. Single and double pass solar air heaters with partially perforated cover and packed mesh. *Energy* **2014**, *73*, 694–702. [CrossRef]
68. Karim, M.A.; Perez, E.; Amin, Z.M. Mathematical modelling of counter flow v-grove solar air collector. *Renew. Energy* **2014**, *67*, 192–201. [CrossRef]
69. El-Sebaai, A.A.; Aboul-Enein, S.; Ramadan, M.R.I.; Shalaby, S.M.; Moharram, B.M. Thermal performance investigation of double pass-finned plate solar air heater. *Appl. Energy* **2011**, *88*, 1727–1739. [CrossRef]
70. Wijesundera, N.E.; Ah, L.L.; Tjioe, L.E. Thermal performance study of two-pass solar air heaters. *Sol. Energy* **1982**, *28*, 363–370. [CrossRef]
71. Jin, D.; Zuo, J.; Quan, S.; Xu, S.; Gao, H. Thermohydraulic performance of solar air heater with staggered multiple V-shaped ribs on the absorber plate. *Energy* **2017**, *127*, 68–77. [CrossRef]
72. ASHRAE. Method of Testing to Determine the Thermal Performance of Solar Collectors. (ASHRAE Standard). 1985. Available online: <https://www.osti.gov/servlets/purl/575023>. (accessed on 5 July 2022).
73. Hottel, H.; Woertz, B. Performance of flat-plate solar-heat collectors. *Trans. ASME* **1942**, *64*, 324–355.
74. Bliss, R.W. The derivations of several “Plate-efficiency factors” useful in the design of flat-plate solar heat collectors. *Sol. Energy* **1959**, *3*, 55–64. [CrossRef]
75. Bondi, P.; Clcala, L.; Farina, G. Performance of black-painted solar air heaters of conventional design. *Sol. Energy* **1988**, *41*, 101–107. [CrossRef]
76. Kays, W.M.; Crawford, M.E. Convective Heat and Mass Transfer. In *McGraw Hill Series in Mechanical Engineering*; McGraw-Hill: New York, NY, USA, 1993; Volume 3.
77. Majumdar, A. *Handbook of Heat Transfer*; Rohsenow, W.M., Hartnett, J.R., Cho, Y.I., Eds.; McGraw-Hill: New York, NY, USA, 1998.
78. Niles, P.W.; Carnegie, E.J.; Pohl, J.G.; Cherne, J.M.; Resources, N.; Obispo, S.L.; Division, E.; Beach, R. Design and performance of an air collector. *Transition* **1978**, *20*, 19–23.
79. Klein, S.A.; Duffie, J.A.; Beckman, W.A. Transient considerations of flat-plate solar collectors. *J. Eng. Gas Turbines Power* **1974**, *96*, 109–113. [CrossRef]
80. Hill, J.E.; Kelly, G.E.; Geist, J.C.; Kusuda, T. *Development of Proposed Standards for Testing Solar Collectors and Thermal Storage Devices*. NBS Technical Note 899; U.S. Government Printing Office: Washington, DC, USA, 1981; pp. 1–265.
81. Hill, J.E.; Jenkins, J.P.; Jones, D.E. Testing of Solar Collectors According To Ashrae Standard 93–77. *ASHRAE Trans.* **1978**, *84*, 107–125.
82. Reddy, T.A.; Gupta, C.L. Generating application design data for solar air heating systems. *Sol. Energy* **1980**, *25*, 527–530. [CrossRef]
83. Kumar, A.; Saini, R.P.P.; Saini, J.S.S. A review of thermohydraulic performance of artificially roughened solar air heaters. *Renew. Sustain. Energy Rev.* **2014**, *37*, 100–122. [CrossRef]
84. Kumar, B.; Kumar, M.; Patil, A.K.; Jain, S. Effect of V cut in perforated twisted tape insert on heat transfer and fluid flow behavior of tube flow: An experimental study. *Exp. Heat Transf.* **2019**, *32*, 524–544. [CrossRef]
85. Kumar, B.; Patil, A.K.; Jain, S.; Kumar, M. Study of Entropy Generation in Heat Exchanger Tube with Multiple v Cuts in Perforated Twisted Tape Insert. *J. Heat Transf.* **2019**, *141*, 081801. [CrossRef]
86. Pandey, R.; Kumar, M.; Saini, J.S. Experimental study of parametric influence on heat transfer and friction in a rectangular duct having V-down baffle blocks with staggered racetrack-shaped openings. *Exp. Heat Transf.* **2021**, *345*, 818–847. [CrossRef]

87. Patnaik, A.; Saini, R.P.P.; Singal, S.K.K. Siddhartha Performance prediction of solar air heater having roughened duct provided with transverse and inclined ribs as artificial roughness. *Renew. Energy* **2009**, *34*, 2914–2922. [[CrossRef](#)]
88. Saini, R.P.; Singal, S.K. A review on roughness geometry used in solar air heaters. *Sol. Energy* **2007**, *81*, 1340–1350. [[CrossRef](#)]
89. Sharma, A.; Goel, V.; Bharadwaj, G. Heat transfer and friction characteristics of double pass solar air heater having V-shaped roughness on the absorber plate Heat transfer and friction characteristics of double pass solar air heater having V-shaped roughness on the absorber plate. *J. Renew. Sustain. Energy* **2013**, *5*, 023109. [[CrossRef](#)]
90. Rana, J.; Silori, A.; Maithani, R.; Chamoli, S. Computational fluid dynamics analysis of a V-rib with gap roughened solar air heater. *Therm. Sci.* **2018**, *22*, 963–972. [[CrossRef](#)]
91. Ghritlahre, H.K.; Prasad, R.K. Prediction of heat transfer of two different types of roughened solar air heater using Artificial Neural Network technique. *Therm. Sci. Eng. Prog.* **2018**, *8*, 145–153. [[CrossRef](#)]
92. Fan, W.; Kokogiannakis, G.; Ma, Z. Optimisation of life cycle performance of a double-pass photovoltaic thermal-solar air heater with heat pipes. *Renew. Energy* **2019**, *138*, 90–105. [[CrossRef](#)]
93. Kumar, A. Analysis of heat transfer and fluid flow in different shaped roughness elements on the absorber plate solar air heater duct. *Proc. Energy Procedia* **2014**, *57*, 2102–2111. [[CrossRef](#)]
94. Bisht, V.S.; Patil, A.K.; Gupta, A. Compact solar air heater: A review. *Lect. Notes Mech. Eng.* **2019**, *1*, 273–281. [[CrossRef](#)]
95. Velmurugan, P.; Kalaivanan, R. Energy and exergy analysis of multi-pass flat plate solar air heater-an analytical approach. *Int. J. Green Energy* **2015**, *12*, 810–820. [[CrossRef](#)]
96. Ghritlahre, H.K.; Verma, M. Accurate prediction of exergetic efficiency of solar air heaters using various predicting methods. *J. Clean. Prod.* **2020**, *288*, 125115. [[CrossRef](#)]
97. Jin, D.; Zhang, M.; Wang, P.; Xu, S. Numerical investigation of heat transfer and fluid flow in a solar air heater duct with multi V-shaped ribs on the absorber plate. *Energy* **2015**, *89*, 178–190. [[CrossRef](#)]
98. Deo, N.S.N.S.; Chander, S.; Saini, J.S. Performance analysis of solar air heater duct roughened with multigap V-down ribs combined with staggered ribs. *Renew. Energy* **2016**, *91*, 484–500. [[CrossRef](#)]
99. Colakoglu, M.; Durmayaz, A. Multiobjective Optimization of a Novel Solar Tower-Based Gas Turbine-Driven Multi-Generation Plant with Energy, Exergy, Economic, and Environmental Impact Analysis. *J. Energy Resour. Technol.* **2022**, *144*, 051302. [[CrossRef](#)]
100. Saravanan, A.; Murugan, M.; Reddy, M.S.; Ranjit, P.S.; Elumalai, P.V.; Kumar, P.; Sree, S.R. Thermo-hydraulic performance of a solar air heater with staggered C-shape finned absorber plate. *Int. J. Therm. Sci.* **2021**, *168*, 107068. [[CrossRef](#)]
101. Thakur, D.S.; Khan, M.K.; Pathak, M. Solar air heater with hyperbolic ribs: 3D simulation with experimental validation. *Renew. Energy* **2017**, *113*, 357–368. [[CrossRef](#)]
102. Kumar, A.; Kim, M.H. Heat transfer and fluid flow characteristics in air duct with various V-pattern rib roughness on the heated plate: A comparative study. *Energy* **2016**, *103*, 75–85. [[CrossRef](#)]
103. Lanjewar, A.; Bhagoria, J.L.L.; Sarviya, R.M. Heat transfer and friction in solar air heater duct with W-shaped rib roughness on absorber plate. *Energy* **2011**, *36*, 4531–4541. [[CrossRef](#)]
104. Kumar, R.; Goel, V.; Singh, P.; Saxena, A.; Kashyap, A.S.; Rai, A. Performance evaluation and optimization of solar assisted air heater with discrete multiple arc shaped ribs. *J. Energy Storage* **2019**, *26*, 100978. [[CrossRef](#)]
105. Rajaseenivasan, T.; Srinivasan, S.; Srithar, K. Comprehensive study on solar air heater with circular and V-type turbulators attached on absorber plate. *Energy* **2015**, *88*, 863–873. [[CrossRef](#)]
106. Tanda, G. Performance of solar air heater ducts with different types of ribs on the absorber plate. *Energy* **2011**, *36*, 6651–6660. [[CrossRef](#)]
107. Al-Shamani, A.N.; Sopian, K.; Mohammed, H.A.; Mat, S.; Ruslan, M.H.; Abed, A.M. Enhancement heat transfer characteristics in the channel with Trapezoidal rib-groove using nanofluids. *Case Stud. Therm. Eng.* **2015**, *5*, 48–58. [[CrossRef](#)]
108. Salih, S.M.; Jalil, J.M.; Najim, S.E. Double-Pass Solar air Heater (DP-SAH) utilizing Latent Thermal Energy Storage (LTES). *IOP Conf. Ser. Mater. Sci. Eng.* **2019**, *518*, 032038. [[CrossRef](#)]
109. Bhowmik, H.; Amin, R. Efficiency improvement of flat plate solar collector using reflector. *Energy Rep.* **2017**, *3*, 119–123. [[CrossRef](#)]
110. Samdarshi, S.K.; Mullick, S.C. Analysis of the top heat loss factor of flat plate solar collectors with single and double glazing. *Int. J. Energy Res.* **1990**, *14*, 975–990. [[CrossRef](#)]
111. Souka, A.F. Double exposure flat-plate collector. *Sol. Energy* **1965**, *9*, 117–118. [[CrossRef](#)]
112. Suri, R.K.; Saini, J.S. Performance Prediction of Single- and Double-Exposure Solar-air Heaters. *Sol. Energy* **1969**, *12*, 525–530. [[CrossRef](#)]
113. Ward, D.A.N.S.; Weiss, T.A.; Lof, G.O.G. Preliminary performance of CSU Solar House I heating and cooling system. *Sol. Energy* **1976**, *18*, 541–548. [[CrossRef](#)]
114. Ward, D.S.; Löf, G.O.G.; Smith, C.C.; Shaw, L.L. Design of a solar heating and cooling system for CSU solar house II. *Sol. Energy* **1977**, *19*, 79–85. [[CrossRef](#)]
115. Selçuk, K. Thermal and economic analysis of the overlapped-glass plate solar-air heater. *Sol. Energy* **1971**, *13*, 165–191. [[CrossRef](#)]
116. Malhotra, A.; Garg, H.P.; Rani, U. Minimizing convective heat losses in flat plate solar collectors. *Sol. Energy* **1980**, *25*, 521–526. [[CrossRef](#)]
117. Abuşka, M.; Şevik, S.; Kayapınar, A. Experimental analysis of solar air collector with PCM-honeycomb combination under the natural convection. *Sol. Energy Mater. Sol. Cells* **2019**, *195*, 299–308. [[CrossRef](#)]

118. Buchberg, H.; Edwards, D.K.; Mackenzie, J.D.; Science, A.; Angeles, L. *Transparent Glass Honeycomb Structures for Energy Loss Control*; Technical Report UCLA-ENG-8; School of Engineering and Applied Science, California University: Los Angeles, CA, USA, 1980.
119. Buchberg, H.; Edwards, D.K. Design considerations for solar collectors with cylindrical glass honeycombs. *Sol. Energy* **1976**, *18*, 193–203. [[CrossRef](#)]
120. Caouris, Y.; Rigopoulos, R.; Tripanagnostopoulos, J.; Yianoulis, P. A novel solar collector. *Sol. Energy* **1978**, *21*, 157–160. [[CrossRef](#)]
121. Mohamad, A.A. High efficiency solar air heater. *Sol. Energy* **1997**, *60*, 71–76. [[CrossRef](#)]
122. Persad, P.; Satcunanathan, S. The Thermal Performance of the Air Heater. *J. Sol. Energy Eng. ASME* **1983**, *105*, 254–258. [[CrossRef](#)]
123. Sodha, M.S.; Bansal, N.K.; Singh, D. Analysis of a non-porous double-flow solar air heater. *Appl. Energy* **1982**, *12*, 251–258. [[CrossRef](#)]
124. Choudhury, C.; Chauhan, P.M.; Garg, H.P. Performance and cost analysis of two-pass solar air heaters. *Heat Recover. Syst. CHP* **1995**, *15*, 755–773. [[CrossRef](#)]
125. Klein, S.A. Calculation of flat-plate collector loss coefficients. *Sol. Energy* **1975**, *17*, 79–80. [[CrossRef](#)]
126. Agarwal, V.K.; Larson, D.C. Calculation of the top loss coefficient of a flat-plate collector. *Sol. Energy* **1981**, *27*, 69–71. [[CrossRef](#)]
127. Nayak, R.K.; Singh, S.N. Effect of geometrical aspects on the performance of jet plate solar air heater. *Sol. Energy* **2016**, *137*, 434–440. [[CrossRef](#)]
128. Soni, A.; Singh, S.N. Experimental analysis of geometrical parameters on the performance of an inline jet plate solar air heater. *Sol. Energy* **2017**, *148*, 149–156. [[CrossRef](#)]
129. Matheswaran, M.M.; Arjunan, T.V.; Muthusamy, S.; Natrayan, L.; Panchal, H.; Subramaniam, S.; Khedkar, N.K.; El-Shafay, A.S.; Sonawane, C. A case study on thermo-hydraulic performance of jet plate solar air heater using response surface methodology. *Case Stud. Therm. Eng.* **2022**, *34*, 101983. [[CrossRef](#)]
130. Choudhury, C.; Garg, H.P.; Khas, H. Evaluation of a jet plate solar air heater. *Sol. Energy* **1991**, *46*, 199–209. [[CrossRef](#)]
131. Behura, A.K.; Kumar, A.; Todkari, V.C.; Dwivedi, G.; Gupta, H.K. Analysis of thermal efficiency of solar flat plate collector using twisted tape. In *Advances in Air Conditioning and Refrigeration; Lecture Notes in Mechanical Engineering*; Springer: Berlin/Heidelberg, Germany, 2021; pp. 89–97. [[CrossRef](#)]
132. Yeh, H.; Ho, C.; Hou, J. Collector efficiency of double-flow solar air heaters with fins attached. *Energy* **2002**, *27*, 715–727. [[CrossRef](#)]
133. Ho, C.-D.; Yeh, H.-M.; Chen, T.-C. Collector efficiency of upward-type double-pass solar air heaters with fins attached. *Int. Commun. Heat Mass Transf.* **2011**, *38*, 49–56. [[CrossRef](#)]
134. Joudi, K.A.; Mohammed, A.I. Experimental performance of a solar air heater with a “V” corrugated absorber. *Energy Convers. Manag.* **1986**, *26*, 193–200. [[CrossRef](#)]
135. HONG, S.W.; BERGLES, A.E. Augmentation of Laminar Flow Heat Transfer in Tubes By Means of Twisted-Tape Inserts. *J. Heat Transf.* **1976**, *98*, 251–256. [[CrossRef](#)]
136. Wen, M.Y.; Jang, K.J.; Yang, C.C. Augmented heat transfer and pressure drop of strip-type inserts in the small tubes. *Heat Mass Transf. Stoffuebertragung* **2003**, *40*, 133–141. [[CrossRef](#)]
137. Chiou, J.P.; El-Wakil, M.M.; Duffie, J.A. A slit and expanded aluminum foil matrix solar collector. *Sol. Energy* **1965**, *9*, 73–80. [[CrossRef](#)]
138. Toğrul, I.T.; Pehlivan, D. Effect of packing in the airflow passage on the performance of a solar air-heater with conical concentrator. *Appl. Therm. Eng.* **2005**, *25*, 1349–1362. [[CrossRef](#)]
139. Prasad, S.B.; Saini, J.S.; Singh, K.M. Investigation of heat transfer and friction characteristics of packed bed solar air heater using wire mesh as packing material. *Sol. Energy* **2009**, *83*, 773–783. [[CrossRef](#)]
140. Kumar, A.; Kim, M.-H. Solar air-heating system with packed-bed energy-storage systems. *Renew. Sustain. Energy Rev.* **2017**, *72*, 215–227. [[CrossRef](#)]
141. Tiwari, P.; Kumar, A.; Sarviya, R.M. Thermal performance of packed bed solar air heater. In *Proceedings of the 2013 International Conference on Energy Efficient Technologies for Sustainability, ICEETS 2013, Nagercoil, India, 10–12 April 2013*; pp. 438–442.
142. Zheng, W.; Zhang, H.; You, S.; Fu, Y.; Zheng, X. Thermal performance analysis of a metal corrugated packing solar air collector in cold regions. *Appl. Energy* **2017**, *203*, 938–947. [[CrossRef](#)]
143. Ramani, B.M.; Gupta, A.; Kumar, R. Performance of a double pass solar air collector. *Sol. Energy* **2010**, *84*, 1929–1937. [[CrossRef](#)]
144. Sopian, K.; Supranto; Othman, M.Y.; Daud, W.R.; Yatim, B. Double-Pass Solar Collectors with Porous Media Suitable for Higher-Temperature Solar-Assisted Drying Systems. *J. Energy Eng.* **2007**, *133*, 13–18. [[CrossRef](#)]
145. Roy, A.; Hoque, M.E. Performance analysis of double pass solar air heater with packed bed porous media in Rajshahi. *Proc. AIP Conf. Proc.* **2017**, *1851*, 020010.
146. Verma, P.; Varshney, L. Parametric investigation on thermo-hydraulic performance of wire screen matrix packed solar air heater. *Sustain. Energy Technol. Assess.* **2015**, *10*, 40–52. [[CrossRef](#)]
147. Hans, V.S.; Saini, R.P.; Saini, J.S. Heat transfer and friction factor correlations for a solar air heater duct roughened artificially with multiple v-ribs. *Sol. Energy* **2010**, *84*, 898–911. [[CrossRef](#)]
148. Joule, J.P., VIII. On the surface-condensation of steam. *Phil. Trans. R. Soc.* **1861**, *151*, 133–160. [[CrossRef](#)]
149. Alam, T.; Kim, M.-H. A critical review on artificial roughness provided in rectangular solar air heater duct. *Renew. Sustain. Energy Rev.* **2017**, *69*, 387–400. [[CrossRef](#)]

150. Verma, D.; Fortunati, E.; Jain, S.; Zhang, X. *Biomass, Biopolymer-Based Materials, and Bioenergy: Construction, Biomedical, and Other Industrial Applications*; Elsevier Science: Amsterdam, The Netherlands, 2019; ISBN 9780081024270.
151. Jain, S.; Sharma, M.P. Oxidation, Thermal, and Storage Stability Studies of Jatropha Curcas Biodiesel. *ISRN Renew. Energy* **2012**, *2012*, 861293. [[CrossRef](#)]
152. Kumar, B.; Patil, A.K.; Jain, S.; Kumar, M. Effects of Double V Cuts in Perforated Twisted Tape Insert: An Experimental Study. *Heat Transf. Eng.* **2019**, *41*, 17. [[CrossRef](#)]
153. Ghritlahre, H.K.; Sahu, P.K.; Chand, S. Thermal performance and heat transfer analysis of arc shaped roughened solar air heater—An experimental study. *Sol. Energy* **2020**, *199*, 173–182. [[CrossRef](#)]
154. Jain, S.; Sharma, M.P. Engine performance and emission analysis using oxidatively stabilized Jatropha curcas biodiesel. *Fuel* **2013**, *106*, 152–156. [[CrossRef](#)]
155. Prasad, K.; Mullick, S.C. Heat transfer characteristics of a solar air heater used for drying purposes. *Appl. Energy* **1983**, *13*, 83–93. [[CrossRef](#)]
156. Webb, R.L.; Eckert, E.R.G.; Goldstein, R.J. Heat transfer and friction in tubes with repeated-rib roughness. *Int. J. Heat Mass Transf.* **1971**, *14*, 601–617. [[CrossRef](#)]
157. Kreith, F.; Boehm, R.F.; Raithby, G.D.; Hollands, K.G.T.; Suryanarayana, N.V.; Modest, M.F.; Carey, V.P.; Chen, J.C.; Lior, N.; Shah, R.K.; et al. Heat and mass transfer. In *CRC Handbook of Mechanical Engineering*, 2nd ed.; CRC: Boca Raton, FL, USA, 1999; Volume 4, pp. 341–357. [[CrossRef](#)]
158. Webb, R.L.; Eckert, E.R.G. Application of rough surfaces to heat exchanger. *Int. J. Heat Mass Transf.* **1972**, *15*, 1647–1658. [[CrossRef](#)]
159. Prasad, B.N.; Saini, J.S. Effect of artificial roughness on heat transfer and friction factor in a solar air heater. *Sol. Energy* **1988**, *41*, 555–560. [[CrossRef](#)]
160. Ebrahim Momin, A.-M.; Saini, J.S.; Solanki, S.C. Heat transfer and friction in solar air heater duct with V-shaped rib roughness on absorber plate. *Int. J. Heat Mass Transf.* **2002**, *45*, 3383–3396. [[CrossRef](#)]
161. Maithani, R.; Saini, J.S. Performance evaluation of solar air heater having V-ribs with symmetrical gaps in a rectangular duct of solar air heater. *Int. J. Ambient. Energy* **2017**, *38*, 400–410. [[CrossRef](#)]
162. Kumar, A.; Saini, R.P.P.; Saini, J.S.S. Development of correlations for Nusselt number and friction factor for solar air heater with roughened duct having multi v-shaped with gap rib as arti ficial roughness. *Renew. Energy* **2013**, *58*, 151–163. [[CrossRef](#)]
163. Lanjewar, A.M.; Bhagoria, J.L.; Sarviya, R.M. Performance analysis of W-shaped rib roughened solar air heater. *J. Renew. Sustain. Energy* **2011**, *3*, 043110. [[CrossRef](#)]
164. Singh Patel, S.; Lanjewar, A. Experimental and numerical investigation of solar air heater with novel V-rib geometry. *J. Energy Storage* **2019**, *21*, 750–764. [[CrossRef](#)]
165. Karwa, R.; Bairwa, R.D.; Jain, B.P.; Karwa, N. Experimental study of the effects of rib angle and discretization on heat transfer and friction in an asymmetrically heated rectangular duct. *J. Enhanc. Heat Transf.* **2005**, *12*, 343–355. [[CrossRef](#)]
166. Singh, S. Thermal performance analysis of semicircular and triangular cross-sectioned duct solar air heaters under external recycle. *J. Energy Storage* **2018**, *20*, 316–336. [[CrossRef](#)]
167. Patil, A.K.; Saini, J.S.; Kumar, K. Nusselt number and friction factor correlations for solar air heater duct with broken V-down ribs combined with staggered rib roughness. *J. Renew. Sustain. Energy* **2012**, *4*, 033122. [[CrossRef](#)]
168. Wright, L.M.; Fu, W.L.; Han, J.C. Thermal performance of angled, V-shaped, and W-shaped rib turbulators in rotating rectangular cooling channels (AR=4:1). *J. Turbomach.* **2004**, *126*, 604–614. [[CrossRef](#)]
169. Kumar, A.; Kumar, R.; Maithani, R.; Chauhan, R.; Sethi, M.; Kumari, A.; Kumar, S.; Kumar, S. Correlation development for Nusselt number and friction factor of a multiple type V-pattern dimpled obstacles solar air passage. *Renew. Energy* **2017**, *109*, 461–479. [[CrossRef](#)]
170. Tamna, S.; Skullong, S.; Thianpong, C.; Promvong, P. Heat transfer behaviors in a solar air heater channel with multiple V-baffle vortex generators. *Sol. Energy* **2014**, *110*, 720–735. [[CrossRef](#)]
171. Misra, R.; Singh, J.; Kumar, S.; Faujdar, S.; Agrawal, M. Prediction of behavior of triangular solar air heater duct using V-down rib with multiple gaps and turbulence promoters as artificial roughness: A CFD analysis. *Int. J. Heat Mass Transf.* **2020**, *162*, 120376. [[CrossRef](#)]
172. Kumar, A.; Layek, A. Nusselt number and friction characteristics of a solar air heater that has a winglet type vortex generator in the absorber surface. *Exp. Therm. Fluid Sci.* **2020**, *119*, 110204. [[CrossRef](#)]
173. Kumar, R.; Kumar, A.; Chauhan, R.; Maithani, R. Comparative study of effect of various blockage arrangements on thermal hydraulic performance in a roughened air passage. *Renew. Sustain. Energy Rev.* **2018**, *81*, 447–463. [[CrossRef](#)]
174. Singh, A.; Kumar, M.; Alam, T.; Saini, R.P.; Saini, J.S.; Patel, S.S.; Lanjewar, A.; Ghritlahre, H.K.; Prasad, R.K.; Bisht, V.S.; et al. Effect of circularity of perforation holes in V-shaped blockages on heat transfer and friction characteristics of rectangular solar air heater duct. *Energy Convers. Manag.* **2014**, *86*, 952–963. [[CrossRef](#)]
175. Chamoli, S.; Thakur, N.S.S. Correlations for solar air heater duct with V-shaped perforated baffles as roughness elements on absorber plate. *Int. J. Sustain. Energy* **2013**, *35*, 37–41. [[CrossRef](#)]
176. Skullong, S.; Promthaisong, P.; Promvong, P.; Thianpong, C.; Pimsarn, M. Thermal performance in solar air heater with perforated-winglet-type vortex generator. *Sol. Energy* **2018**, *170*, 1101–1117. [[CrossRef](#)]
177. Jain, S.K.; Misra, R.; Kumar, A.; Agrawal, G.D. Thermal performance investigation of a solar air heater having discrete V-shaped perforated baffles. *Int. J. Ambient. Energy* **2019**, *43*, 243–251. [[CrossRef](#)]

178. Promvonge, P.; Khanoknaiyakarn, C.; Kwankaomeng, S.; Thianpong, C. Thermal behavior in solar air heater channel fitted with combined rib and delta-winglet. *Int. Commun. Heat Mass Transf.* **2011**, *38*, 749–756. [[CrossRef](#)]
179. Skullong, S.; Promvonge, P.; Thianpong, C.; Pimsarn, M. Thermal performance in solar air heater channel with combined wavy-groove and perforated-delta wing vortex generators. *Appl. Therm. Eng.* **2016**, *100*, 611–620. [[CrossRef](#)]
180. Karwa, R.; Maheshwari, B.K.K. Heat transfer and friction in an asymmetrically heated rectangular duct with half and fully perforated baffles at different pitches. *Int. Commun. Heat Mass Transf.* **2009**, *36*, 264–268. [[CrossRef](#)]
181. Verma, S.K.K.; Prasad, B.N.N. Investigation for the optimal thermohydraulic performance of artificially roughened solar air heaters. *Renew. Energy* **2000**, *20*, 19–36. [[CrossRef](#)]
182. Sahu, M.M.; Bhagoria, J.L. Augmentation of heat transfer coefficient by using 90° broken transverse ribs on absorber plate of solar air heater. *Renew. Energy* **2005**, *30*, 2057–2073. [[CrossRef](#)]
183. Gupta, D.; Solanki, S.C.C.; Saini, J.S.S. Thermohydraulic performance of solar air heaters with roughened absorber plates. *Sol. Energy* **1997**, *61*, 33–42. [[CrossRef](#)]
184. Pawar, C.B.; Aharwal, K.R.; Chaube, A. Heat transfer and fluid flow characteristics of rib-groove roughened solar air heater ducts. *Indian J. Sci. Technol.* **2009**, *2*, 50–54. [[CrossRef](#)]
185. Varun; Saini, R.P.; Singal, S.K. Investigation of thermal performance of solar air heater having roughness elements as a combination of inclined and transverse ribs on the absorber plate. *Renew. Energy* **2008**, *33*, 1398–1405. [[CrossRef](#)]
186. Gupta, D.; Solanki, S.C.; Saini, J.S. Heat and fluid flow in rectangular solar air heater ducts having transverse rib roughness on absorber plates. *Sol. Energy* **1993**, *51*, 31–37. [[CrossRef](#)]
187. Rohit, A.K.; Lanjewar, A. Thermo-hydraulic performance evaluation using W-Discrete rib in solar air heater. *Indian J. Sci. Technol.* **2016**, *9*, 90–97. [[CrossRef](#)]
188. Singh, S.; Chander, S.; Saini, J.S.S. Heat transfer and friction factor of discrete V-down rib roughened solar air heater ducts. *J. Renew. Sustain. Energy* **2011**, *3*, 013108. [[CrossRef](#)]
189. Maithani, R.; Saini, J.S.S. Heat transfer and friction factor correlations for a solar air heater duct roughened artificially with V-ribs with symmetrical gaps. *Exp. Therm. Fluid Sci.* **2016**, *70*, 220–227. [[CrossRef](#)]
190. Kwak, J.S.; Shin, S. Effect of hole shape on the heat transfer in a rectangular duct with perforated blockage walls. *J. Mech. Sci. Technol.* **2008**, *22*, 1945–1951. [[CrossRef](#)]
191. Lewis, M.J. Optimising the thermohydraulic performance of rough surfaces. *Int. J. Heat Mass Transf.* **1975**, *18*, 1243–1248. [[CrossRef](#)]
192. Mohanty, C.P.; Behura, A.K.; Singh, M.R.; Prasad, B.N.; Kumar, A.; Dwivedi, G.; Verma, P. Parametric performance optimization of three sides roughened solar air heater. *Energy Sources Part A Recover. Util. Environ. Eff.* **2020**. [[CrossRef](#)]
193. Ravi, R.K.; Saini, R.P. Nusselt number and friction factor correlations for forced convective type counter flow solar air heater having discrete multi V shaped and staggered rib roughness on both sides of the absorber plate. *Appl. Therm. Eng.* **2018**, *129*, 735–746. [[CrossRef](#)]
194. Ravi, R.K.; Saini, R.P. Effect of roughness elements on thermal and thermohydraulic performance of double pass solar air heater duct having discrete multi V-shaped and staggered rib roughness on both sides of the absorber plate. *Exp. Heat Transf.* **2017**, *6152*, 47–67. [[CrossRef](#)]
195. Chhapparwal, G.K.; Srivastava, A.; Dayal, R. Artificial repeated-rib roughness in a solar air heater—A review. *Sol. Energy* **2019**, *194*, 329–359. [[CrossRef](#)]
196. Han, J.C.; Zhang, Y.M. High performance heat transfer ducts with parallel broken and V-shaped broken ribs. *Int. J. Heat Mass Transf.* **1992**, *35*, 513–523. [[CrossRef](#)]
197. Karwa, R.; Sharma, A.; Karwa, N. A comparative study of different roughness geometries proposed for solar air heater ducts. *Int. Rev. Mech. Eng.* **2010**, *4*, 159–166.
198. Ghritlahre, H.K.; Verma, M.; Parihar, J.S.; Mondloe, D.S.; Agrawal, S. A detailed review of various types of solar air heaters performance. *Sol. Energy* **2022**, *237*, 173–195. [[CrossRef](#)]
199. Singh, S.; Chander, S.; Saini, J.S. Thermal and effective efficiency based analysis of discrete V-down rib-roughened solar air heaters. *J. Renew. Sustain. Energy* **2011**, *3*, 023107. [[CrossRef](#)]
200. Vogiatzis, I.I.; Denizopoulou, A.C.; Ntinias, G.K.; Fragos, V.P. Simulation analysis of air flow and turbulence statistics in a rib grit roughened duct. *Sci. World J.* **2014**, *2014*, 791513. [[CrossRef](#)]
201. Tariq, A.; Panigrahi, P.K.; Muralidhar, K. Flow and heat transfer in the wake of a surface-mounted rib with a slit. *Exp. Fluids* **2004**, *37*, 701–719. [[CrossRef](#)]
202. Aharwal, K.R.; Gandhi, B.K.; Saini, J.S. Experimental investigation on heat-transfer enhancement due to a gap in an inclined continuous rib arrangement in a rectangular duct of solar air heater. *Renew. Energy* **2008**, *33*, 585–596. [[CrossRef](#)]
203. Singh, S.N. Flow and heat transfer studies in a double—Pass counter flow Solar Air Heater. *Int. J. Heat Technol.* **2013**, *31*, 37–42. [[CrossRef](#)]
204. Karwa, R. Experimental studies of augmented heat transfer and friction in asymmetrically heated rectangular ducts with ribs on the heated wall in transverse, inclined, v-continuous and v-discrete pattern. *Int. Commun. Heat Mass Transf.* **2003**, *30*, 241–250. [[CrossRef](#)]
205. Gawande, V.B.; Dhoble, A.S.; Zodpe, D.B. Effect of roughness geometries on heat transfer enhancement in solar thermal systems—A review. *Renew. Sustain. Energy Rev.* **2014**, *32*, 347–378. [[CrossRef](#)]

206. Karmare, S.V.; Tikekar, A.N. Experimental investigation of optimum thermohydraulic performance of solar air heaters with metal rib grits roughness. *Sol. Energy* **2009**, *83*, 6–13. [[CrossRef](#)]
207. Kumar, A.; Saini, R.P.; Saini, J.S. Effect of roughness width ratio in discrete Multi v-shaped rib roughness on thermo-hydraulic performance of solar air heater. *Heat Mass Transf. Stoffuebertragung* **2014**, *51*, 209–220. [[CrossRef](#)]
208. Cortés, A.; Piacentini, R. Improvement of the Efficiency of a Bare Solar Collector by Means of Turbulence Promoters. *Appl. Energy* **2000**, *36*, 253–261. [[CrossRef](#)]
209. Gupta, M.K.K.; Kaushik, S.C.C. Performance evaluation of solar air heater for various artificial roughness geometries based on energy, effective and exergy efficiencies. *Renew. Energy* **2009**, *34*, 465–476. [[CrossRef](#)]
210. Bahrehmand, D.; Ameri, M.; Gholampour, M. Energy and exergy analysis of different solar air collector systems with forced convection. *Renew. Energy* **2015**, *83*, 1119–1130. [[CrossRef](#)]
211. Saravanakumar, P.T.; Somasundaram, D.; Matheswaran, M.M. Exergetic investigation and optimization of arc shaped rib roughened solar air heater integrated with fins and baffles. *Appl. Therm. Eng.* **2020**, *175*, 115316. [[CrossRef](#)]
212. Abo-elfadl, S.; Yousef, M.S.; Hassan, H. Energy, exergy, and enviroeconomic assessment of double and single pass solar air heaters having a new design absorber. *Process Saf. Environ. Prot.* **2021**, *149*, 451–464. [[CrossRef](#)]
213. Saravanakumar, P.T.; Somasundaram, D.; Matheswaran, M.M. Thermal and thermo-hydraulic analysis of arc shaped rib roughened solar air heater integrated with fins and baffles. *Sol. Energy* **2019**, *180*, 360–371. [[CrossRef](#)]
214. Maithani, R.; Agarwal, R.; Kumar, A.; Sharma, S. Parametric optimization of impinging air jet on hemispherical protrusion of a solar thermal collector. *Exp. Heat Transf.* **2022**, 1–22. [[CrossRef](#)]
215. Ghritlahre, H.K.; Sahu, P.K. A comprehensive review on energy and exergy analysis of solar air heaters. *Arch. Thermodyn.* **2020**, *41*, 183–222. [[CrossRef](#)]
216. Mittal, M.K.; Varun; Saini, R.P.; Singal, S.K. Effective efficiency of solar air heaters having different types of roughness elements on the absorber plate. *Energy* **2007**, *32*, 739–745. [[CrossRef](#)]
217. Singh, V.P.; Jain, S.; Karn, A.; Kumar, A.; Dwivedi, G. Mathematical Modeling of Efficiency Evaluation of Double Pass Parallel Flow Solar Air Heater. *Sustainability* **2022**, *14*, 10535. [[CrossRef](#)]
218. Hernández, A.L.; Quiñonez, J.E. Analytical models of thermal performance of solar air heaters of double-parallel flow and double-pass counter flow. *Renew. Energy* **2013**, *55*, 380–391. [[CrossRef](#)]